

OCT 18 1962



Technical Note

145

EQUATORIAL SPREAD F

WYNNE CALVERT



**U. S. DEPARTMENT OF COMMERCE
NATIONAL BUREAU OF STANDARDS**

THE NATIONAL BUREAU OF STANDARDS

Functions and Activities

The functions of the National Bureau of Standards are set forth in the Act of Congress, March 3, 1901, as amended by Congress in Public Law 619, 1950. These include the development and maintenance of the national standards of measurement and the provision of means and methods for making measurements consistent with these standards; the determination of physical constants and properties of materials; the development of methods and instruments for testing materials, devices, and structures; advisory services to government agencies on scientific and technical problems; invention and development of devices to serve special needs of the Government; and the development of standard practices, codes, and specifications. The work includes basic and applied research, development, engineering, instrumentation, testing, evaluation, calibration services, and various consultation and information services. Research projects are also performed for other government agencies when the work relates to and supplements the basic program of the Bureau or when the Bureau's unique competence is required. The scope of activities is suggested by the listing of divisions and sections on the inside of the back cover.

Publications

The results of the Bureau's research are published either in the Bureau's own series of publications or in the journals of professional and scientific societies. The Bureau itself publishes three periodicals available from the Government Printing Office: The Journal of Research, published in four separate sections, presents complete scientific and technical papers; the Technical News Bulletin presents summary and preliminary reports on work in progress; and Basic Radio Propagation Predictions provides data for determining the best frequencies to use for radio communications throughout the world. There are also five series of non-periodical publications: Monographs, Applied Mathematics Series, Handbooks, Miscellaneous Publications, and Technical Notes.

A complete listing of the Bureau's publications can be found in National Bureau of Standards Circular 460, Publications of the National Bureau of Standards, 1901 to June 1947 (\$1.25), and the Supplement to National Bureau of Standards Circular 460, July 1947 to June 1957 (\$1.50), and Miscellaneous Publication 240, July 1957 to June 1960 (Includes Titles of Papers Published in Outside Journals 1950 to 1959) (\$2.25); available from the Superintendent of Documents, Government Printing Office, Washington 25, D. C.

NATIONAL BUREAU OF STANDARDS
Technical Note

145

AUGUST 1, 1962

EQUATORIAL SPREAD F

Wynne Calvert
Boulder Laboratories
Boulder, Colorado

NBS Technical Notes are designed to supplement the Bureau's regular publications program. They provide a means for making available scientific data that are of transient or limited interest. Technical Notes may be listed or referred to in the open literature.

ABSTRACT

Most equatorial spread F may be attributed to coherent scattering by thin, magnetic-field-aligned irregularities in the ionization of the F layer. These irregularities occur in patches which move horizontally. The velocity of the motion may be measured by (1) the simulation of spread F observed with a single ionosonde, (2) the timing of the occurrence of spread F at spaced ionosondes, or (3) the measurement of the doppler-shift imposed on scattered radio waves. The velocities are west-to-east throughout the night, with magnitudes of 100-200 m/s at sunspot maximum and 50-130 m/s at sunspot minimum. The instability of the F layer giving rise to the formation of spread-F irregularities could result from (1) upward electromagnetic drift of the ionosphere as a whole, (2) thermal contraction of the neutral atmosphere after sunset, (3) atmospheric gravity waves, or (4) geomagnetic support of the F layer against gravity.

This technical note is based upon a thesis submitted by the author to the faculty of the Graduate School of the University of Colorado as a requirement for the degree of Doctor of Philosophy.

The work described here grew from that of research groups affiliated with NBS who are currently studying equatorial phenomena. The observations involved were performed by them; the interpretations were largely the contribution of this author. Some embryos of the ideas developed here were conceived during numerous discussions with Dr. R. Cohen, Dr. T. E. VanZandt, Dr. K. Davies, Dr. M. L. V. Pitteway, Mr. R. B. Norton, Mr. S. Radicella, Mr. J. T. Brown, and Mr. E. Stiltner. Mr. J. T. Brown collected the velocities of figures 26 and 27.

The author wishes to acknowledge the generous guidance of Dr. R. Cohen and Dr. T. E. VanZandt during this work.

CONTENTS

ABSTRACT

Part I

OBSERVATIONS OF SPREAD <u>F</u>	1
Introduction	1
Occurrence of spread <u>F</u>	3
The relation of spread <u>F</u> to other phenomena	11
Equatorial spread- <u>F</u> irregularities	12

Part II

THE INTERPRETATION OF SPREAD <u>F</u>	19
Previous interpretations of spread <u>F</u>	21
A scattering model for equatorial spread <u>F</u>	22
The simulation of equatorial 'scatter' spread <u>F</u>	31
Equatorial 'waveguide' spread <u>F</u>	37
Appendix A. Transformation relationships for backscatter traces	40
Appendix B. Equatorial sporadic <u>E</u> simulation	44

Part III

SPREAD- <u>F</u> MOTIONS	51
Methods of observation	51
Spread- <u>F</u> simulation	52
Spaced ionosondes I	56
Spaced ionosondes II	58
Doppler-shifted oblique scatter	62
Appendix C. Conditions for phase coherence along thin irregularities near the equator	72

Part IV

THEORIES OF SPREAD- <u>F</u> IRREGULARITIES	77
Current theories	77
Electrostatic coupling to the <u>E</u> region	78
Amplification of drifting irregularities	81
Electrostatic drift	83
Thermal contraction of the neutral atmosphere	85
Gravity waves	87
Gravitational instability	88
Conclusions	89
Appendix D. The motion of a cylindrical irregularity in ionization	91
Appendix E. Geographic locations mentioned in the text	101
REFERENCES	102

ILLUSTRATIONS

1. An idealized ionogram	2
2. Equatorial spread- <u>F</u> configurations	4-7
3. Spread- <u>F</u> configurations at high latitudes	8
4. Spread- <u>F</u> occurrence versus magnetic latitude	9
5. Height of the equatorial <u>F</u> layer	13
6. South American map	14
7. Transequatorial scatter signals	16
8. Direction-of-arrival of spread- <u>F</u> echoes	18
9. Ground scatter configuration	20
10. Equatorial scattering model: below the base	26
11. Equatorial scattering model: between the base and the peak	27
12. Equatorial scattering model: above the peak	28
13. Projection of oblique scatter echoes	30
14. Predicted equatorial 'scatter' spread- <u>F</u> ionograms	32
15. Simulation of Huancayo spread <u>F</u>	34
16. Simulation of Huancayo spread <u>F</u>	35
17. Simulation of Huancayo spread <u>F</u>	36
18. Equatorial 'waveguide' spread- <u>F</u> model	38
19. Scattering ray geometry	43
20. Equatorial sporadic <u>E</u> at Huancayo	45
21. Simulation of equatorial sporadic- <u>E</u> traces	47
22. Envelopes of equatorial slant sporadic <u>E</u>	48
23. Simulation of equatorial sporadic- <u>E</u> intensity	50
24. Simulation of spread- <u>F</u> sequence	53
25. Ground distance of spread- <u>F</u> sequence	54

26.	Spread- <u>F</u> velocities at sunspot maximum	55
27.	Spread- <u>F</u> velocities at sunspot minimum	57
28.	Spread- <u>F</u> velocities deduced by Knecht	59
29.	The correlation of spread <u>F</u> between Huancayo and Natal	61
30.	Spread- <u>F</u> doppler shifts	64-65
31.	Loci of phase coherence: single-hop path	67
32.	Loci of phase coherence: double-hop path	69
33.	Spread- <u>F</u> velocities derived from doppler shifts	71
34.	Doppler-shift geometry: vertical view	73
35.	Doppler-shift geometry: plan view	74
36.	Electrostatic coupling scale sizes	80
37.	Amplification of drifting irregularity	82
38.	Motion of a charged particle in a magnetic field	92
39.	Ionization irregularity in cross section	95

Part I

OBSERVATIONS OF SPREAD F

Introduction. Spread F refers to a condition of the upper atmosphere as it appears to an ionosonde. An ionosonde is simply a sweep-frequency radar which responds to radio waves reflected by the ionosphere. It commonly covers the range 1-25 Mc/s and records delays to about 10^{-2} sec. The instrument produces ionograms-plots of frequency versus delay. The delay of the radio-wave pulses is usually presented in terms of virtual height--the delay multiplied by half the free-space velocity of radio waves.

The free electrons of the ionosphere strongly disperse radio waves. The dispersion, neglecting the effects of particle collisions and the geomagnetic field, may be represented by the refractive index μ :

$$\mu^2 = 1 - (f_N/f)^2, \quad (1)$$

where f is the frequency of the radio wave and f_N is the plasma frequency (proportional to the square-root of the electron density). Since the wave is reflected where $f = f_N$ (where $\mu = 0$), the frequency reflected is a measure of the electron density at the height of reflection. The group velocity, (which determines the delay of the ionosonde pulses) derived from equation (1), decreases with increasing electron density. Thus the pulses are retarded by the ionosphere, and the virtual height will exceed the true height of the point of reflection. Figure 1 illustrates how this retardation affects the ionogram. The frequencies marked f_oE , f_oF_1 , f_oF_2 are the penetration frequencies of the various ionospheric layers.

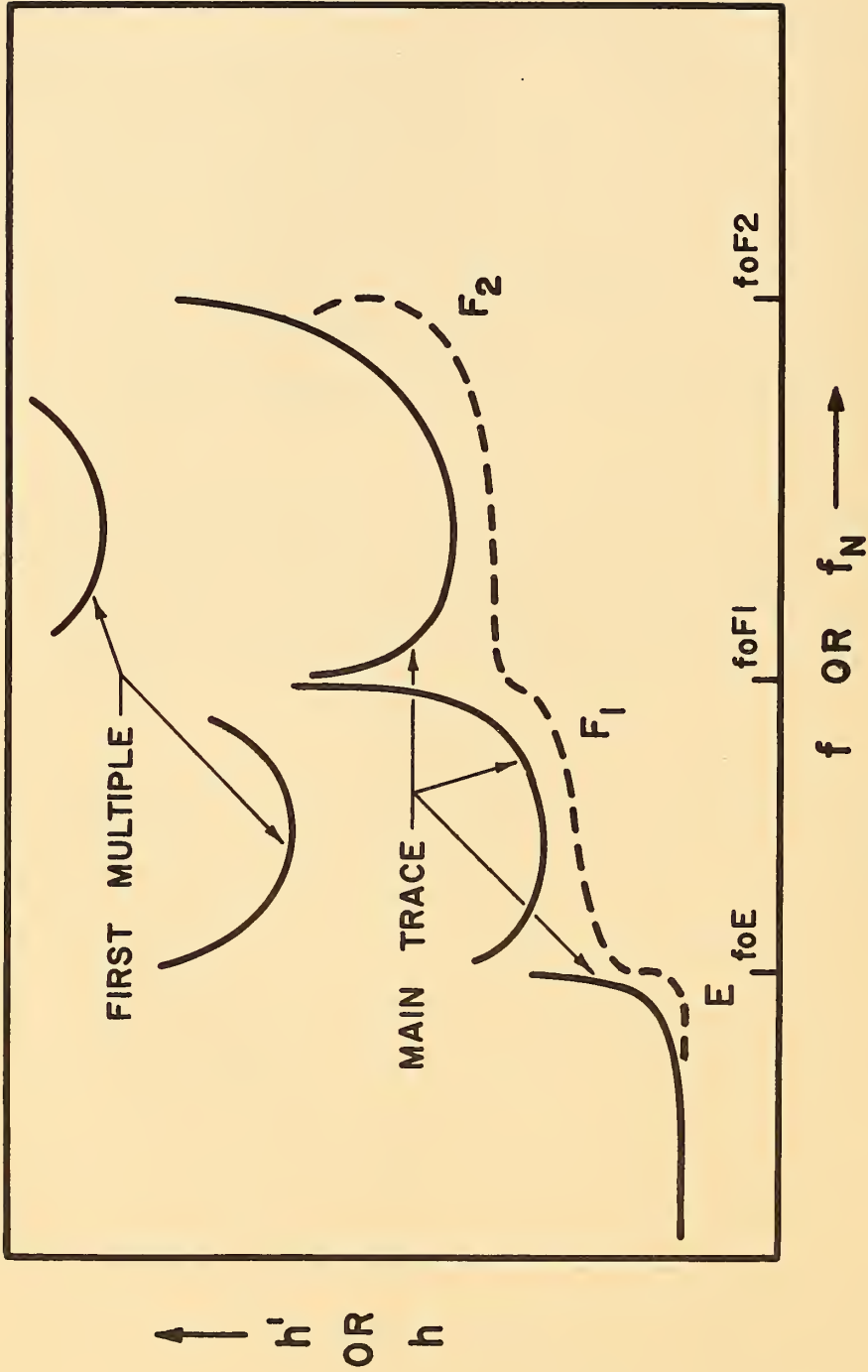


Figure 1. An idealized ionogram (solid) and the corresponding plasma frequency profile (dashed). The former is higher because of retardation within the ionosphere.

The prominent cusps associated with the penetration frequencies result from small electron-density gradients at the height of reflection. Additional traces resembling the main trace often appear on ionograms at greater virtual heights as a result of multiple reflections between the ionosphere and the earth. They are called first-, second-, etc. "multiples".

Spread F is said to occur when the F-layer trace on the ionogram becomes diffuse, in contrast with the sharp trace illustrated in figure 1. The appearance of the diffuse echoes--the configuration of spread F--varies with geographic location and time. Figures 2 and 3 show examples of spread F observed at low and high geomagnetic latitudes, respectively. The former are the topic of this work.

Equatorial spread F appears as variations of the four configurations of figure 2. Based on their interpretation in part II, figures 2a, 2b, 2c show the three basic types of equatorial 'scatter' spread F, and figure 2d shows equatorial 'waveguide' spread F. The significant feature of the configuration which distinguishes between the two is the presence or absence of steep striations like those of figure 2d.

Occurrence of spread F. Spread F occurs in two separate geographic regions in which its characteristics differ considerably. This leads to the division of spread F into equatorial and high-latitude varieties, and to the isolation of the former as the topic of this study.

Figure 4 shows the two regions where spread F is common. This figure is sketched from similar figures by Singleton (1960) to show the essential features of spread-F occurrence as a function of geomagnetic latitude and local time. The equatorial region is bounded by $\pm 20^\circ$ geomagnetic latitude; the high-latitude region(s) by $\pm 60^\circ$ geomagnetic

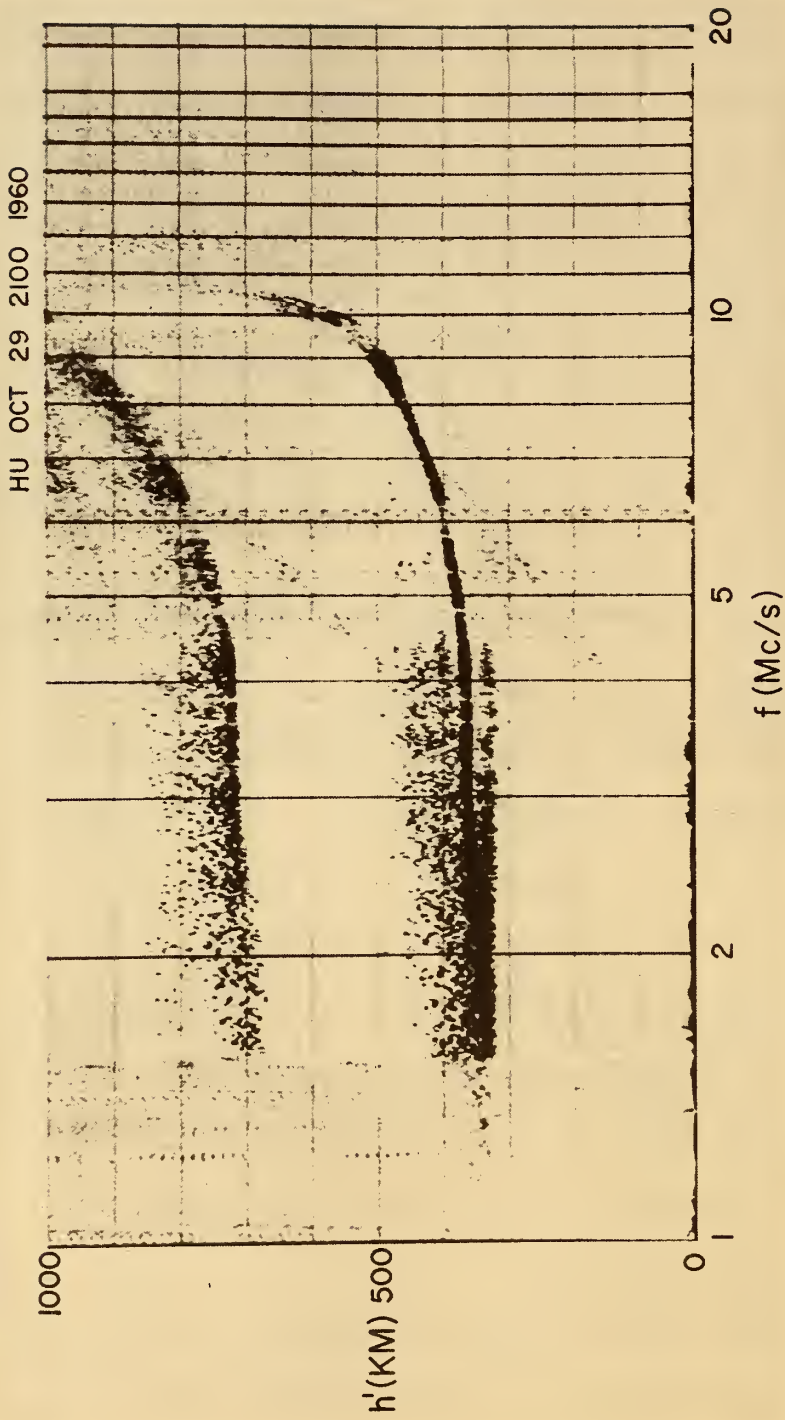


Figure 2a. A "rectangular" equatorial 'scatter' spread-F configuration observed at Huancayo. Recorded at 2100 EST, 29 October 1960.

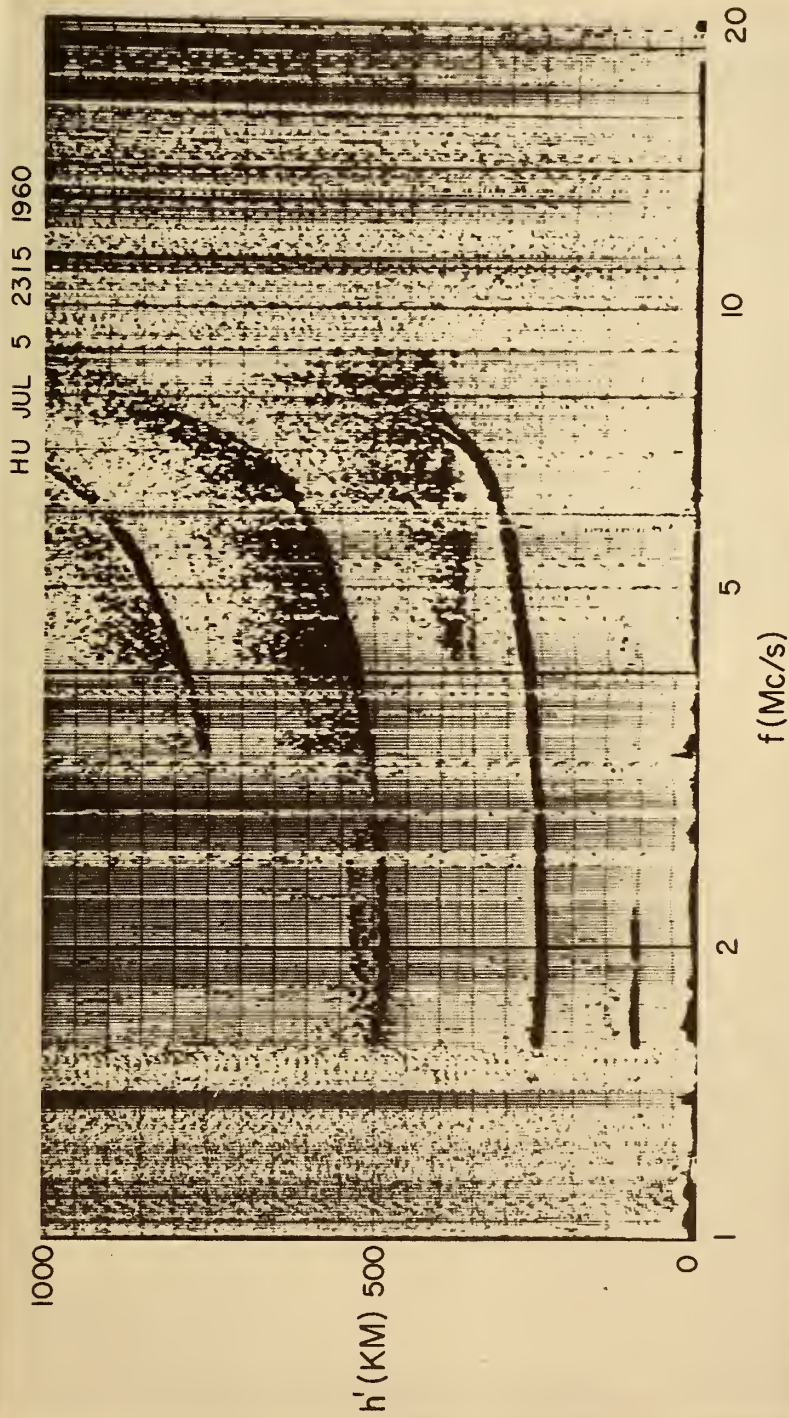


Figure 2b. A "triangular" equatorial 'scatter' spread-F configuration observed at Huancayo. Recorded at 2315 EST, 5 July 1960.

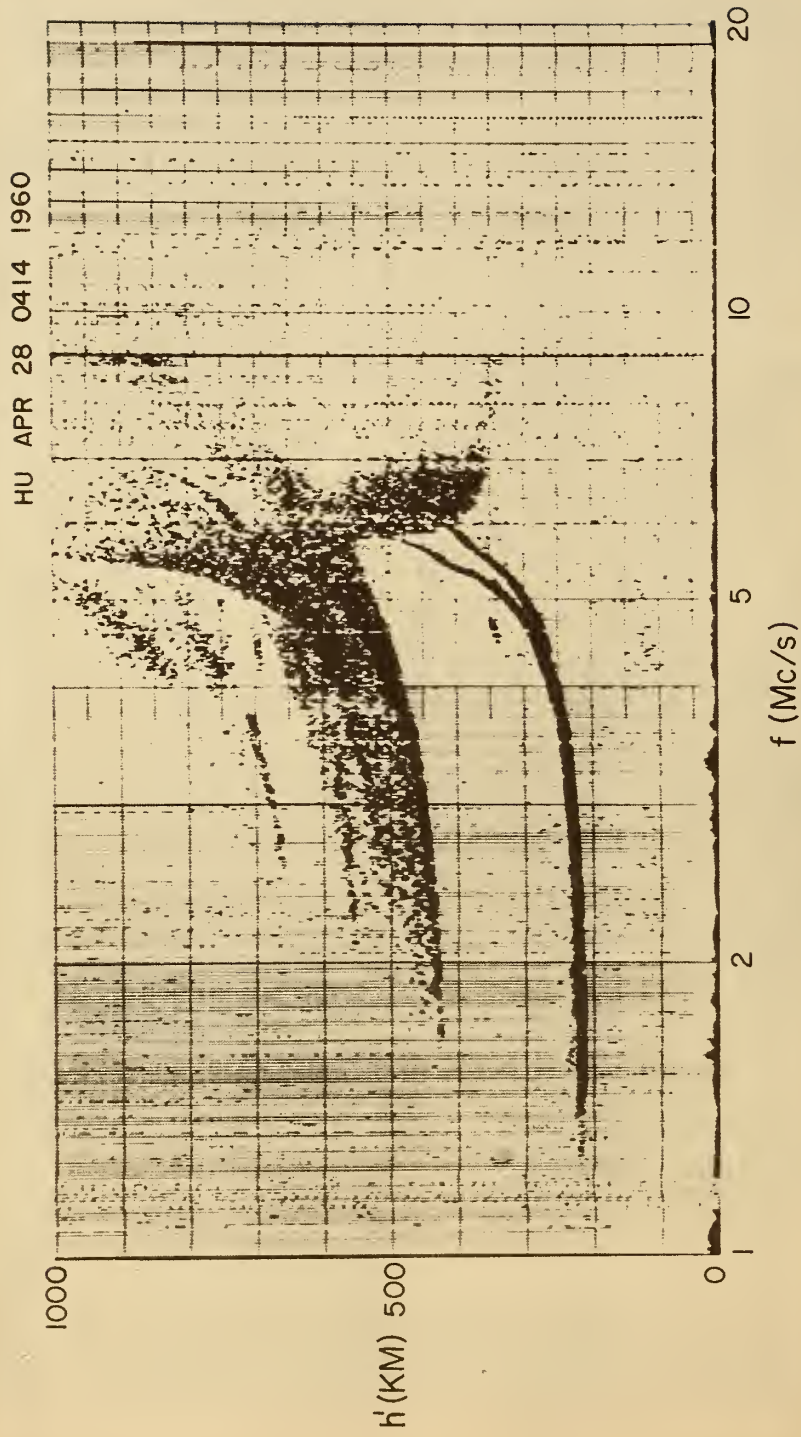


Figure 2c. An equatorial 'scatter' spread-F configuration, aptly called "feathers", observed at Huancayo. Recorded at 0414 EST, 28 April 1960.

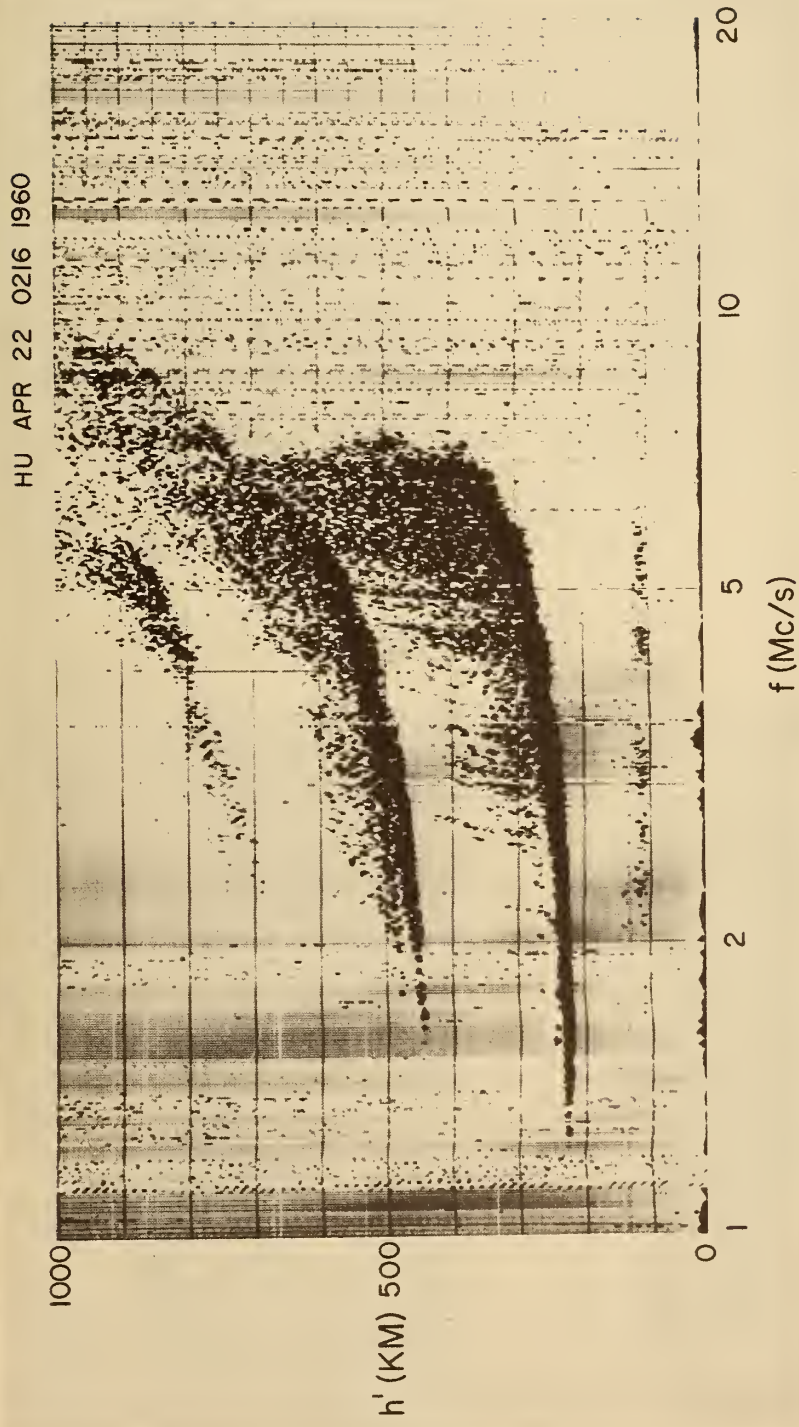


Figure 2d. An equatorial 'waveguide' spread-F configuration observed at Huancayo. Recorded at 0216 EST, 22 April 1960.

POINT BARROW

1340 LT

1 December 1961

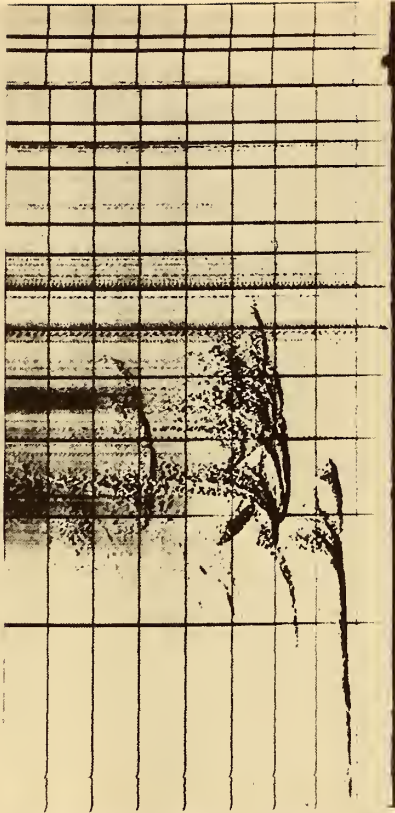


(a)

POINT BARROW

2129 LT

6 December 1961

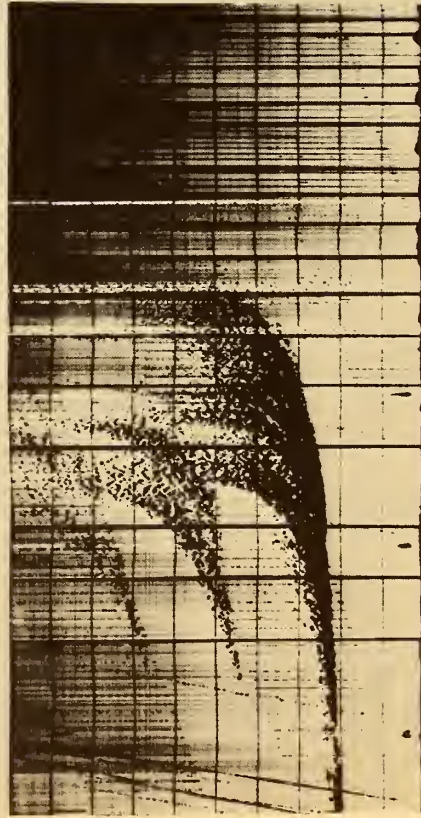


(b)

THULE

1310 LT

17 January 1961

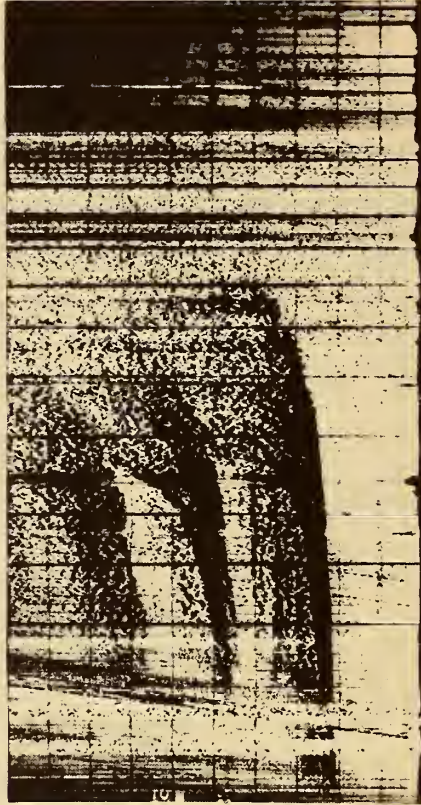


(c)

THULE

1502 LT

17 January 1961



(d)

Figure 3. Some spread-F configurations at high latitudes.

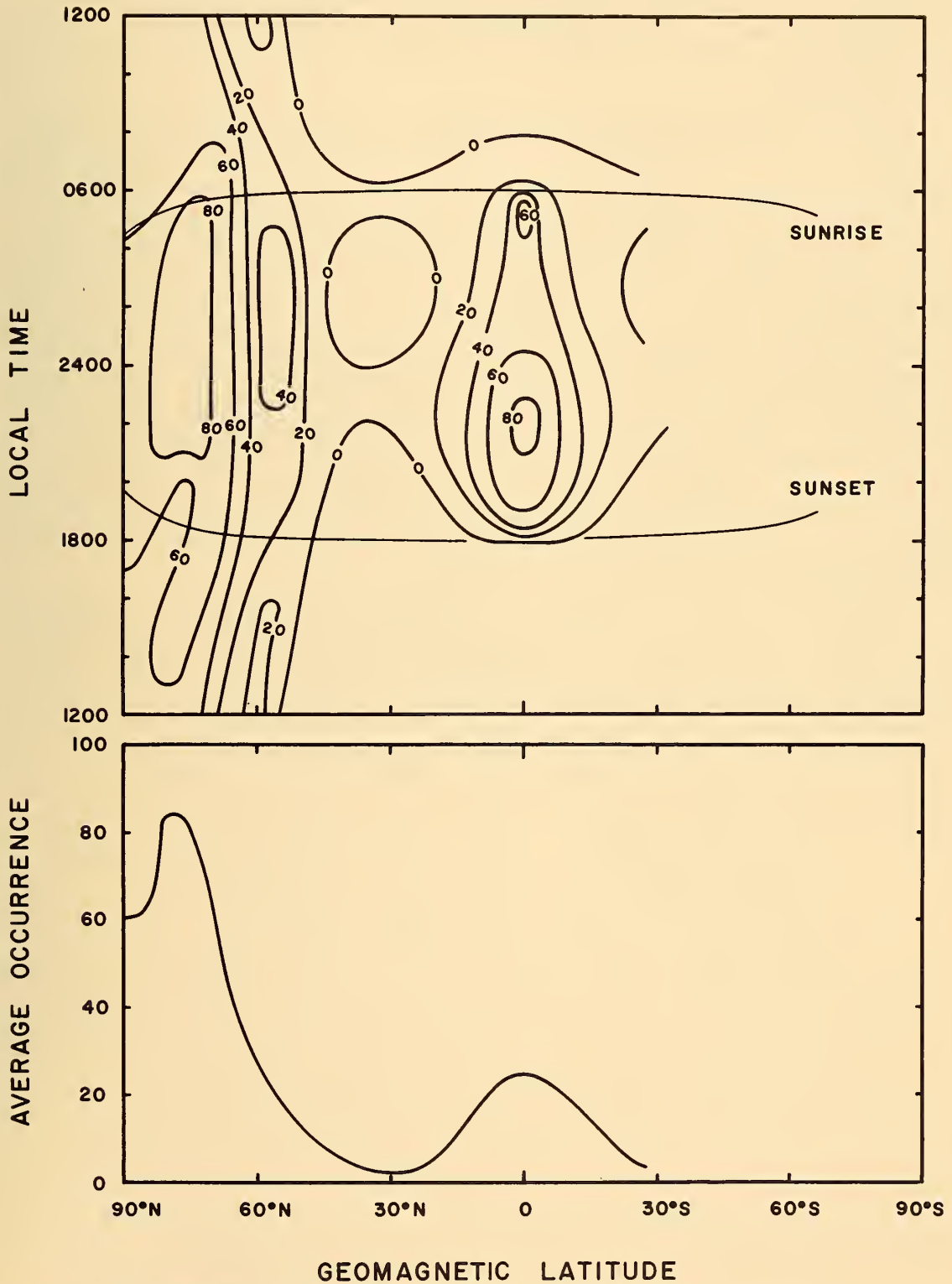


Figure 4. Idealized spread-F occurrence frequency (%) for equinox, sunspot-maximum conditions near the 75th meridian. Adapted from Singleton (1960).

latitude. In the high-latitude region spread F shows a preference for the nighttime, while in the equatorial region it is exclusively a nighttime phenomenon.

The two spread F regions have different seasonal variations. Near the magnetic equator spread F occurs most often during the equinoxes (or during local summer where the magnetic equator departs considerably from the geographic equator). For example, at Huancayo, Peru extensive displays of spread F are observed nightly from November through January, but only on a small handful of nights during June (Cohen and Bowles, 1961). In the high-latitude region the occurrence frequency peaks during local winter although it remains high year-round. This is, of course, confused with the trend toward nighttime occurrence.

The sunspot-cycle dependence of spread F also varies with latitude. Spread-F statistics have been accumulated by Reber (1954a, 1954b, 1956) for stations within the spread-F regions and between the two:

Washington, D.C., USA;	dip: 71°N;	high-latitude
Maui, Hawaii, USA;	dip: 39°N;	intermediate
Rarotonga Island;	dip: 39°S;	intermediate
Dakar, Fr. W. Africa:	dip: 17°N;	equatorial

These data indicate that spread-F occurrence in the equatorial region goes with the sunspot cycle; in the high-latitude region, with the reverse of the sunspot cycle. The effect is much less marked for the former than for the latter. At the intermediate stations the sunspot cycle appears to alter the seasonal dependence. During sunspot minimum the peak occurrence is in local winter; during sunspot maximum, in local summer or equinoxes. These stations seem to exchange their role as equatorial or high-latitude stations with the phase of the sunspot cycle.

The relation of spread F to other phenomena. The occurrence of spread F has been compared with that of a number of other phenomena, including geomagnetic activity, ionospheric scintillation, and F-layer height changes.

The correlation between spread F and magnetic activity is strongly negative near the magnetic equator, positive between 20° and 60° geomagnetic latitude, and again negative near the poles. The negative correlation at very high latitudes is probably a result of observational selection (Shimazaki, 1959b, 1960b), since the polar blackout or auroral absorption occurring with high magnetic indices interferes with F-layer observations. The strong negative correlation for equatorial spread F is in the sense that high magnetic activity by day rarely precedes spread F on the following night (Wright and Skinner, 1959; Rao and Rao, 1961). The effect is strong enough to suggest the prediction of spread F from the state of magnetic activity (Wright, 1959).

Spread F and radio-star scintillation have been correlated in terms of monthly and annual means (Dagg, 1957b), their diurnal variation (Ryle and Hewish, 1950; Koster and Wright, 1960), and individual events (Briggs, 1958; Brenan, 1960; Wild and Roberts, 1956; Wright, Koster, and Skinner, 1956). The correlation is clearly positive for both equatorial and high-latitude stations. Kent (1961) has analyzed the scintillation of radio signals from an artificial satellite. The diurnal occurrence and the relation to magnetic activity agree with those of spread F. The scintillation patterns at the equator correspond to magnetic-field-aligned irregularities 0.4 km by 2 km in size.

Equatorial spread F has been related to height changes of the F layer since the early reports (Booker and Wells, 1938). A theory by Martyn (1959)--discussed in part IV--has recently inspired further study (Wright, 1959; Rao, Rao, and Pant, 1960; Lyon, Skinner, and Wright, 1960b, 1961; Rao and Rao, 1961; Rao and Mitra, 1962). The equatorial F layer appears to rise 50-150 km just after sunset, reaching its greatest height at a time when spread F usually starts (See figure 4.). Figure 5 shows examples of this rise for Huancayo, Peru. The curves are monthly averages of the height of the base of the F layer with and without spread F. From these diagrams it appears that the F layer rises farther and remains high longer with the presence of spread F. The effect is strongest at the equinoxes and weakest during local winter (May-July).

Equatorial spread-F irregularities. Beginning with the IGY, Dr. K. L. Bowles and Dr. R. Cohen of the National Bureau of Standards have conducted a series of observations of magnetic-field-aligned irregularities in the ionosphere above Peru. This section was adapted from their work (Bowles and Cohen, 1957, 1960; Cohen and Bowles, 1961).

As a part of the IGY effort, the following transequatorial scatter experiment was conducted in South America. To study radio-wave scattering in the F layer, a 50 Mc/s transmitter was installed at Antofagasta, Chile to beam a steady "continuous-wave" signal north to Guayaquil, Ecuador. The transmitting and receiving antenna beams intersected at F-region heights above the magnetic equator, as shown in figure 6. In a late phase of the experiment, pulse transmissions over the transequatorial path were employed to determine the height of the scattering irregularities. Finally, a number of additional experiments were conducted at Huancayo, Peru

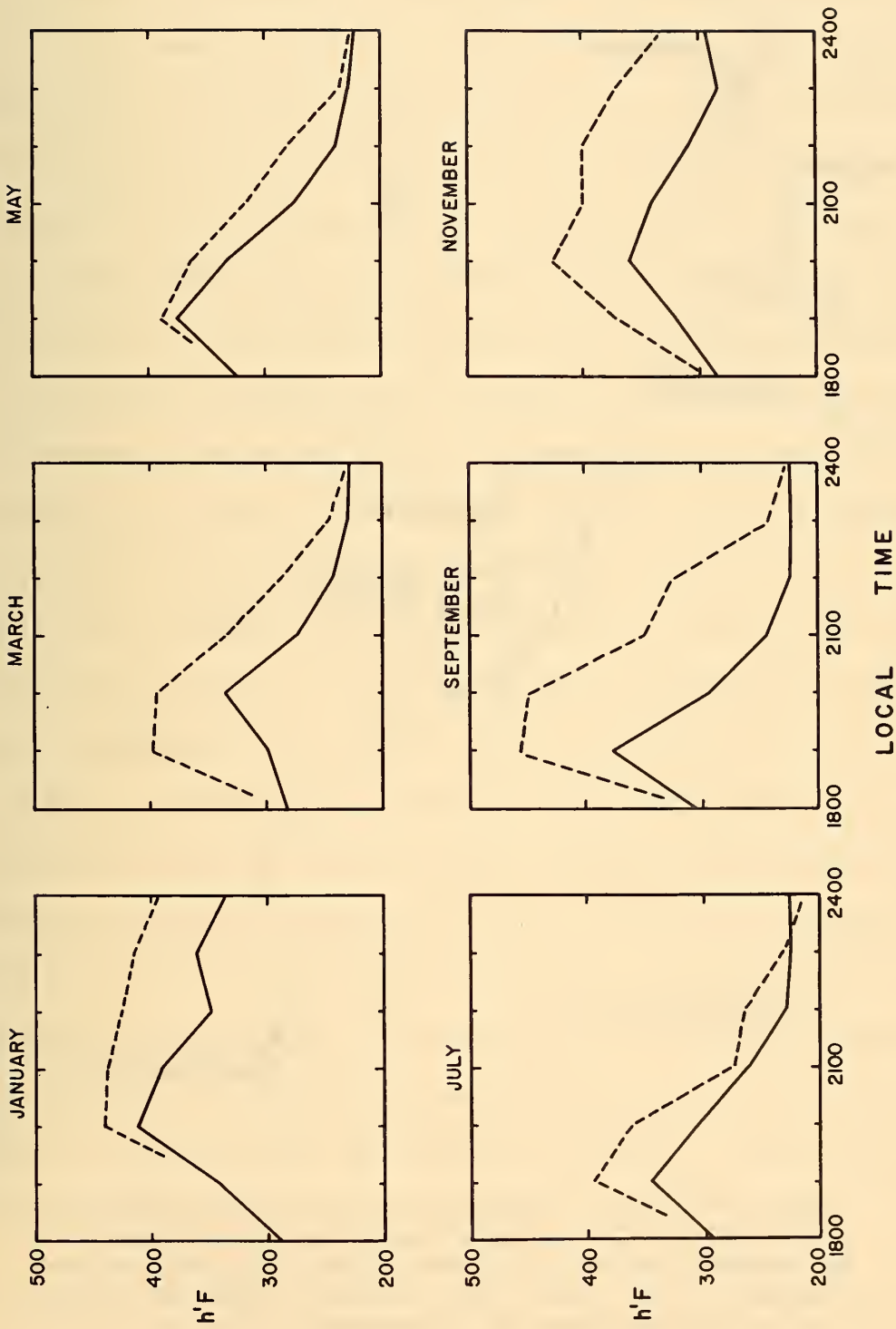


Figure 5. Height (hourly) of the base of the F layer averaged over the month with (dashed) and without (solid) equatorial spread F. Huancayo, Peru data for 1958 were used.

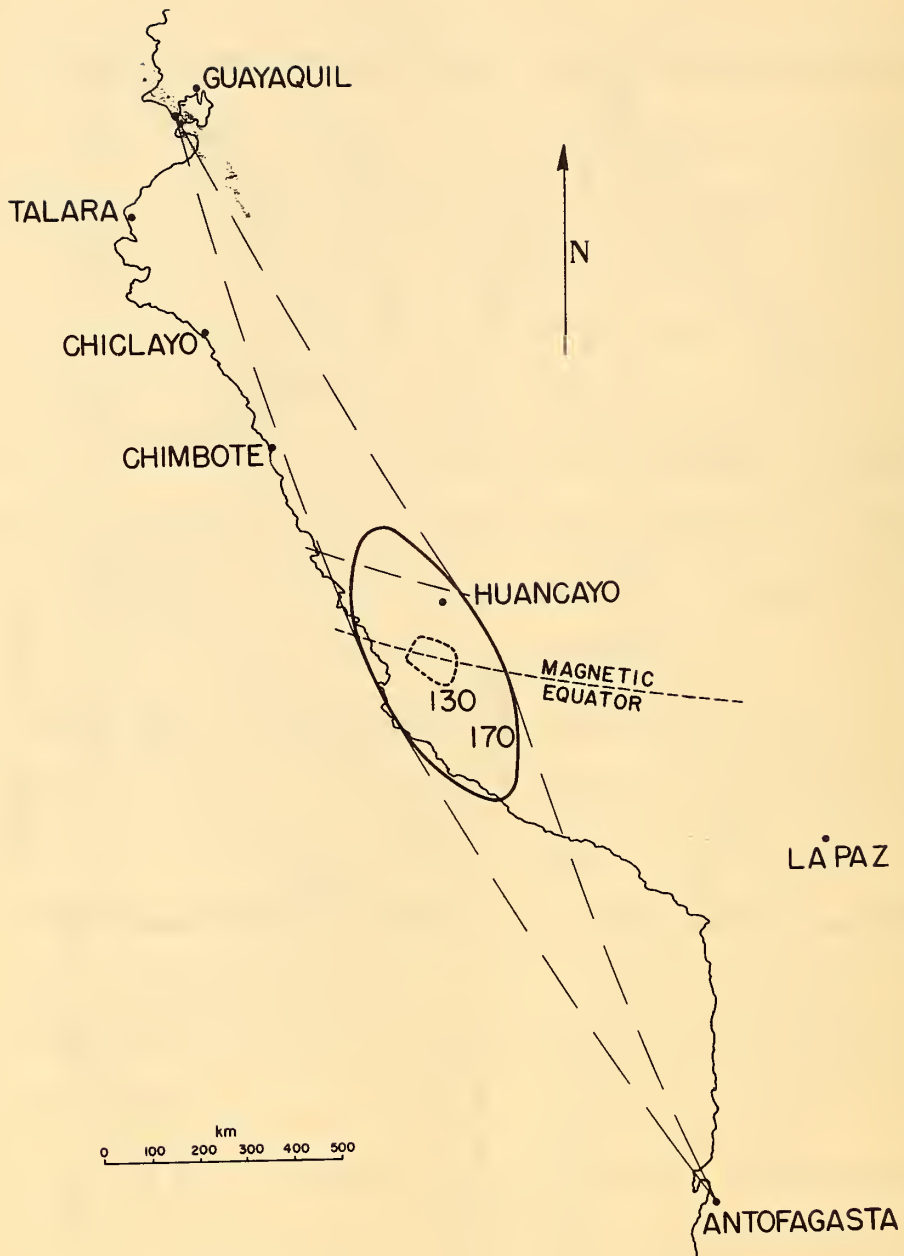


Figure 6. A map of the west coastal area of South America with the approximate loci of antenna beam intersections computed for the heights indicated (130 and 170 km). La Paz, Bolivia; Huancayo, Peru; Talara, Peru; Chiclayo, Peru; and Chimbote, Peru are the locations of ionosondes.

to supplement the data from the forward-scatter experiment.

Figure 7 illustrates the close connection between signal enhancements on the scatter path and the occurrence of equatorial 'scatter' spread F near its midpoint. (Enhancements did not appear to accompany equatorial 'waveguide' spread F.) In these diagrams, time increases from right to left. Figure 7a shows a strong E-layer signal (associated with daytime sporadic E) decaying between 1800 and 1912 and then abruptly giving way to a scatter signal from the F layer. Huancayo ionograms recorded shortly thereafter show the onset of spread F. Concurrent pulse measurements indicated that the scattering took place at the height of the arrows--coincident with the lowest features of the configurations. Much later, the spread-F configuration became more complicated and the signal strength became more variable. Figure 7b shows an early morning enhancement associated with the second type of equatorial 'scatter' spread F (i.e. figure 2b). Both the signal enhancement and the display of spread F at Huancayo develop between 0300 and 0400 and decay between 0400 and 0500. The two peaks in signal strength indicate that two patches of irregularities came into view. In this case the pulse measurements indicated that the scattering took place well within the F layer. The enhancement to the far left is attributed to the onset of sporadic E in the morning. In both of the examples above, the pulse measurements indicated that the patches of spread-F irregularities were the order of only 50 km thick.

The observation of relatively thin patches of spread-F irregularities led to the interpretation that the spread echoes on the ionogram at large delays do not return from overhead, but from some oblique direction.

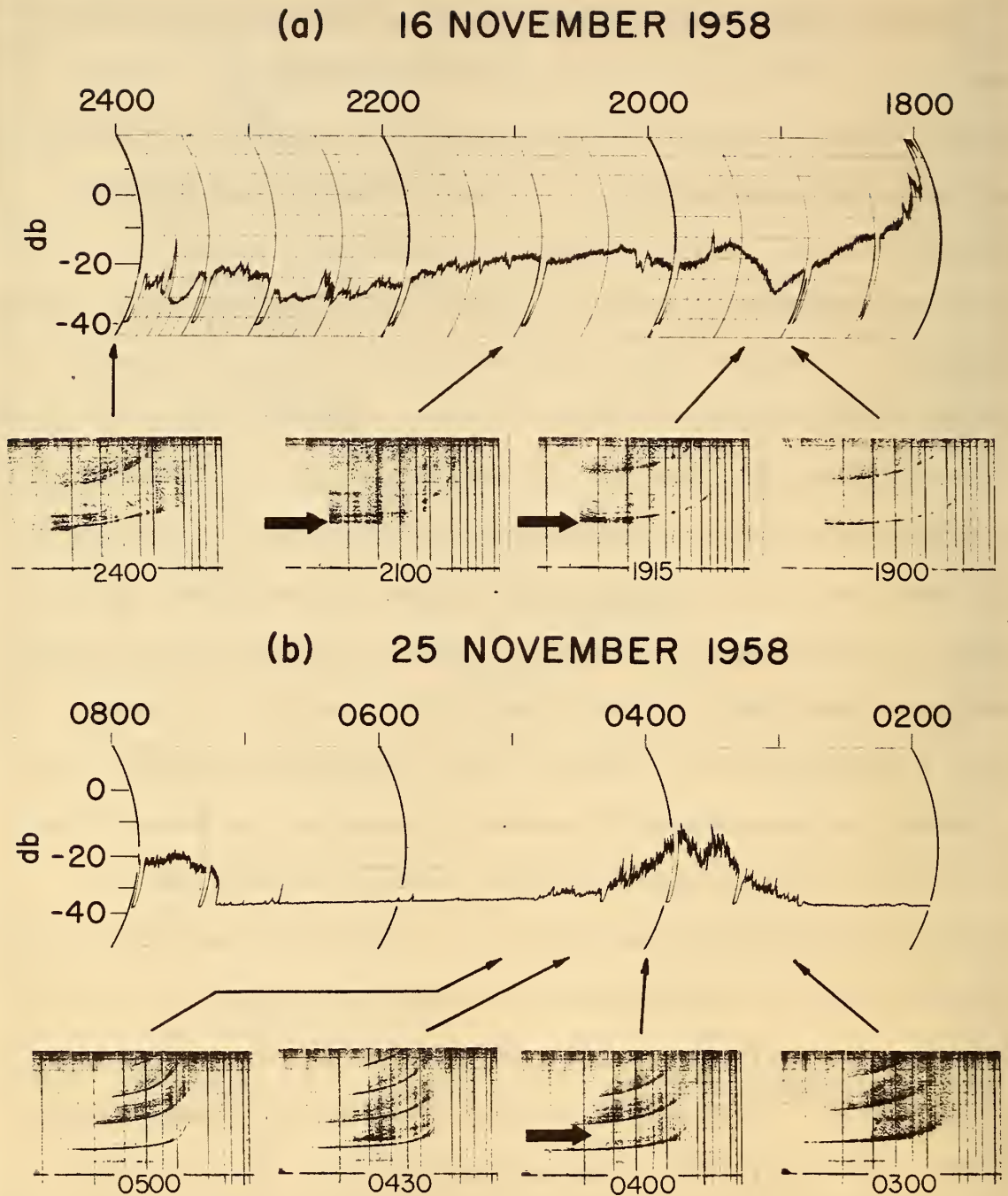


Figure 7. Signal strength for the Antofagasta-Guayaquil scatter path during equatorial 'scatter' spread F_2 at Huancaayo. The height of irregularities derived from pulse measurements is indicated by the arrows. Adapted from Cohen and Bowles (1961).

The direction of this oblique scattering was subsequently determined with directional antennas installed at Huancayo, Peru. Figure 8 shows "A-scan" diagrams--plots of echo strength versus pulse delay--corresponding to 8.3 Mc/s beam antennas inclined 30° to the vertical and directed south, east, west, and north (Pitteway and Cohen, 1961). The transmitted pulse appears at the left edge of each display and time increases toward the right. When the striations of the spread F configuration are largely horizontal (figure 8a) the oblique echoes return from the east and from the west. However, when steep striations like those of figure 2d are also present (figure 8b; above the arrow on the ionogram marking the 8.3 Mc/s operating frequency) oblique echoes also return from the south. This, and the fact that forward scatter at 50 Mc/s is not enhanced with spread F consisting solely of steep striations, is observational evidence for the division of equatorial spread F into the two varieties here termed 'scatter' and 'waveguide'.

The east-west oblique echoes of equatorial 'scatter' spread F are consistent with the picture of coherent scattering by thin, north-south irregularities (the scattering then being strongest in the plane normal to their long dimension). Since 50 Mc/s radio waves are scattered, irregularities the order of 6 m in cross-section (the wavelength at 50 Mc/s) must be present. Further experiments on the north-south coherence of the scattered echoes lead to the conclusions that the irregularities are at least 1 km in length and that they are aligned along the earth's magnetic field.

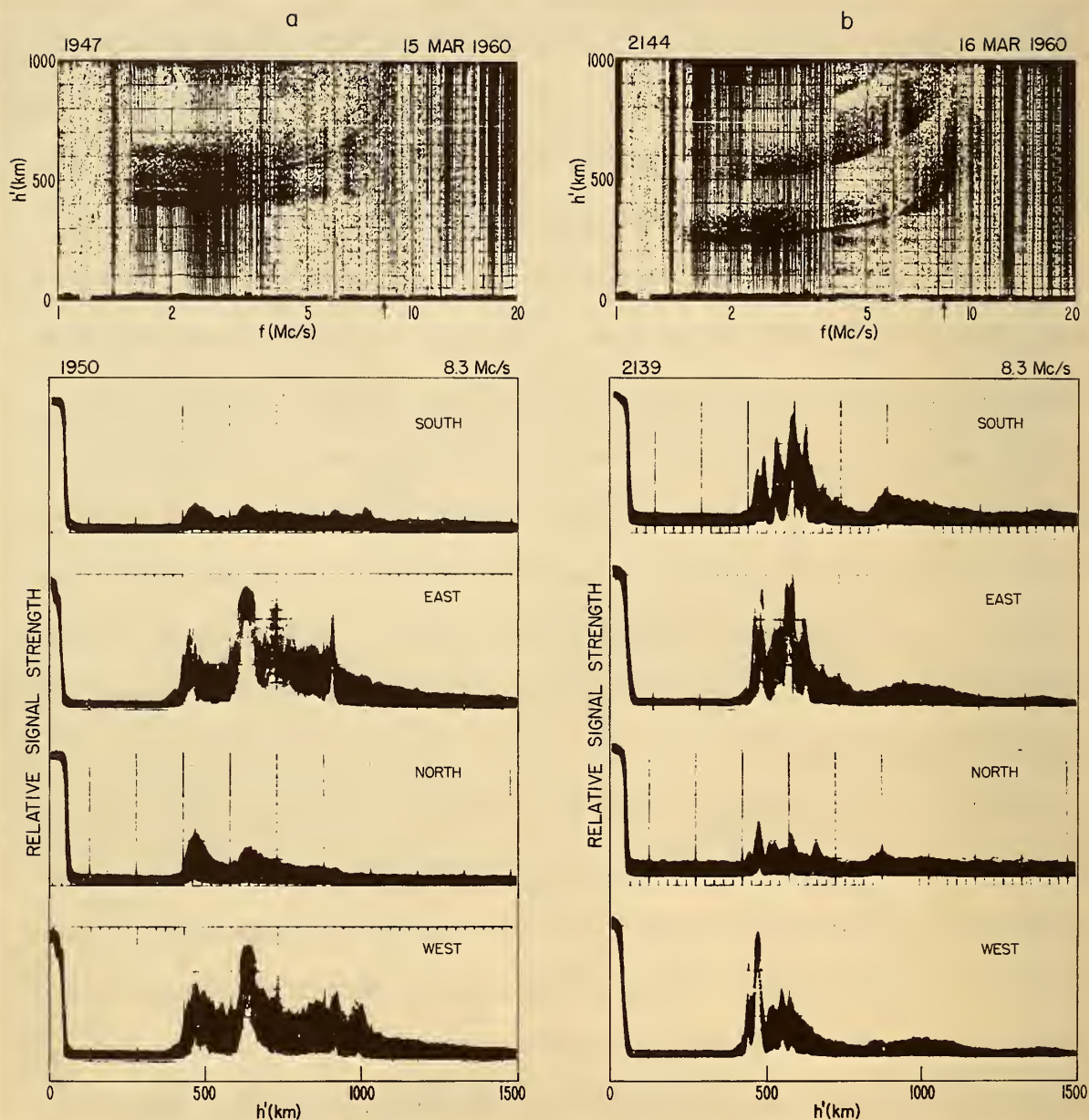


Figure 8. Spread \underline{F} echoes received from various directions during the occurrence of (a) horizontal structure and (b) both horizontal and vertical structure in the spread- \underline{F} configuration at Huancayo. The 8.3 Mc/s operating frequency is indicated by the small arrow on the ionogram.

Part II

THE INTERPRETATION OF SPREAD F

The first phase of a theoretical study of spread F should be the interpretation of the ionogram configuration in terms of a geometrical model. In other words, we wish to know what distribution of electron density, scattering irregularities, etc. will give the observed appearance to the ionogram.

As an example of such a model, Dieminger's (1951) interpretation of ground scatter will be outlined. In figure 9a, the ground scatter echoes are those spread echoes extending upward from the first multiple of the F-layer trace. They seem to be always present when the ionosonde is sufficiently sensitive. Dieminger's interpretation involves radio-wave scattering at the ground: Radio waves are reflected in the F layer; scattered by irregularities on the ground; reflected again in the F layer; and then returned to the ionosonde. Since this propagation circuit becomes the second-hop circuit at vertical incidence, the ground-scatter configuration should naturally extend from the first multiple on the ionogram. Further details of the configuration are revealed by simple ray-path calculations. Neglecting the effects of the earth's magnetic field and assuming horizontal stratification of the ionosphere lead to Martyn's (1935) and Breit and Tuve's (1929) theorems. These compare vertical and oblique ray paths reflected at the same height in the ionosphere. They state that the frequency and delay for such rays are each proportional to the secant of the angle of incidence (i):

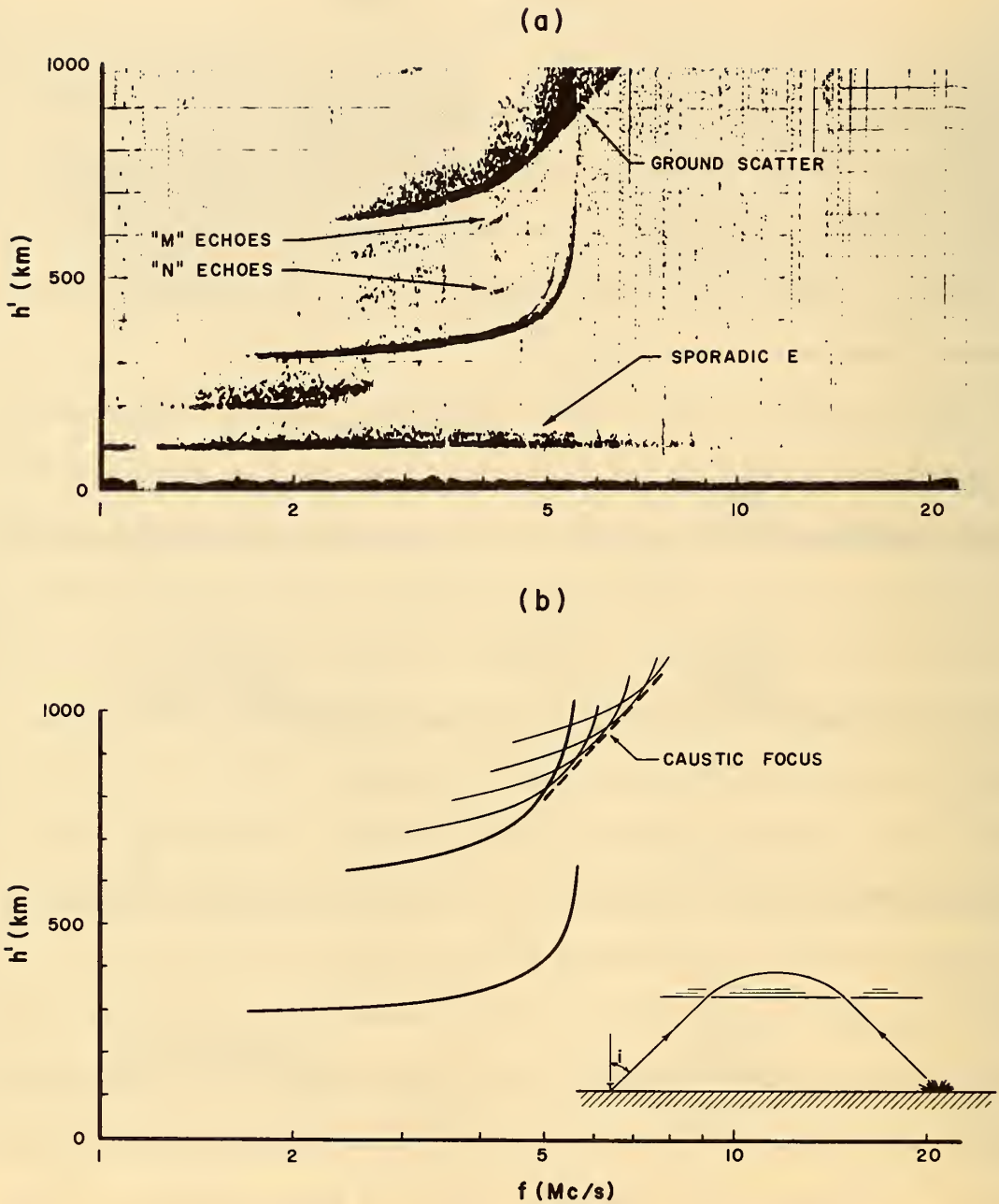


Figure 9. (a) Huancayo, Peru ionogram recorded shortly before dawn, April, 1960, and
 (b) The interpretation of ground scatter proposed by Dieminger (1951): scattering by irregularities on the ground.

$$f_i = f_v \sec i, \quad (\text{Martyn}) \quad (2)$$

$$h'_i = h'_v \sec i, \quad (\text{Breit and Tuve}) \quad (3)$$

where the subscripts v and i refer to vertical and oblique incidence, respectively, f is the frequency, and h' is the delay. Hence the ratio of frequency to delay for oblique rays at a given angle of incidence is a constant times that for vertical incidence. Thus the contribution to ground scatter of a given angle of radiation from the ionosonde antenna is a trace similar to the first multiple with both its delay and frequency increased proportionately, as depicted in figure 9b. The lower edge of the configuration should be linear (i.e. its virtual height proportional to frequency) and is called a caustic focus--the tangential envelope of a set of traces.

Previous interpretations of spread F. Eckersley (1937, 1940) proposed a model for spread F which is essentially that for ground scatter, but with the scattering irregularities in the ionospheric E layer rather than on the ground. The scattering irregularities were considered to be local concentrations of ionization of the proper size and of sufficient contrast with their surroundings to scatter radio-wave energy. Echoes consistent with this model are found to occur (e.g. on the ionogram of figure 9a), and are called "M" and "N" echoes. However, these configurations should not be considered as spread F, but as part of the sporadic E configuration with which

they always occur. This model fails to account for the equatorial spread F configurations of figure 2.

Renau (1959a, 1959b, 1960) has considered a number of spread-F models. Among these are sharp ledges of ionization similar to those proposed by Whale (1951) to explain sporadic E, a scattering screen below the F layer, and aspect-sensitive backscatter by magnetic-field-aligned irregularities in ionization. The models, however, do not appear to provide an adequate explanation of the equatorial spread-F configurations of figure 2.

A scattering model for equatorial spread F. * The equatorial spread-F configurations of figures 2a, 2b, 2c are here considered to arise from coherent scattering by thin, magnetic-field-aligned irregularities. The model is developed in detail for the special case of scattering at the magnetic equator. It attributes most of the features of the spread-F configuration to refraction and retardation imposed on the radio waves by the ionosphere as they travel to and from the position of scattering, and scarcely involves the scattering process itself.

This model is based on the tracing of radio-wave ray paths between the ionosonde and the position of scattering and the computation of the corresponding delays to form theoretical ionograms. It utilizes the simplifying conditions that:

*The content of this and the next section was presented to URSI at the May 1961 meeting by the author and was subsequently published (Calvert and Cohen, 1961).

- (a) the ray-tracing approach is assumed valid (i.e. The electron density is assumed constant over at least a few wavelengths of the radio wave.);
- (b) propagation is confined to the vertical east-west plane through the equatorial ionosonde;
- (c) only the ordinary ray of magnetoionic propagation theory is considered;
- (d) the ionosphere is considered horizontally stratified;
- (e) the scattering irregularities are assumed to scatter somewhat isotropically in the vertical east-west plane; and
- (f) a single-scattering approximation is assumed adequate.

The elongated irregularities are, at the equator, horizontal and oriented north-south. Thus, as indicated above in (b), the plane in which coherent scattering can occur is a vertical east-west plane through the ionosonde. Propagation is thus transverse to the magnetic field and the dispersion relation for the ordinary wave is just that for the field-free case, equation (1). Furthermore, this is also approximately true for the extraordinary wave when, as is often the case with spread \underline{F} , the propagation is sufficiently oblique to the ionosphere. (For this reason, ordinary and extraordinary features can seldom be distinguished in spread- \underline{F}

configurations.) Thus the simplification introduced by condition (c) is justified.

Conditions (a) and (d) allow the use of Snell's law in calculating propagation paths.

Condition (e) implies that an echo may be obtained over any ray path, or combination of ray paths, connecting the ionosonde and the assumed scattering center.

Condition (f) states that the individual irregularities scatter independently, so that the ionogram corresponding to a set of irregularities is simply the superposition of those corresponding to each of the irregularities alone.

The equivalent range corresponding to a pair of ray paths to and from the irregularity is arrived at by integrating the delay along the route. This equivalent range, as a function of frequency, defines a 'scatter trace' on the ionogram. First the scatter traces corresponding to a scattering irregularity overhead are discussed. The results will then be transformed to give the scatter traces corresponding to an irregularity east or west of the ionosonde.

For the overhead case, the (vertical) equivalent range h'_V is first computed from equation (13) with $f = f_A$ (See appendix A). This simple integration yields resulting ionograms like those of figures 10a, 11a, and 12a for irregularities situated at or below the base (h_0) of the F layer, between the base and the peak (h_m) of the F layer, and at or above the peak of the F layer, respectively. For the first two, there are three possible 'round-trip' ray paths:

(i) the direct path to the irregularity and return, (ii) the path reflected to the irregularity by the overlying ionosphere and return, and (iii) the combination of these two--arriving by one path and returning by the other. The 'backscatter' modes (i) and (ii), contribute the two added traces on the ionograms of figures 10a and 11a, above and below the regular \underline{F} -layer trace. The 'combination' mode, (iii), produces a scatter trace with equivalent ranges which are the averages (at each frequency) between those of the backscatter modes. Thus, in this case, the combination trace coincides with the regular \underline{F} -layer trace. With the irregularity above the peak of the layer, no reflected ray path is possible, and only one scatter trace, that of mode (i), is produced on the ionogram (figure 12a).

There is a point-to-point correspondence between the backscatter traces for an irregularity overhead and those for an irregularity at the same height, but located east or west of the ionosonde. It is represented by the transformation:

$$f_R = f_V (1 + R^2/h'_V)^{\frac{1}{2}}, \quad (4)$$

$$h'_R = h'_V (1 + R^2/h'_V)^{\frac{1}{2}}, \quad (5)$$

where $h'_V = h'_V(f_V)$ represents a backscatter trace produced by an irregularity overhead and $h'_R(f_R)$ represents the corresponding backscatter trace produced by an irregularity at the same height, but at a ground distance R from the ionosonde. This transformation, a generalization of that expressed by equations (2) and (3), is derived in appendix A.

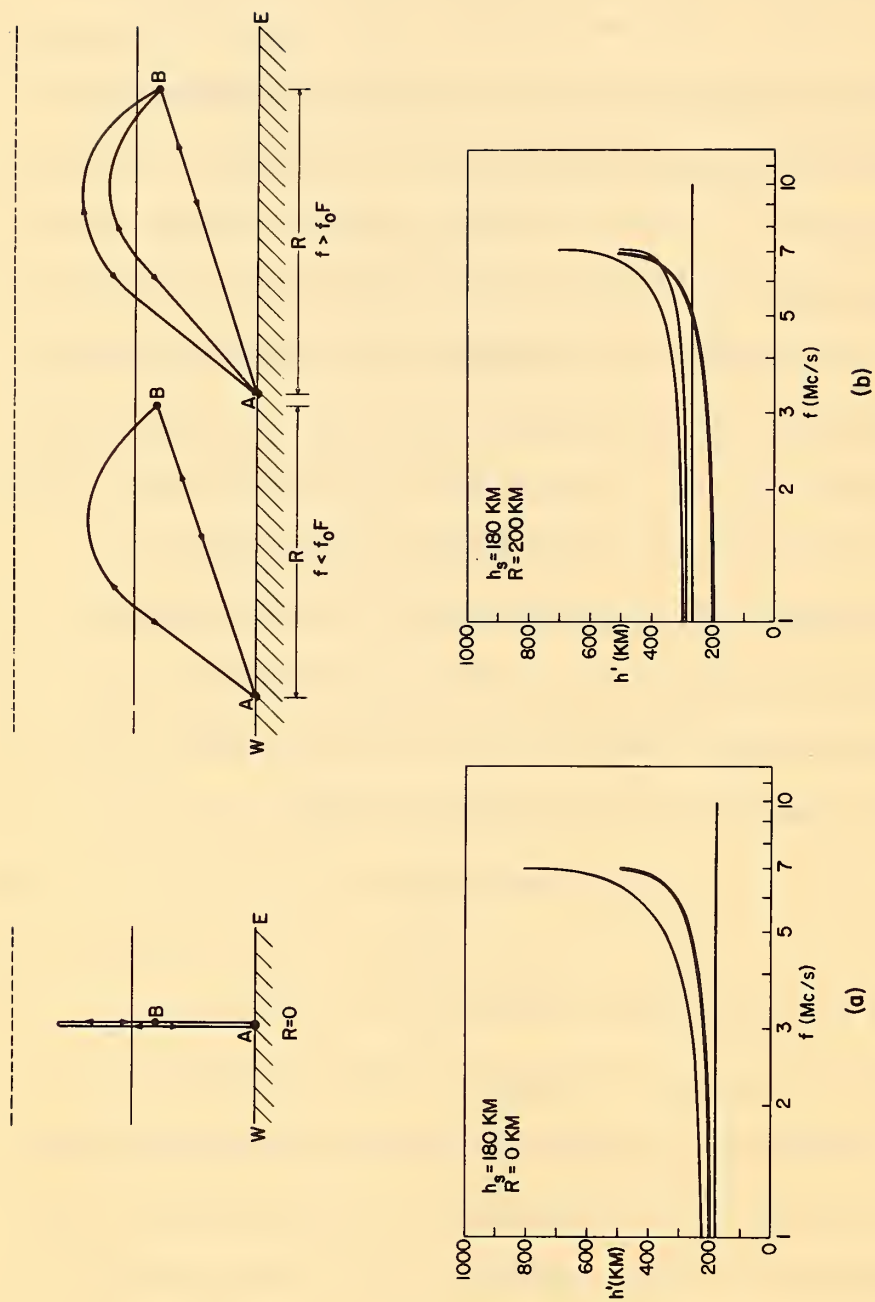


Figure 10. Ray-paths and the resulting 'ionograms' for an irregularity at or below the base of the \underline{F} layer: (a) directly overhead; (b) at a ground distance of 200 km from the ionosonde. (The parabolic \underline{F} layer used in this case and in the calculations of figures 11, 12, and 14 has its base at 200 km, its peak at 300 km, and a penetration frequency of 7.0 Mc/s.)

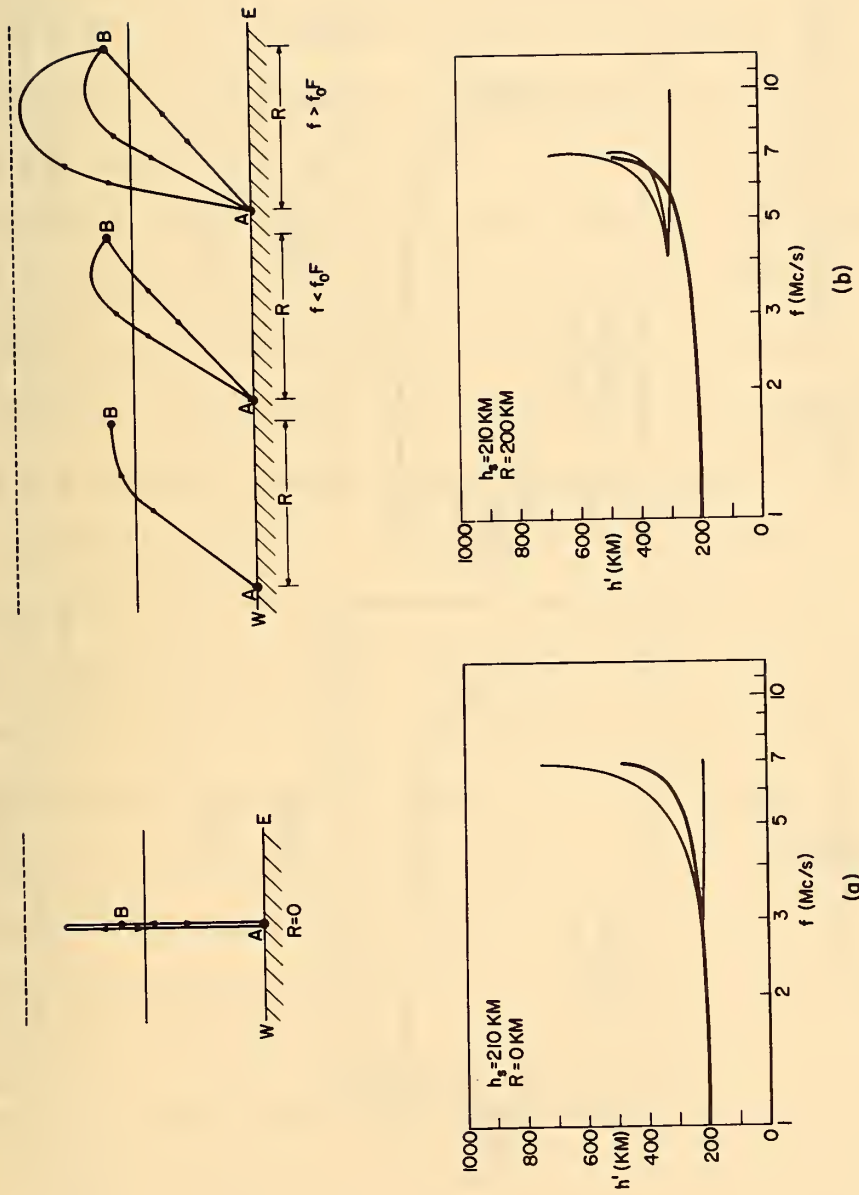


Figure 11. Ray-paths and the resulting 'ionograms' for an irregularity embedded between the base and the peak of the F layer: (a) directly overhead; (b) at a ground distance of 200 km from the ionosonde.

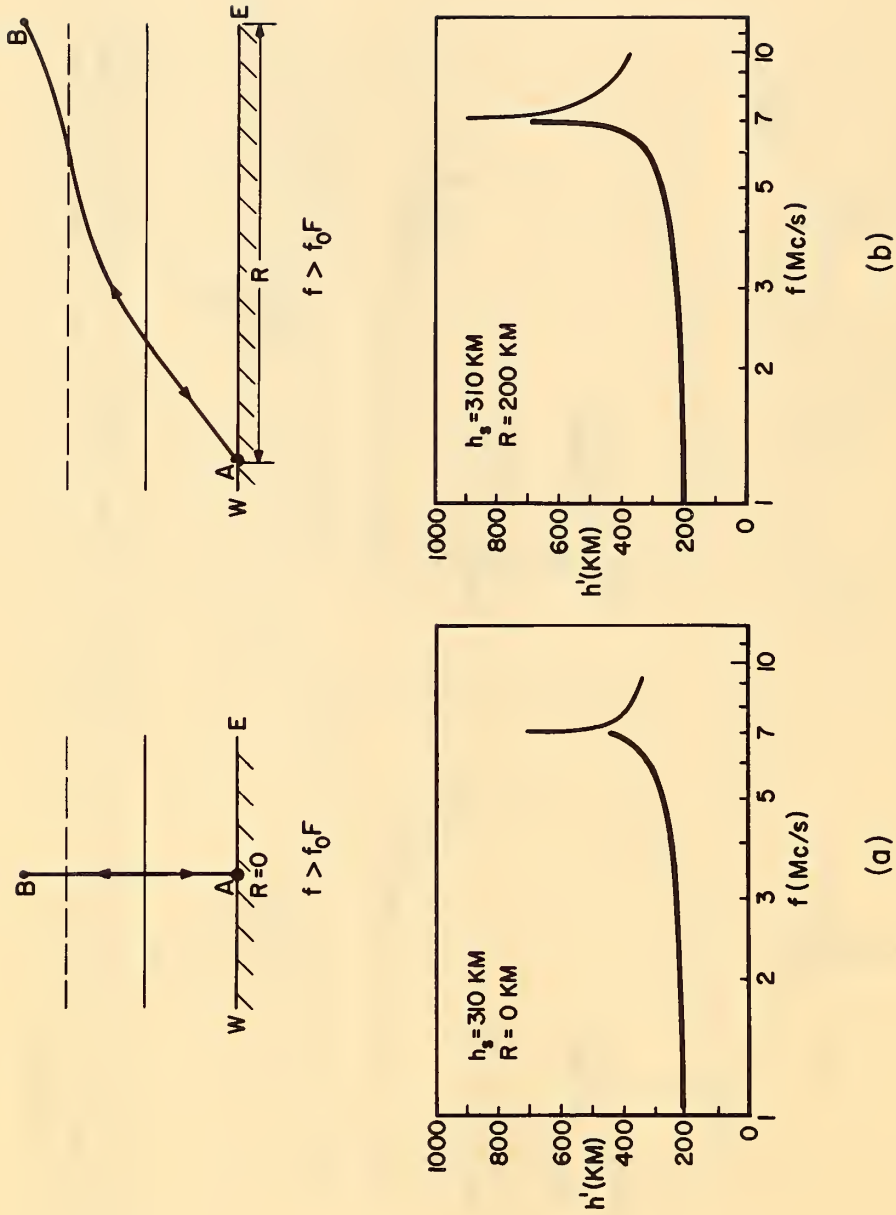


Figure 12. Ray-paths and the resulting 'ionograms' for an irregularity embedded in the F layer at or above its peak electron density: (a) directly overhead; (b) at a ground distance of 200 km from the ionosonde.

As illustrated in figure 13, the transformation has the effect of projecting the backscatter traces toward greater frequencies and toward greater equivalent ranges. On an ionogram with linear axes, the projection is along straight lines which pass through the origin.

Finally, the combination traces for the oblique case are again calculated by averaging the equivalent ranges of the two backscatter traces. The middle scatter traces in figures 10b and 11b were calculated in this manner. On actual ionograms, such combination traces might be expected to dominate over their related backscatter traces, since (1) there are two 'round-trip' ray paths of equal retardation combining to produce them and (2) the scattering is through a smaller--and hence more favorable--scattering angle.

Near the penetration frequency of the layer (f_oF) the mode (ii) backscatter trace for an overhead irregularity is greatly retarded (h'_v approaches infinity as f_v approaches f_oF). It is apparent from the transformation that the corresponding oblique scatter trace must double back to approach an asymptote at this penetration frequency (as h'_v approaches infinity, f_R approaches f_v and thus f_oF). The upper branch of such traces (e.g. figures 10b, 11b, and 13) is a manifestation of the "Pederson" or "high-angle" mode of propagation engineering, the 'nose' frequency playing the role of a 'maximum usable frequency' (MUF) between the ionosonde and the irregularity.

For an irregularity embedded between the base and the peak of the layer, scatter traces begin abruptly at a 'vertex' or 'triple-point' where three scatter traces emerge (e.g. figure 11b). When

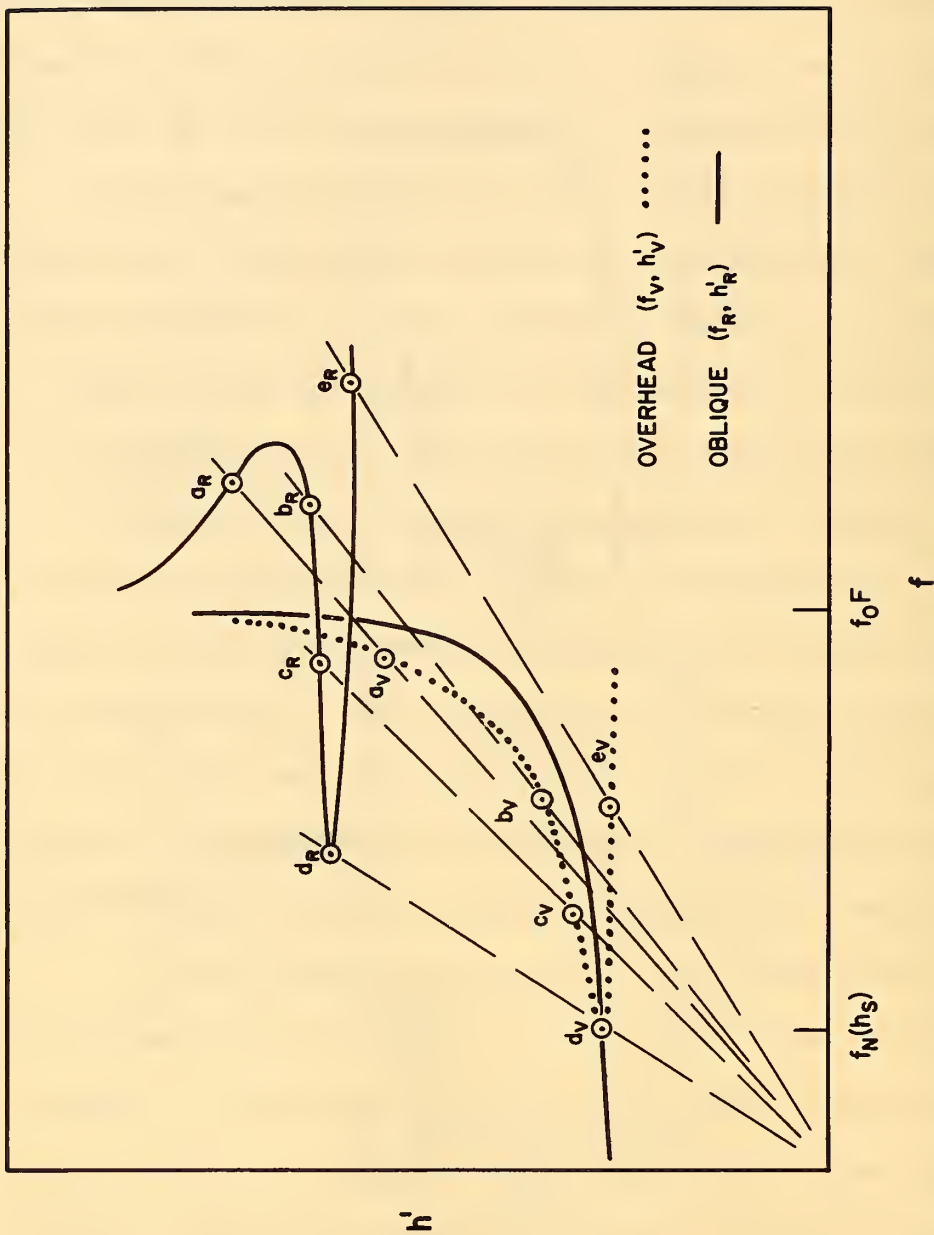


Figure 13. Schematic transformation of the backscatter traces for an irregularity embedded between h_0 and h_m (the case of figure 11).

the irregularity is overhead, this occurs at the local plasma frequency around the irregularity; when oblique, at a higher frequency. The triple-point may even occur beyond the penetration frequency of the F layer (e.g. figure 14; $h_s = 220$ km, $R = 400$ km).

Figure 14 is a collection of predicted ionograms for individual scattering irregularities at various heights and various ground distances from the ionosonde. Among these the basic features of the three configurations of equatorial 'scatter' spread F may be found. The distinction among the three is thus interpreted in terms of the height of the irregularities with respect to the F layer: below the base, figure 2a; between the base and the peak, figure 2b; and above the peak, figure 2c.

In addition, the propagation model described in this section also applies to interpretation equatorial sporadic E (See appendix B.).

The simulation of equatorial 'scatter' spread F. Certain observed configurations of equatorial spread F will now be interpreted on the basis of the above model. The technique employed is that of synthesis, wherein an electron-density profile and the positions of assumed scattering irregularities are determined so as to obtain agreement with the observed ionogram.

The electron-density profile is derived from the regular F trace on the ionogram. For the nighttime, Huancayo ionograms involved, a simple parabolic distribution was usually an adequate approximation.

The synthesis enables the measurement of various parameters of the patches of spread-F irregularities, such as their dimensions, their positions, and the velocities of their motions.

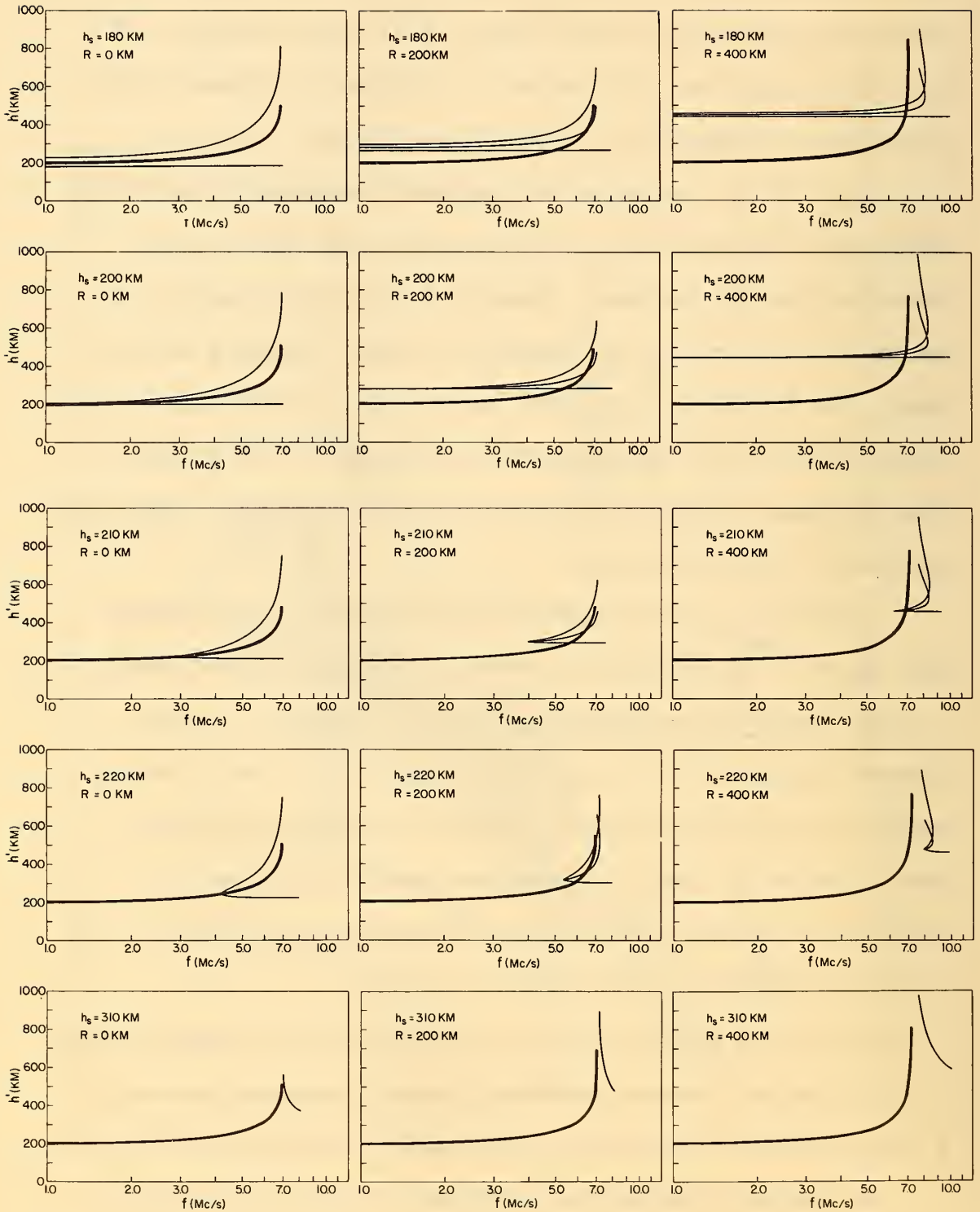


Figure 14. Predicted 'ionograms' for irregularities at various heights, h_s , and ground distances, R , east or west of an equatorial ionosonde.

Occasionally, more than one spread-F configuration may appear concurrently, as in figure 15a. Here the rectangular spread-F configuration (attributed to low-lying irregularities) occurs at low frequencies, while the triangular spread F configuration (attributed to embedded irregularities) occurs at higher frequencies. The synthesis of this pair of configurations is presented in figure 15b. The rectangular portion is calculated for a patch of irregularities located just at the base of the layer (at 328 km height), extending from overhead out to a ground distance of 300 km. The triangular portion was obtained with a single irregularity embedded in the F layer at a height of 334 km and at a ground distance of 500 km. (The high-frequency cutoff of each scatter trace has been introduced arbitrarily.) The fact that no echoes are observed corresponding to irregularities between the two patches leads to the interpretation that they are separate.

The ionogram in figure 16a is an example of the third configuration of equatorial 'scatter' spread F. (The descriptive term "feathers" characterizes its form.) The synthesis (figure 16b) of this configuration is based upon a patch of irregularities within a ground distance of 100 km from the ionosonde, and extending in height between 310 km and 350 km--5 km to 45 km above the peak of the F layer. The thickness of this patch of irregularities (around 40 km) appears to be representative of spread-F patches.

Figure 17a is another example of equatorial 'scatter' spread F interpreted in terms of embedded irregularities. Its partial synthesis (figure 17b) is based on four irregularities at a height

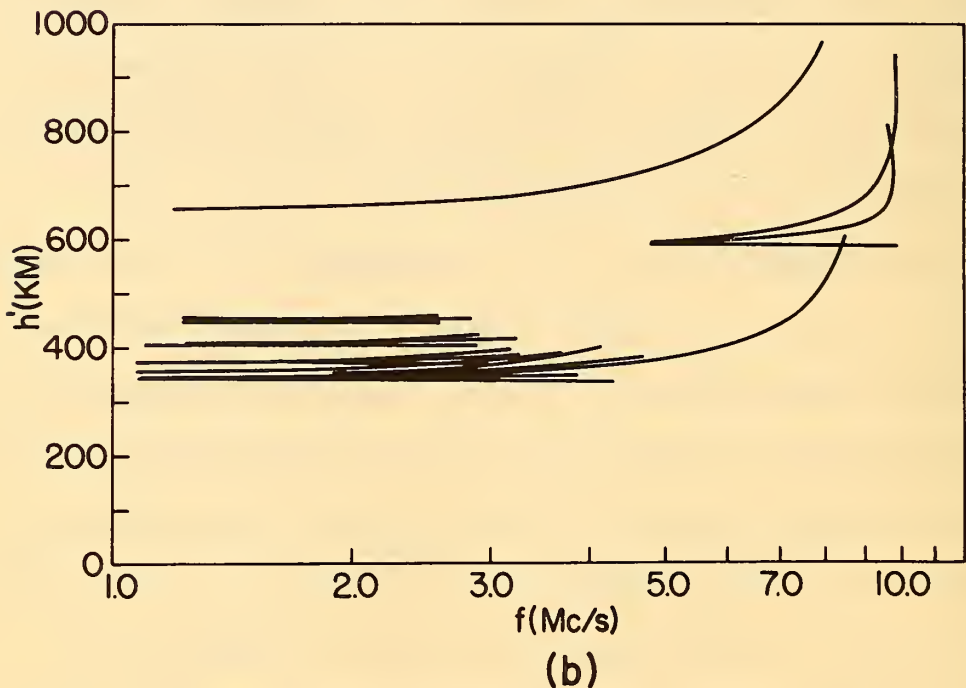
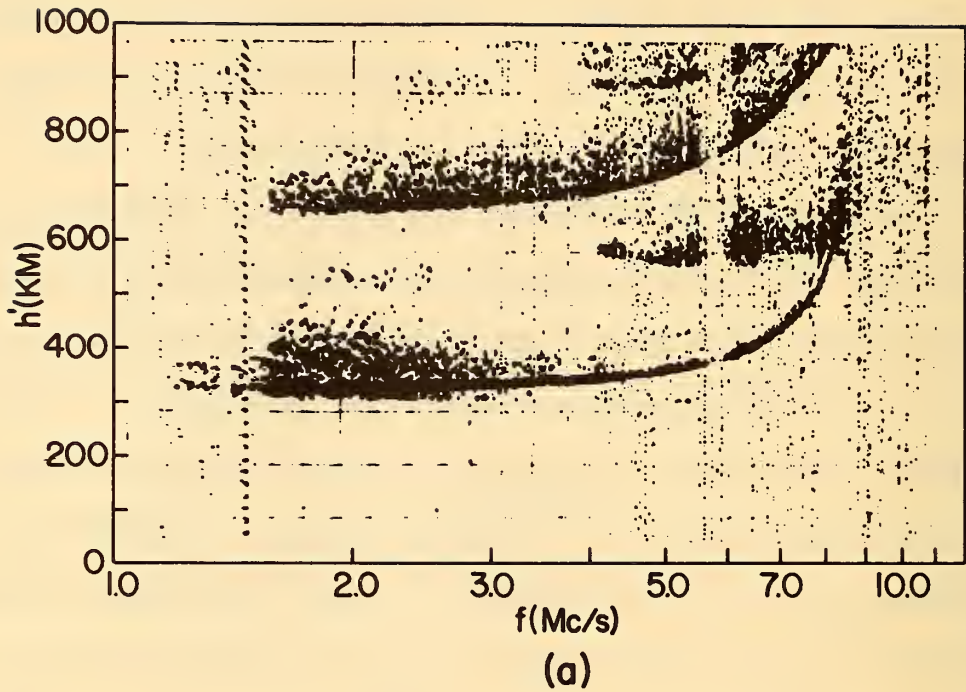


Figure 15. (a) Huancayo ionogram, recorded at 2031 EST, 21 April 1960, in which two spread- \underline{F} configurations appear, and (b) The simulation of this ionogram. (The parabolic \underline{F} layer used for this calculation has $h_o = 328$ km, $h_m = 450$ km, and $f_{o\underline{F}} = 8.4$ Mc/s.)

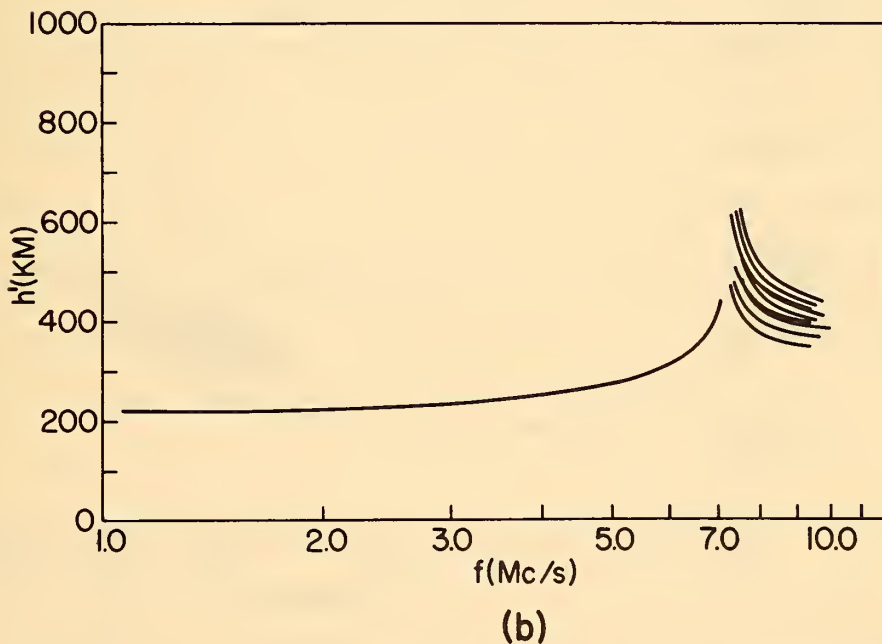
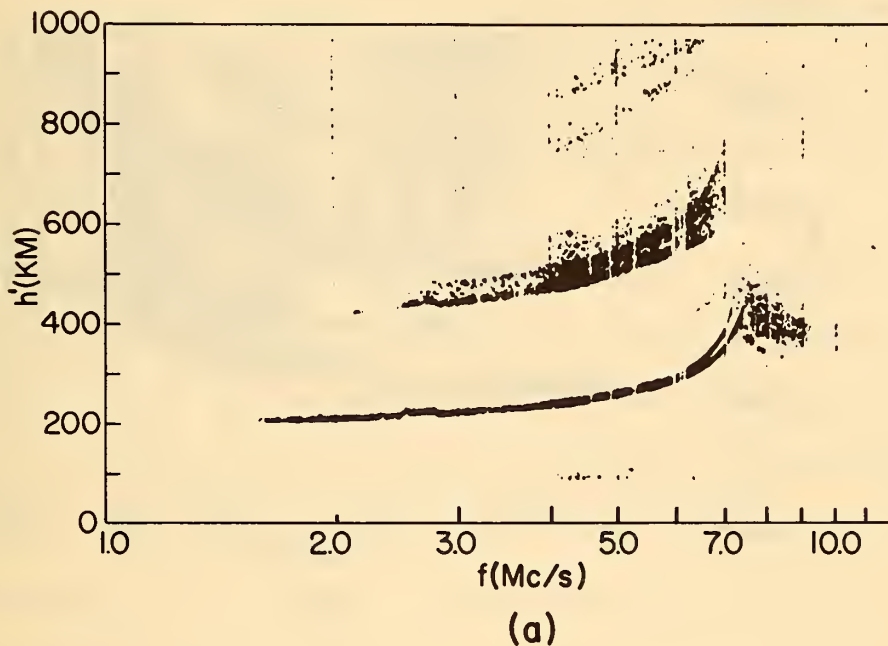
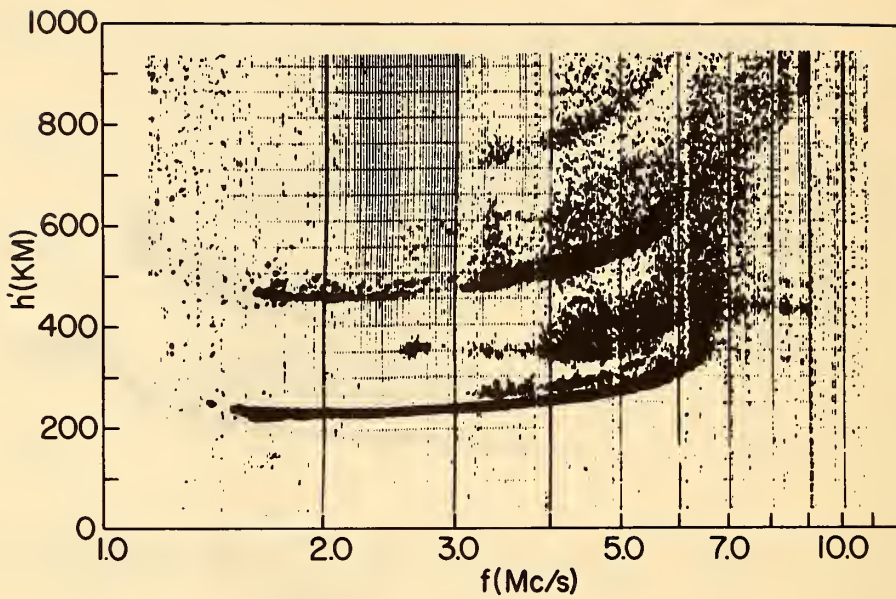
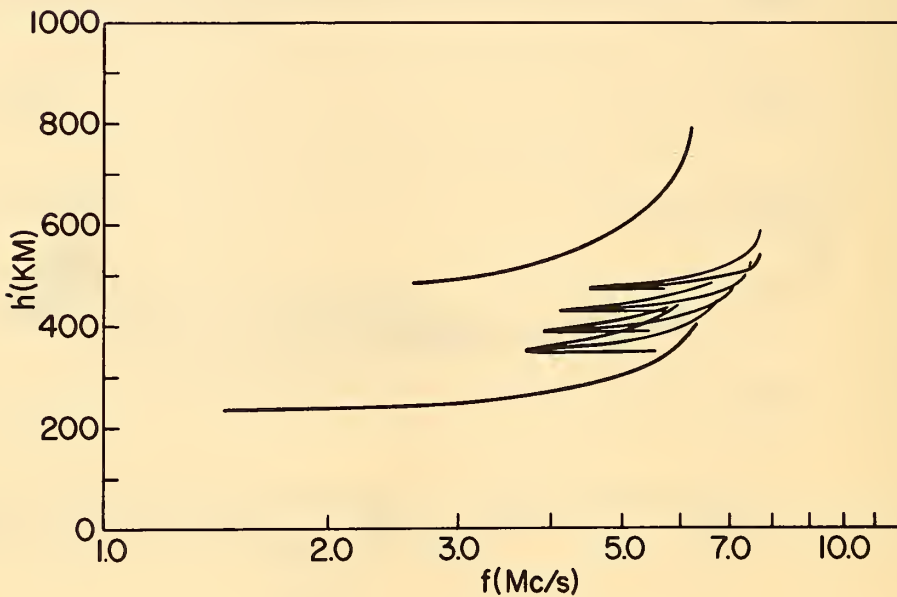


Figure 16. (a) Huancayo ionogram, recorded at 0100 EST, 15 October 1960, in which a configuration called 'feathers' occurs, and
 (b) The simulation of this ionogram. (The parabolic F layer used in this case has $h_o = 215$ km, $h_m = 305$ km, and $f_{oF} = 7.3$ Mc/s.)



(a)



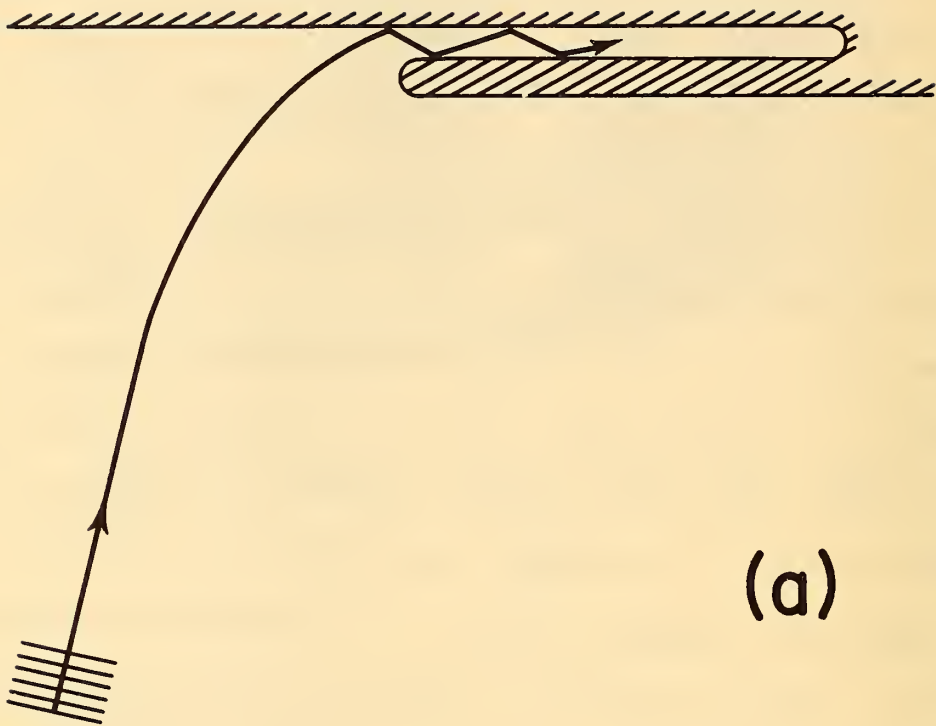
(b)

Figure 17. (a) Huancayo ionogram, recorded at 0015 EST, 17 June 1960, which exhibits a configuration similar to that of figure 2b, and
 (b) The simulation of this ionogram. (The parabolic \bar{F} layer used in this case has $h_o = 220$ km, $h_m = 320$ km, and $f_{o\bar{F}} = 6.8$ Mc/s.)

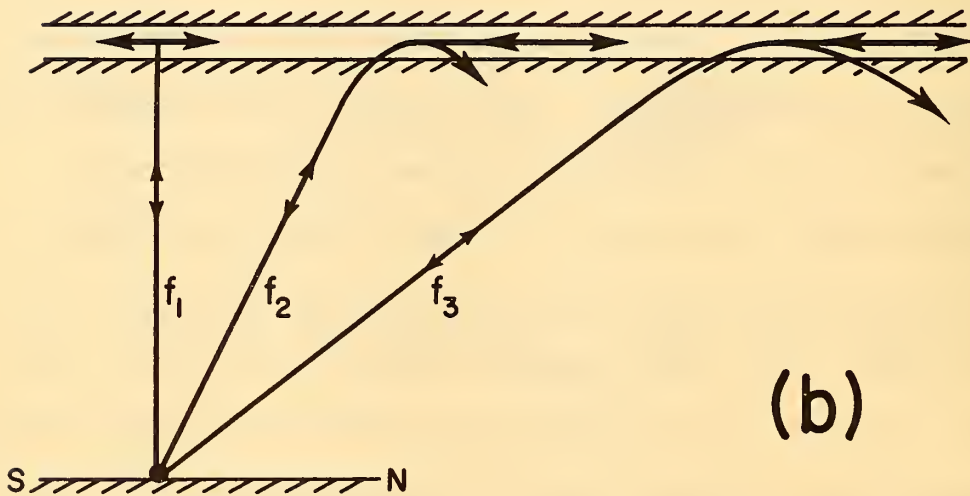
of 227 km and at ground distances of 250, 300, 350, and 400 km from the ionosonde. (The base of the F layer in this case was at a height of 220 km.) Thus this patch of irregularities had an east-west extent of 150 km.

The above interpretation of equatorial 'scatter' spread-F is made more convincing in part III where a sequence of ionograms is synthesized. For $1\frac{1}{2}$ hours a patch of spread-F irregularities, remaining at a constant height, moved first toward, then away from, the ionosonde. During the period of observation it covered a ground distance of 600 km with a constant velocity of 113 m/s.

Equatorial 'waveguide' spread F. An interpretation of the fourth equatorial spread-F configuration (figure 2d) has been proposed by Pitteway and Cohen (1961). The model, sketched in figure 18, invokes north-south ducts adequate to contain radio energy in a waveguide mode: The waveguide mode is excited by incident radio waves where they are propagating parallel to the duct (at the ray reflection level in the equatorial case). Radio energy in this waveguide mode then travels to the 'end' of the duct and is reflected. The reflected energy which leaks out of the duct near the original position of entry is then able to return to the ionosonde to form a spread echo. The delay for such echoes is thus the sum of the delay to the duct entry and the delay accumulated 'rattling around' within the duct. Each striation of the configuration is attributed to a separate duct; the portion with the greater delay attributed to more oblique propagation.



(a)



(b)

Figure 18. The equatorial 'waveguide' spread- \underline{F} model proposed by Pitteway and Cohen (1961): (a) Duct entry, and (b) Schematic ray paths for $f_3 > f_2 > f_1$.

In contrast with that of equatorial 'scatter' spread F, the oblique propagation of equatorial 'waveguide' spread F is north-south rather than east-west. The slight dip (2°) of the magnetic field at Huancayo, Peru appears to allow an easier entry into the ducts toward the south (figure 8).

The 'waveguide' irregularities are similar to the 'scatter' irregularities except that (1) they must have larger transverse dimensions and (2) they must have electron densities less than that of the ambient medium (to act as waveguides) and thus can only occur embedded in the layer.

Appendix A

TRANSFORMATION RELATIONSHIPS FOR BACKSCATTER TRACES

The equivalent range from an ionosonde to a scattering irregularity is

$$h' = \int_{\text{ray}} \mu' ds \quad (6)$$

where μ' is the group refractive index and ds is the element of path-length.

If the magnetic field is neglected, the dispersion relation has the form

$$\mu^2(f) = 1 - f_N^2/f^2, \quad (7)$$

where μ is the phase refractive index, f_N is the local plasma frequency, and f is the exploring frequency. It can be shown using

$$(7) \text{ that } \mu \mu' = 1. \quad (8)$$

From figure 19, it can be seen that

$$ds = dz/\cos \phi. \quad (9)$$

Substitution of (8) and (9) into (6) gives

$$h' = \int_{\text{ray}} |dz|/\mu \cos \phi = \int_{\text{ray}} |dz| (\mu^2 - \mu^2 \sin^2 \phi)^{-\frac{1}{2}}. \quad (10)$$

By Snell's law,

$$\mu \sin \phi = \text{constant} = \mu_A, \quad (11)$$

where μ_A is the index of refraction at the apex of the ray-path; i.e., from (7),

$$\mu_A^2 = 1 - f_A^2/f^2. \quad (12)$$

Substitution of (7) and (12) into (10) yields

$$h' = f \int_{\text{ray}} |dz| (f_A^2 - f_N^2)^{-\frac{1}{2}} \quad (13)$$

The integral of (13) is constant for rays that traverse the same height-interval as long as these rays have reflection-points at the same height (the height characterized by the plasma frequency f_A). Thus, for such a family of corresponding ray-paths, there is the relationship

$$h'/f = \text{constant}. \quad (14)$$

Let the subscript V refer to a ray at vertical incidence, and the subscript R refer to a corresponding ray at oblique incidence. Then from (14),

$$h'_V/f_V = h'_R/f_R. \quad (15)$$

Another useful relation may be derived by integration in terms of the horizontal coördinate. From figure 19,

$$ds = dx/\sin \phi, \quad (16)$$

so that (6) may be written, in view of equations (8) and (11),

$$h' = \int_{\text{ray}} dx/\mu \sin \phi = \int_{\text{ray}} dx/\mu_A = R/\mu_A, \quad (17)$$

where R is the ground distance of the irregularity. Substitution of $\mu_A = R/h'$ from (17) into (12) yields

$$h'^2 = (f_A/f)^2 h'^2 + R^2. \quad (18)$$

At oblique incidence, h' becomes h'_R , and f becomes f_R . Also, from (12), since normal-incidence reflection occurs where $\mu^2 = 0$,

$$f_A = f_V, \quad (19)$$

so that (18) becomes

$$h_R'^2 = (f_V/f_R)^2 h_R'^2 + R^2. \quad (20)$$

Using (15), this equation can be written

$$h_R'^2 = h_V'^2 + R^2 = h_V'^2 (1 + R^2/h_V'^2),$$

or

$$h_R' = h_V' (1 + R^2/h_V'^2)^{\frac{1}{2}} \quad (21)$$

Alternatively, (15) may be expressed, following (21) as

$$f_R = f_V (1 + R^2/h_V'^2)^{\frac{1}{2}}. \quad (22)$$

Equations (21) and (22) are recognized as the transformation used in the text, equations (4) and (5).

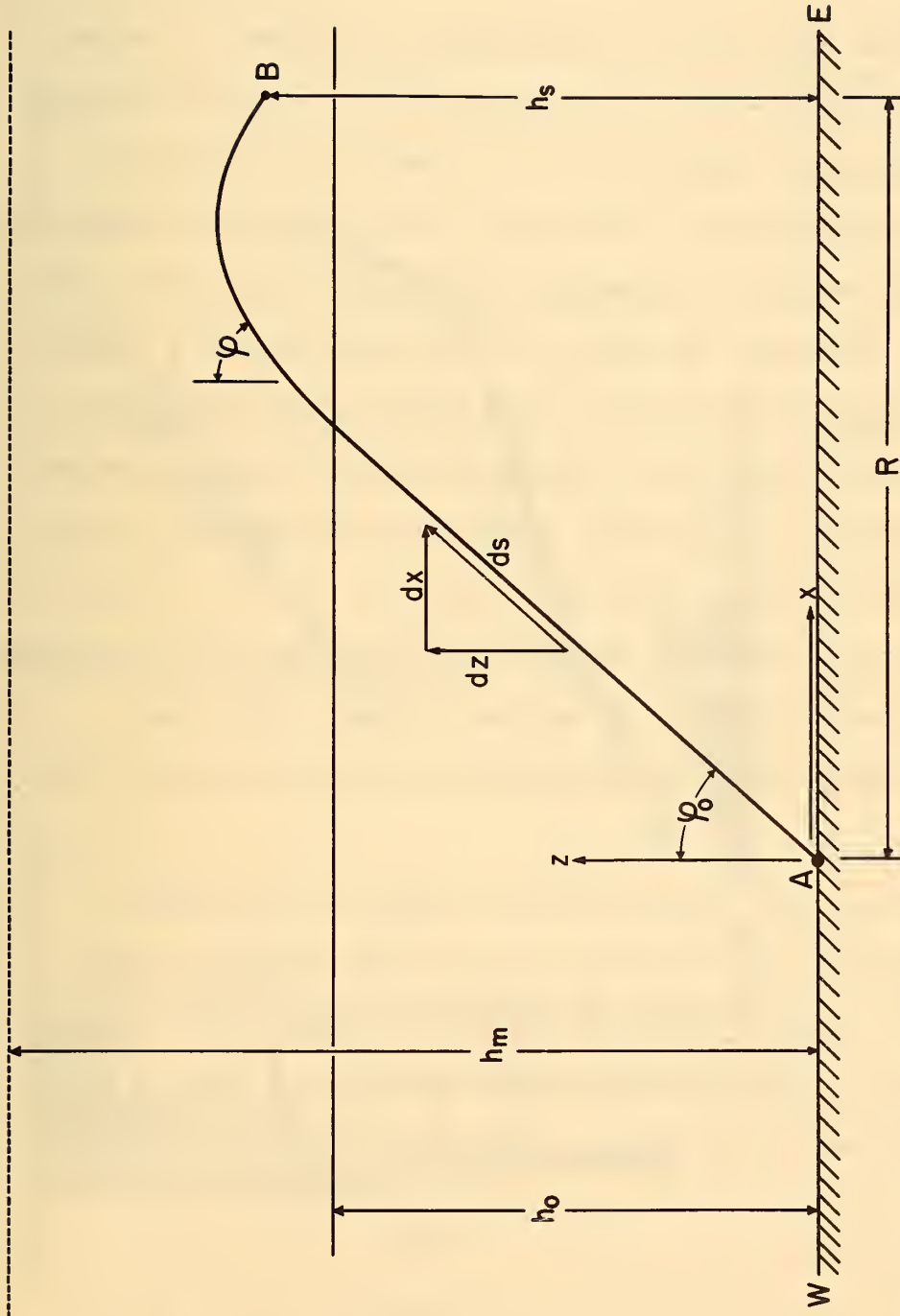


Figure 19. Ray-trajectory to an irregularity at point B in the vertical east-west plane from an ionosonde at point A. The height of the irregularity is h , its ground distance from the ionosonde is R , and the take-off angle of the ray is ϕ_0 . The 'base' of the F layer is at height h_0 , and its 'peak' is at height h_m .

Appendix B

THE SIMULATION OF EQUATORIAL SPORADIC E *

The above model for the interpretation of equatorial 'scatter' spread F applies as well to the interpretation of equatorial sporadic E. Figure 20 shows the typical equatorial sporadic E configuration observed at Huancayo, Peru. Two parts of this configuration have been classified: 'equatorial sporadic E' (q-type) and 'equatorial slant sporadic E' (s-type). The former is the diffuse trace at a constant equivalent range of about 100 km. The latter is the diffuse trace emerging from the former at a low frequency and rising in equivalent range proportional to frequency. No term has been adopted for the spread echoes bounded by these two traces.

It was shown by Cohen, Bowles, and Calvert (1962) that the echoes comprising the q-type trace arrive from overhead, while those comprising the s-type trace arrive from a considerable angle to the vertical.

There is strong evidence for thin, magnetic-field-aligned irregularities in the ionization of the E layer (Bowles and Cohen, 1962a, 1962b; Cohen, Bowles, and Calvert, 1962; Egan, 1960; Bowles, Cohen, Ochs, and Balsley, 1960; etc.). They are the order of 6m by 200m in size and lie in the region between 95 and 110 km height.

* The content of this appendix was presented to URSI at the May 1961 meeting by Dr. Cohen and subsequently published (Cohen, Bowles, and Calvert, 1962).

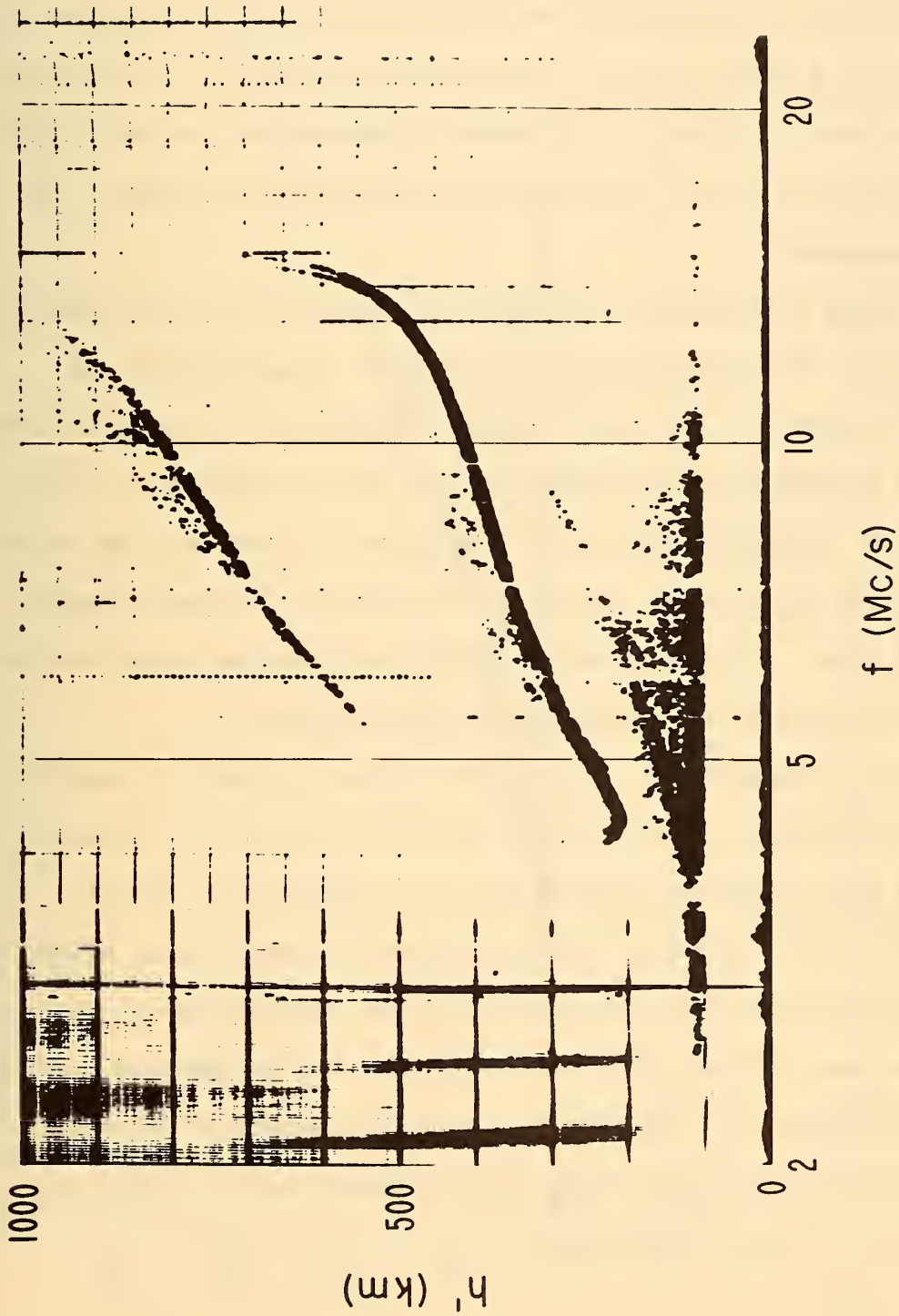


Figure 20. Huancayo ionogram recorded at 1229 EST, 19 April 1960. It exhibits a typical equatorial sporadic E configuration.

Equatorial sporadic E is interpreted as scattering by a thin stratum of irregularities at E-region heights. In order to produce the observed (s-type) slant trace, this stratum must be embedded in the equatorial E layer below its peak ionization density. This situation is simulated in figure 21 for several irregularities located slightly above the base of the E layer and at various ground distances from the ionosonde.

Figure 21 faithfully reproduces the width of the slant trace of figure 20. The upper envelope of the trace is generated by the 'triple-points' of the individual configurations as the ground distance of the irregularities is increased. The edge is expected to be enhanced on the ionogram, since it corresponds to scattering at the ray reflection level, where the ray paths converge. The lower envelope of the trace is formed as the caustic focus (like the ground-scatter caustic focus) of the center traces of the 'triplets'.

This interpretation of equatorial sporadic E predicts that the upper envelope of its slant trace should be linear (i.e. its equivalent range should be proportional to its frequency). This is a direct result of the projection involved in transforming, after equations (4) and (5), echo delays from the overhead case to the oblique case. Figure 22 shows this feature for the observed slant trace in figure 20. The linearity of slant-sporadic-E traces has been noticed previously by Agy (private communication to Smith and Knecht, 1957) and by Whale (1951).

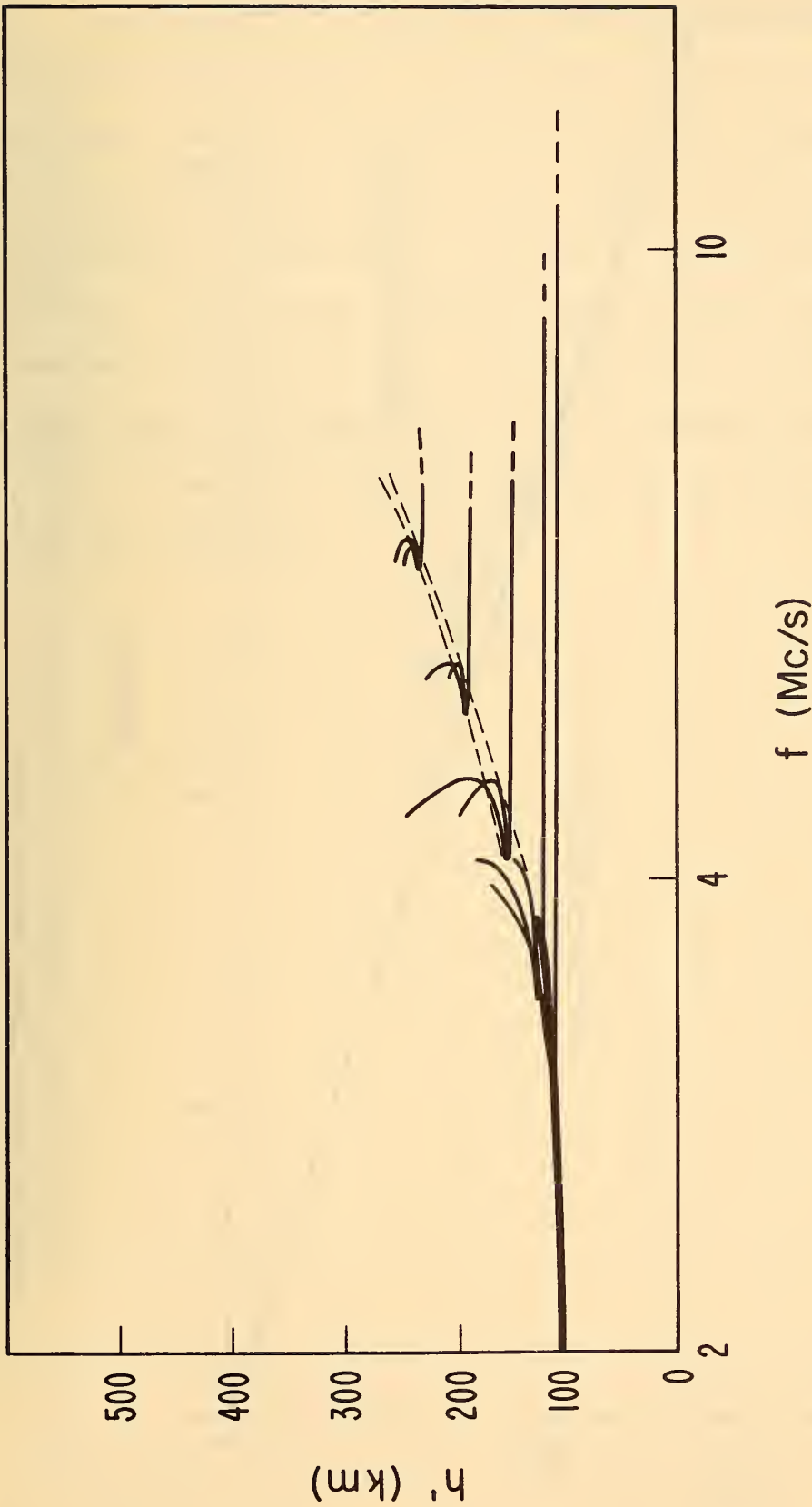


Figure 21. Superposition of the individual 'ionograms' corresponding to scatterers embedded in the E layer below its height of maximum electron density. The scatterers are taken to be at a height of 105 km and at ground distances of 0, 50, 100, 150, and 200 km. The E layer assumed for this figure and figure 23 is parabolic with its base at 100 km and a peak plasma frequency of 4.0 Mc/s at 114 km.

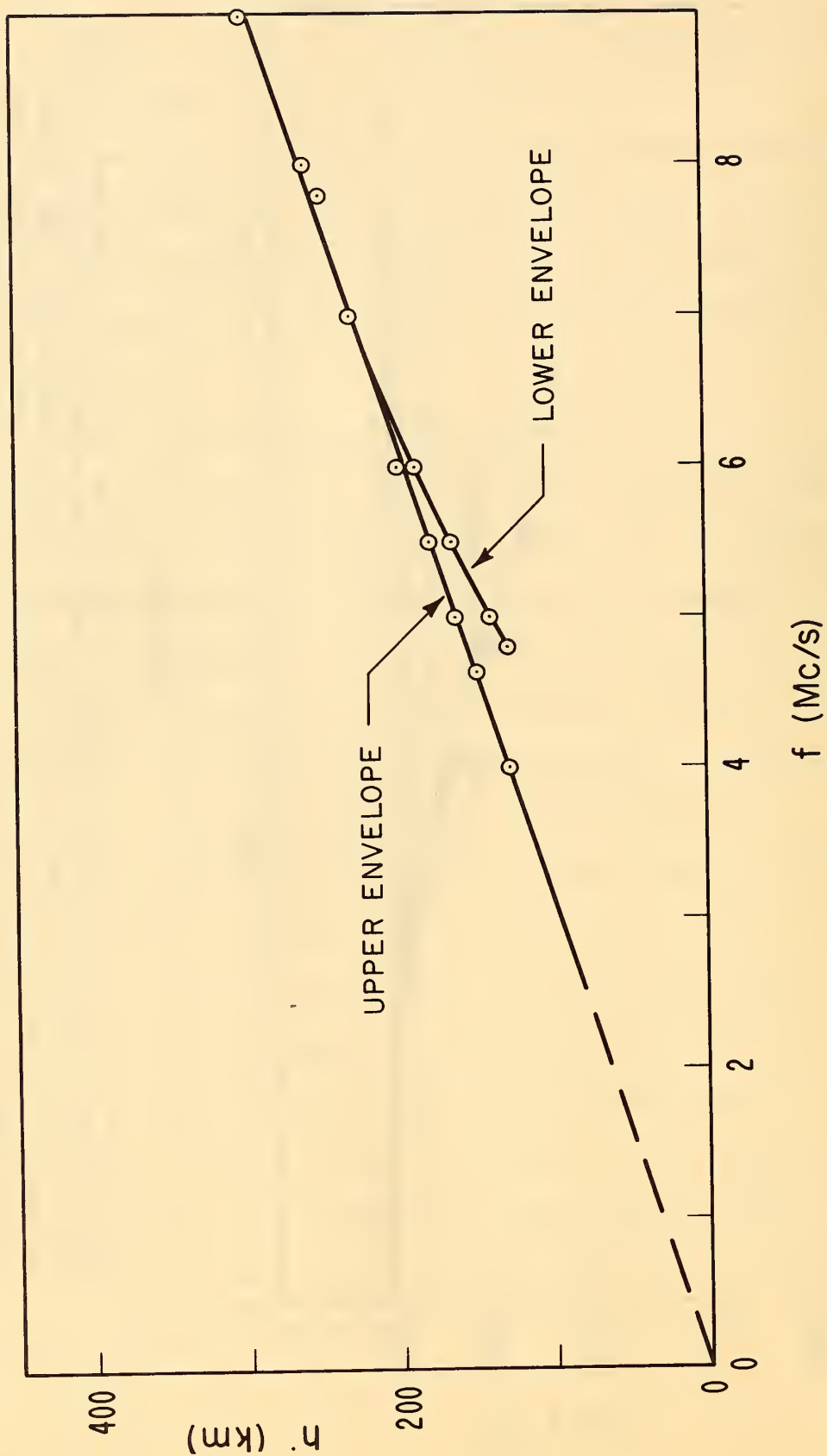


Figure 22. The upper and lower envelopes of the 'equatorial slant sporadic E' trace of figure 20, replotted with a linear frequency axis.

The simulation of the equatorial sporadic-E configuration may be carried a step further by accounting for the relative strength of the echoes. Figure 23 was produced by adjusting the density of points (each produced by an electronic computer and plotted automatically) proportional to an estimate of the expected echo intensity. This estimate considered attenuation with distance, ionospheric defocusing of rays, and the efficiency of scattering (Cohen, Bowles, and Calvert, 1962). There is striking agreement between this synthesized configuration and that of the observed equatorial sporadic E.

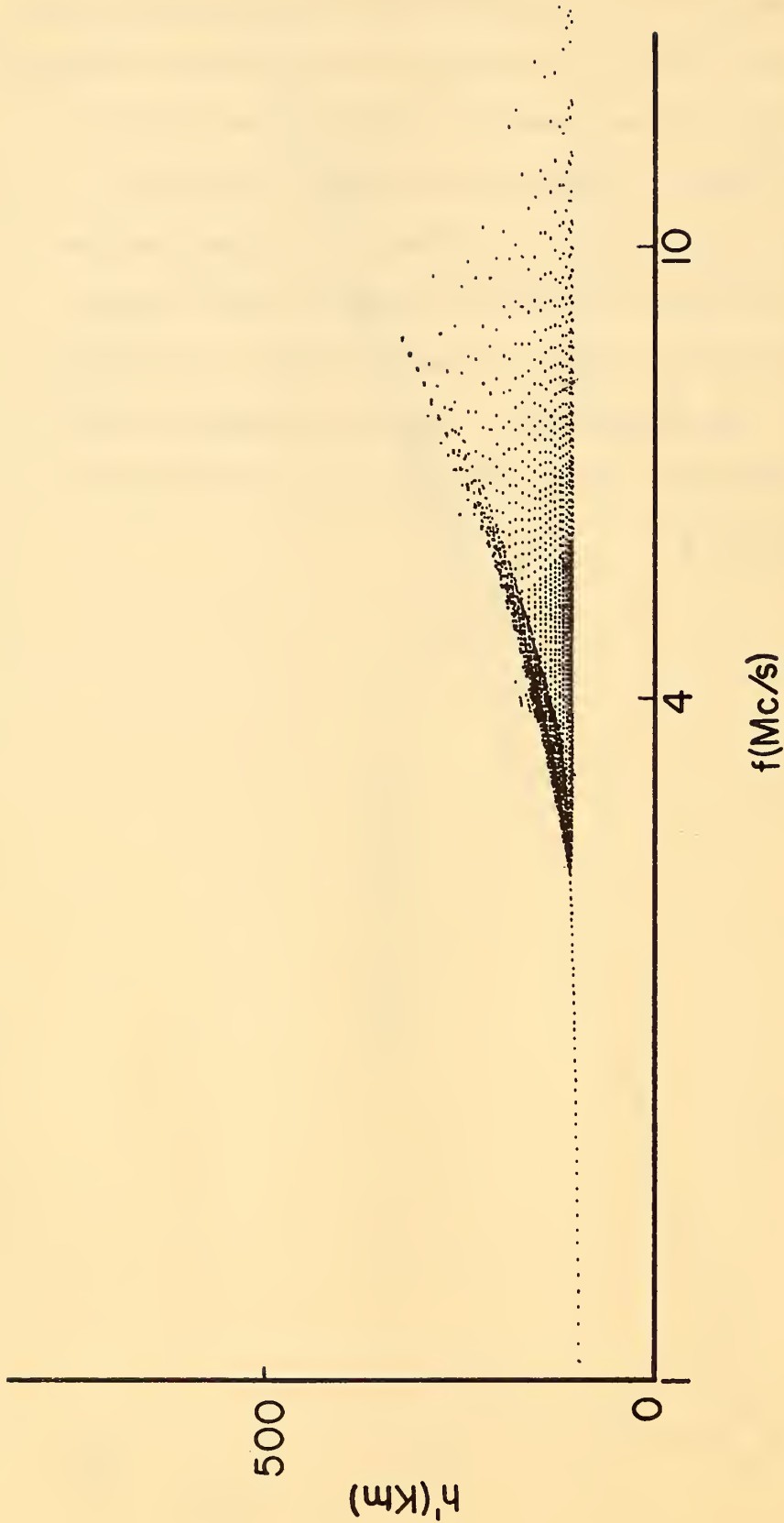


Figure 23. Simulation of the equatorial sporadic E configuration. Scattering irregularities were assumed to be at a height of 105 km and to extend as far as 300 km on either side of the ionosonde. The separation of points is adjusted (beyond a cutoff) to be inversely proportional to the expected echo intensity.

Part III

SPREAD-F MOTIONS *

Methods of observation. The motions of F-layer irregularities are often detected through the observation of radio diffraction patterns moving along the ground. Radio stars and local radio transmitters are commonly-used sources of radio waves. With this technique, fluctuations in the signals received with spaced antennas are displaced in time and compared for similarity. The time displacement giving the greatest correlation, combined with the known separation of the antennas, thus determines the velocity of the moving irregularities.

Another technique revealing F-layer motions is that of following large-scale ionospheric distortions as they occur at spaced ionosondes. These "traveling disturbances", observed extensively at temperate latitudes, appear to possess many features of wave motion.

The two techniques above are discussed more fully by Ratcliffe and Weekes (1960.)

In this part, three techniques are discussed which reveal the motions of spread-F irregularities. They involve (1) the analysis of ionograms recorded at a single station, (2) the timing of the occurrence of spread F at spaced ionosondes, and (3) the measurement

* Here the term "motion" implies the horizontal movement of ionospheric structure (ripples, distortions, irregularities, patches of irregularities, etc.).

of the doppler shift of radio waves scattered by spread F irregularities.

Spread-F simulation. In part II the position of spread-F irregularities in the east-west plane was determined from the configuration of spread F at a single ionosonde. From a sequence of ionograms it is thus possible to study the east-west motion of patches of equatorial 'scatter' spread-F irregularities.

As an example of this technique, figure 24 shows two ionograms recorded 17 minutes apart, together with their partial syntheses (i.e. those computed as if the patch were a single irregularity). A height of 261 km and ground distances of 460 and 340 km give good agreement. The additional traces in these diagrams above the second and third multiples of the F-layer trace are attributed to propagation paths involving additional F-layer and ground reflections en route to the scattering region. They are indicated by dashed curves in the simulations and were calculated for one (the lower) and two (the upper) additional ground reflections. Five more ionograms of this $1\frac{1}{2}$ -hour sequence were analyzed. The height of the patch of irregularities remained constant, and its ground distance varied as shown in figure 25. The linearity of this plot indicates that the velocity was constant, and the slope indicates that its east-west component was 113 m/s.

Figure 26 presents spread-F velocity measurements obtained by this technique for sunspot maximum (1958-1960) data from Huancayo, Peru and Natal, Brazil. A nocturnal trend is apparent in these results. The velocities decrease with time of night from about 200 m/s at 2100 LT to about 80 m/s at 0600 LT. A few velocities of 100 m/s

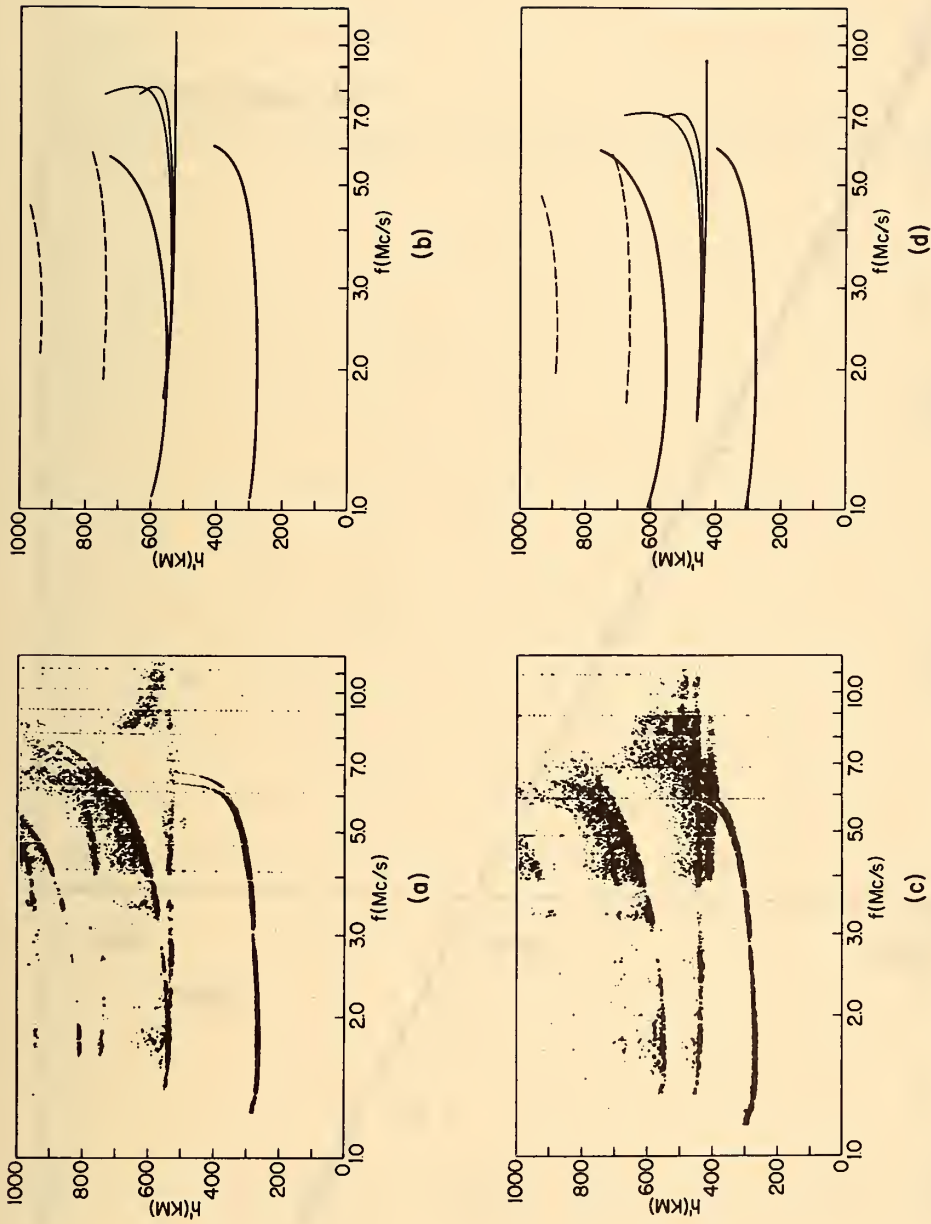


Figure 24. (a) Huancayo ionogram recorded at 0258 EST, 23 June 1960. (b) Simulation of this ionogram with an irregularity at a height of 261 km and at a ground distance of 460 km. (c) Huancayo ionogram recorded 17 minutes later than (a). (d) Simulation of this ionogram, with an irregularity at a height of 261 km and at a ground distance of 340 km. A rectangular \underline{E} layer extending from 100 km to the base of the \underline{F} layer, with $f_{O\underline{E}} = 0.62$ Mc/s; plus a parabolic \underline{F} layer with $h_o = 260$ km, $h_m = 330$ km, $f_{O\underline{F}} = 6.2$ Mc/s was used in the calculations.

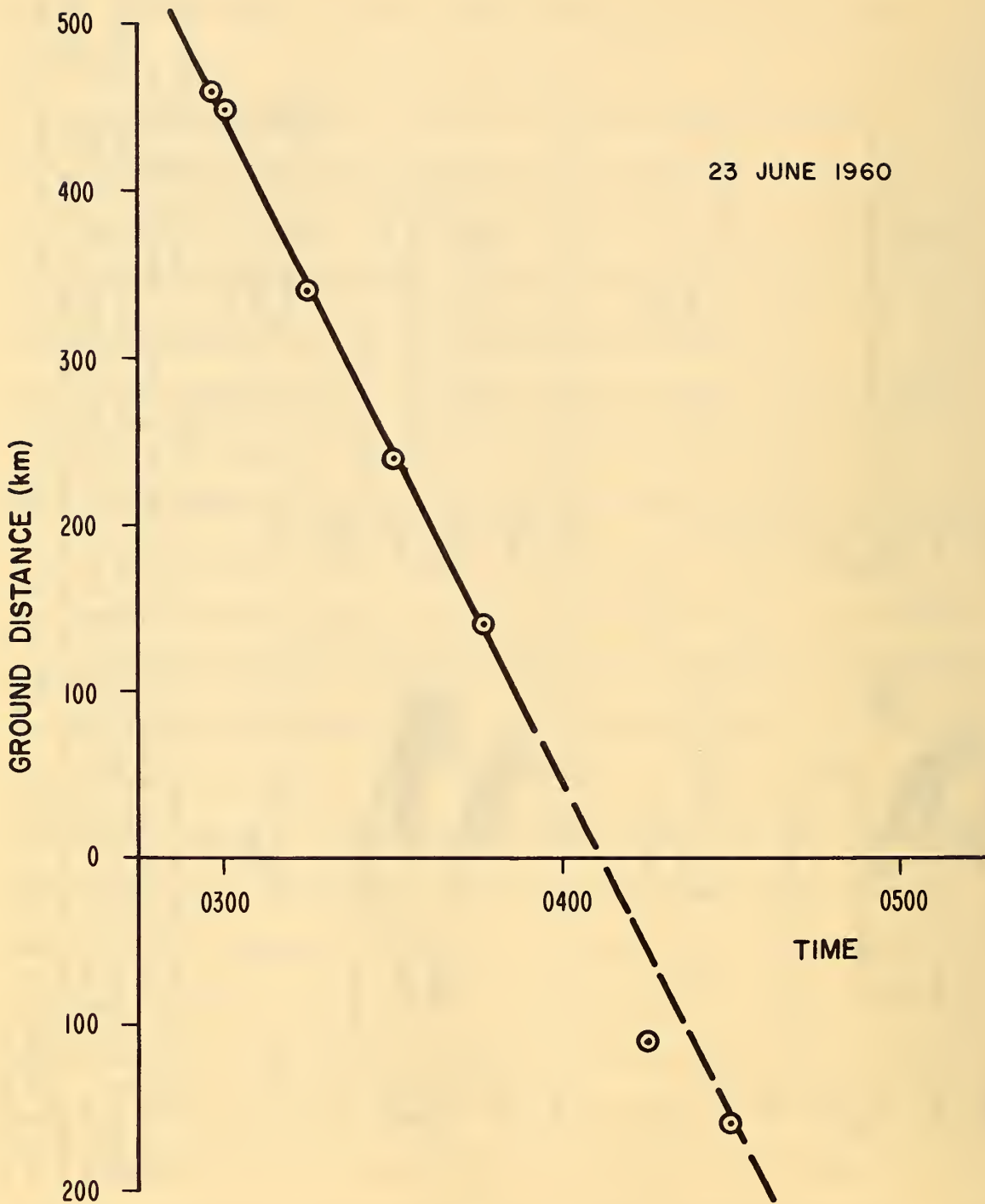


Figure 25. The ground distance of a patch of irregularities plotted against the local time of the Huancayo ionogram simulated. (The first and third points result from figure 24.)

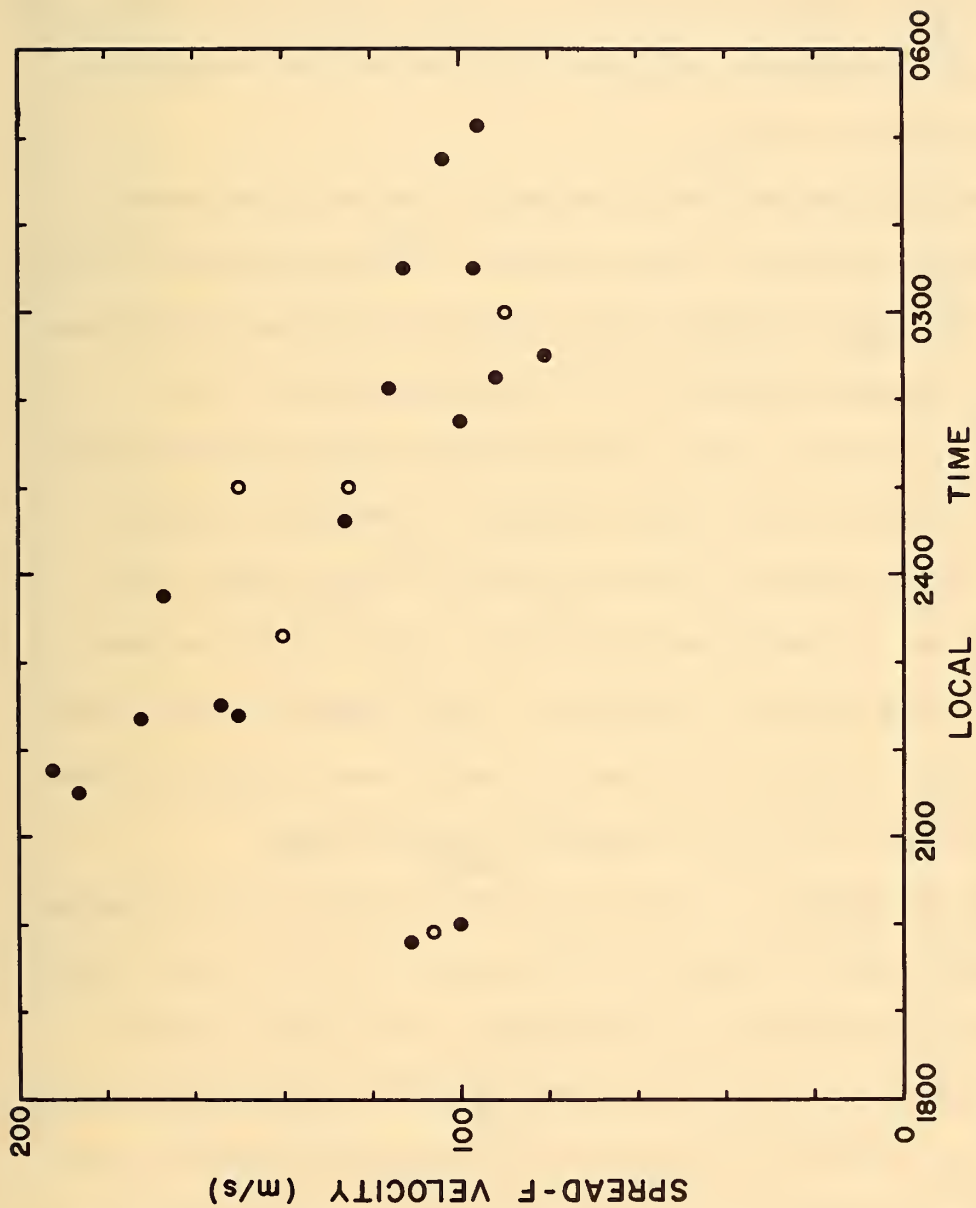


Figure 26. Spread-F velocities at sunspot maximum derived from Huancayo ionograms (filled circles) and Natal ionograms (open circles).

occurred prior to 2100 LT. The trend agrees remarkably well with the spaced-receiver observations of Skinner, Hope, and Wright (1958).

Figure 27 presents similar measurements for sunspot minimum (1955-1956) data from Huancayo, Peru. In this case the nocturnal trend is considerably moderated, with the velocities varying through the night from 130 m/s to 60 m/s.

Further data are required to establish whether these spread-F motions are east-to-west or west-to-east. The transequatorial scatter experiment of Cohen and Bowles (1961) provided such data for motions at Huancayo between December, 1957 and November, 1958. This experiment (described in part I) employed beam antennas which limited the scatter volume to that shown southwest of Huancayo in figure 6. The sense of the motions are thus indicated by which occurs first, the enhancement of transequatorial scatter signals or the overhead passage of irregularities at Huancayo. Of the spread-F motions which could clearly be sensed in this manner (eight cases occurring between 2130 LT and 0600 LT) all were directed toward the east.

Spaced ionosondes I. From the routine scalings of IGY ionograms, Knecht (1960, 1962) has found that the onset of spread F often occurs in sequence along the chain of ionosondes in Peru (See figure 6.). With the assumption that this is a manifestation of spread-F motions, the delay in onset and the spacing of the ionosondes yield the north-west-southeast component of the spread-F velocity. With the further assumption that the motion is along the magnetic equator (inclined some 37° to the chain of ionosondes), the observed delays are consistent with the spaced-receiver measurements of Skinner, Hope, and

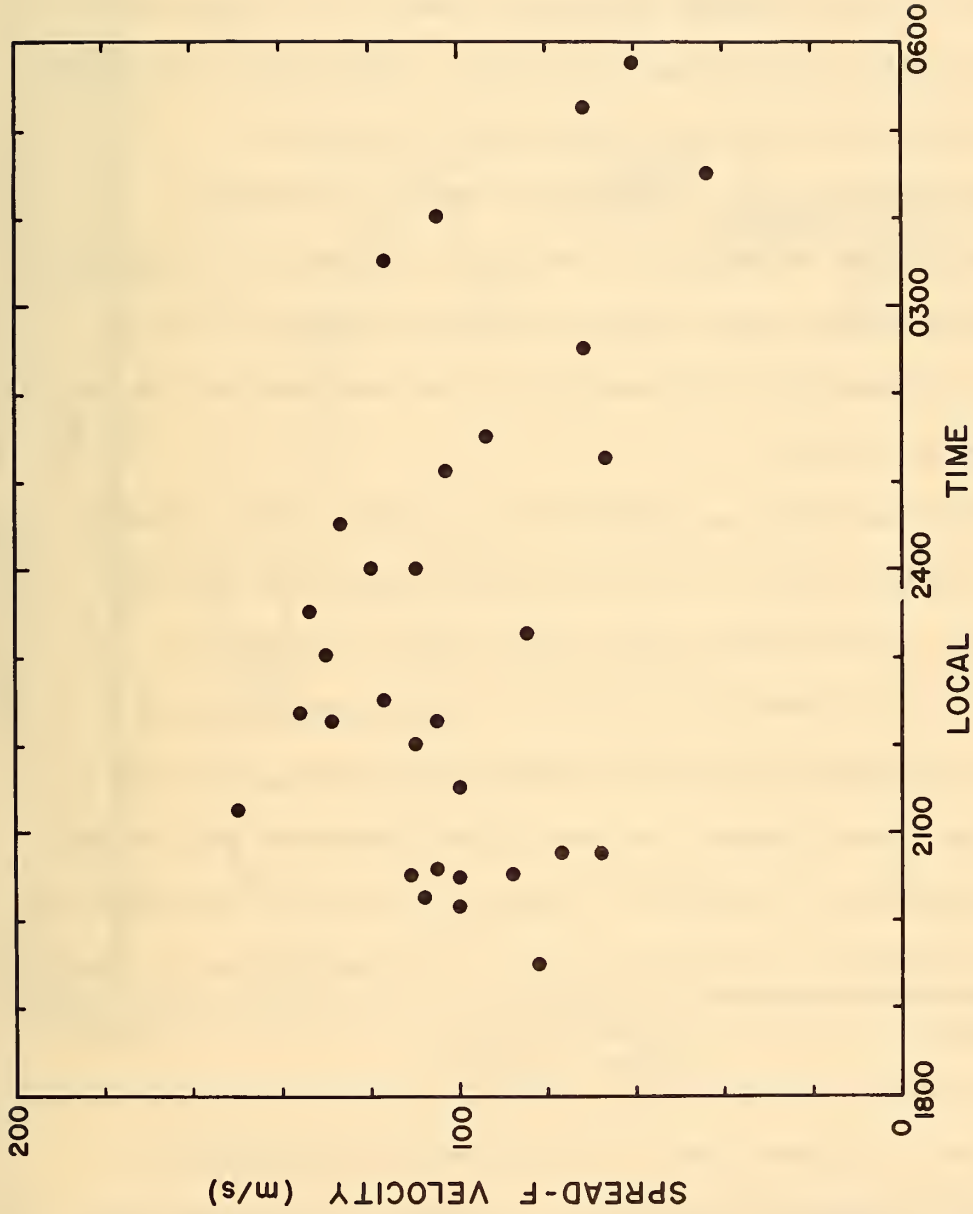


Figure 27. Spread-F velocities at sunspot minimum derived from Huancayo ionograms.

Wright (1958) and with the velocities determined above by the simulation of spread F. The results of Knecht's analysis for September 1958 are reproduced in figure 28. The 15-minute interval between observations introduces the large scatter in the measurements and causes the tendency to group about certain velocities. Nonetheless, the trend toward lower velocities later in the night is apparent.

Spaced ionosondes II. Provided the patches of spread-F irregularities last long enough, the above technique may be applied to stations more widely spaced along the magnetic equator. Such an analysis is presented in this section for two stations--at Huancayo, Peru and Natal, Brazil.

Huancayo and Natal are separated by the whole width of South America, roughly 4400 km. With the spread F velocities thus far determined, it should take roughly eight hours for spread-F irregularities to travel this distance. Thus evening spread F at Huancayo was compared with morning spread F at Natal. This pair of stations was chosen because they use similar ionosondes and similar scaling techniques. The latter is important, since the occurrence of spread F was taken to be that indicated in the tabulations of ionospheric data produced as a routine of the station.

The occurrence of spread F at the two stations was compared by counting the coincidences and contradictions corresponding to a given delay between their observation. Monthly totals were then recorded as contingency tables of the form below.

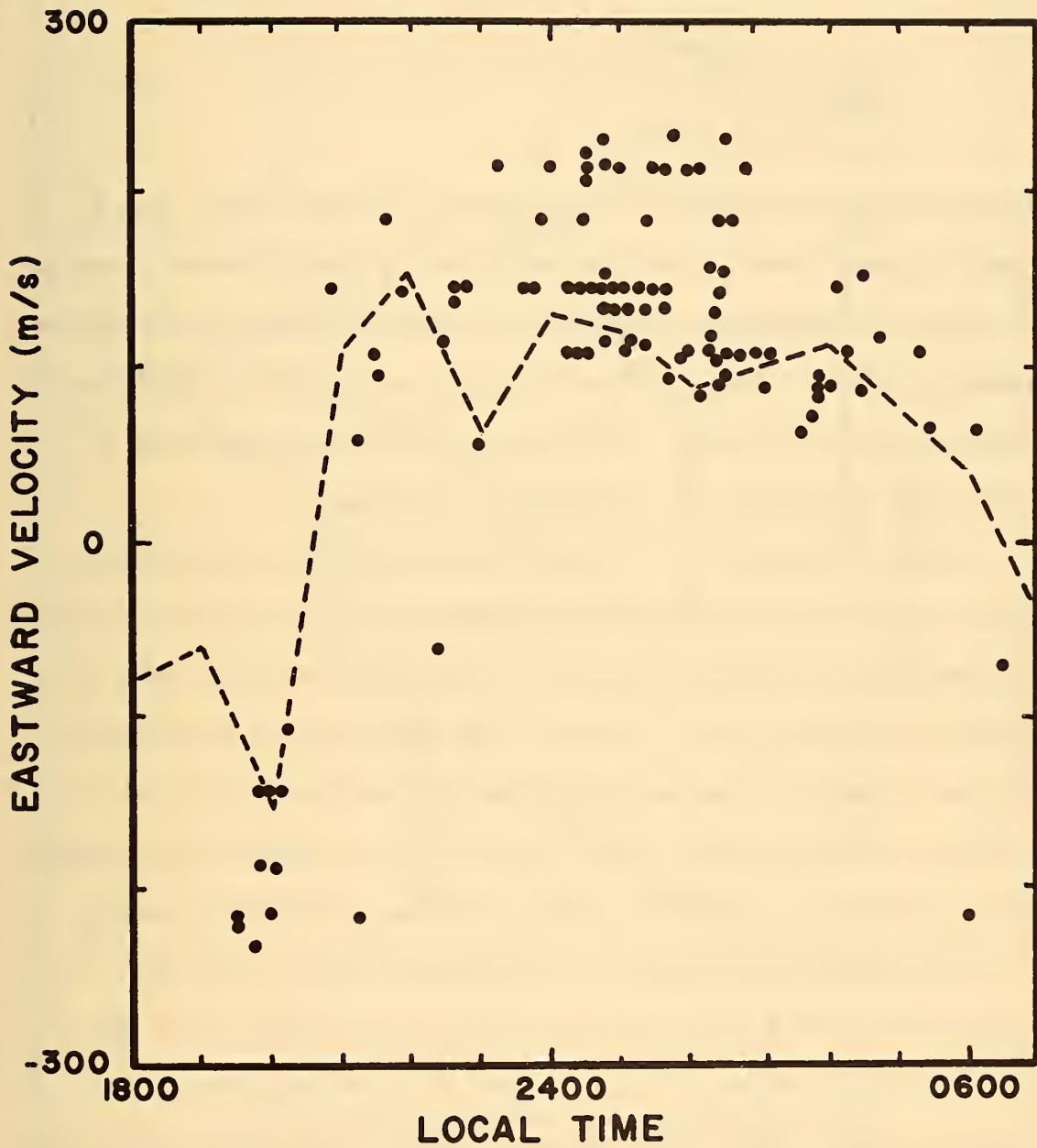


Figure 28. The spread-F velocities determined by Knecht (unpublished material) compared with the spaced-receiver measurements obtained at Ibadan, Nigeria (dashed) by Skinner, Hope, and Wright (1958).

		Huancayo, Peru	
		Spread <u>F</u>	No spread <u>F</u>
Natal, Brazil	Spread <u>F</u>	<u>a</u>	<u>b</u>
	No spread <u>F</u>	<u>c</u>	<u>d</u>

The correlation indicated by this scheme is positive when a and d greatly exceed b and c, negative when b and c greatly exceed a and d. The degree of correlation implied by a given contingency table may be measured by the probability that the distribution within the table occurred purely by chance. When this is large the correlation is weak; when it is small the correlation is strong.

Figure 29 shows the contingency-table probability associated with various delays between spread-F observations. October, 1958 data recorded for the hours 2000-2300 LT (evening set) and 0200-0600 LT (morning set) were used. The solid line indicates the correlation between spread F in the evening at Huancayo and spread F in the following morning at Natal. For comparison, the dashed line indicates the corresponding correlation between evening and morning spread F at the same station (Huancayo). The Huancayo-Natal correlation becomes very strong with a three-hour delay and reaches a maximum with a five-hour delay. The sharp drop in correlation beyond the five-hour delay results from the sun's rising at Natal and attenuating spread F. For this reason, the delay corresponding to the peak correlation does not represent an average transit time for the spread-F irregularities. The excellent correlation at the peak of the graph

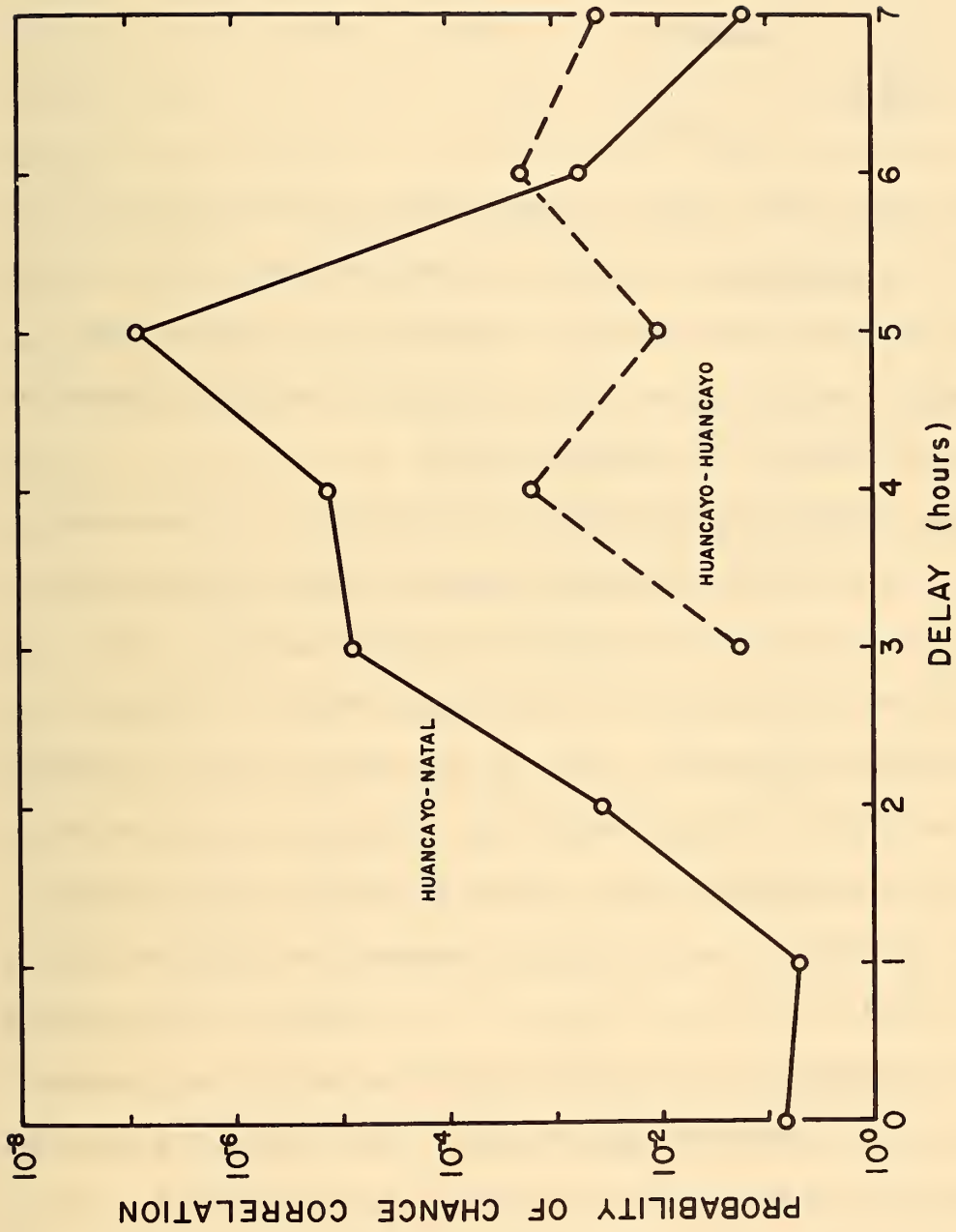


Figure 29. The correlation of evening spread \bar{F} at Huancayo with morning spread \bar{F} at (1) Natal and (2) Huancayo.

(10^{-7} probability) was obtained from the contingency table below.

		Huancayo, Peru	
		Spread <u>F</u>	No spread <u>F</u>
Natal, Brazil	Spread <u>F</u>	19	0
	No spread <u>F</u>	14	30

The zero in this table seems to indicate that evening spread F at Huancayo is a prerequisite of morning spread F at Natal. The mechanism ultimately responsible for spread F thus operates only near sunset, since the spread F observed later in the night appears to occur only by virtue of its eastward motion.

Doppler-shifted oblique scatter. This section is a preliminary analysis of data from an experiment performed under the auspices of the Voice of America and the National Bureau of Standards. This experiment was conducted by Dr. K. Davies and Father J. R. Koster during September and October, 1961. It involved an oblique propagation path between Tripoli, Libya (transmitter) and Accra, Ghana (receiver). The 20 Mc/s transmitted frequency was controlled by a highly stable oscillator at Tripoli, and the received frequency was compared with that of a similar oscillator at Accra. In this manner, it was possible to detect the relatively small doppler shift imposed by the ionosphere and record it on slow-moving magnetic tape. Upon playing the tape at full speed (1500 times the recording speed) doppler shifts of a few cycles per second are transformed into audio frequencies acceptable to standard audio-frequency spectrum analyzers. Davies, Watts, and Zacharisen (1962) have discussed this technique in greater detail.

Figure 30 presents some examples of nighttime doppler shifts as they appear in the result of the spectrum analysis. The doppler-shift frequency increases upward, and time increases to the right. In these figures, the daytime signal, visible at the far left, is narrow; having a width the order of 0.2 c/s. Just after sunset this often gives way to very broad signals which may cover as much as 18 c/s. The broad signals occurring before midnight usually consist of striations sloping downward to the right.

The large nighttime doppler shifts are attributed to spread-F motions occurring near the southern terminal of the path where it crosses the magnetic equator. The largest doppler shifts arise by scattering from spread-F irregularities when they are first observed west of the path. As the eastward velocity of a given spread-F patch carries it closer to the path, the component of the motion producing doppler shifts decreases, and hence the patch appears as a sloping band on the records. This interpretation is further strengthened by the fact that broad signals fail to develop on evenings following strong magnetic disturbances--a well-known feature of spread-F occurrence.

Since no absolute frequency calibration was attempted, a reference frequency for the doppler shifts is lacking. However, its position on the records may be estimated where the narrow signal corresponding to normal propagation is superimposed (e.g. 27-28 Sept., 29-30 Sept., 6-7 Oct.; figure 30). Assuming that such narrow signals are not appreciably doppler shifted leads to the feature that spread-F irregularities appear to approach the path but not leave it. This will

TRIPOLI → ACCRA 19.904 Mc/s

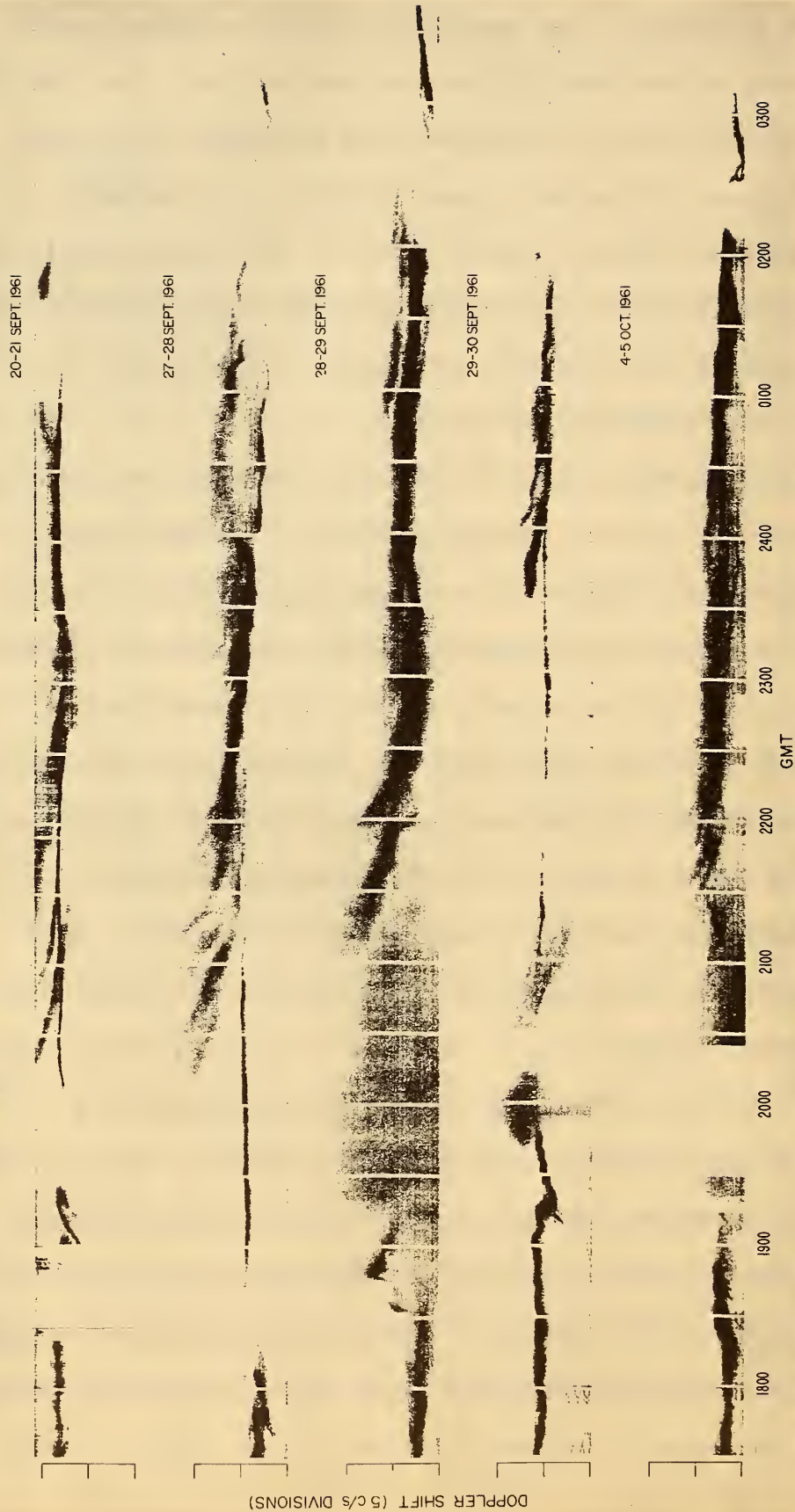


Figure 30a. Nighttime doppler shifts attributed to equatorial spread F.

TRIPOLI → ACCRA 19.904 Mc/s

5-6 OCT. 1961

6-7 OCT. 1961

11-12 OCT. 1961

12-13 OCT. 1961

14-15 OCT. 1961

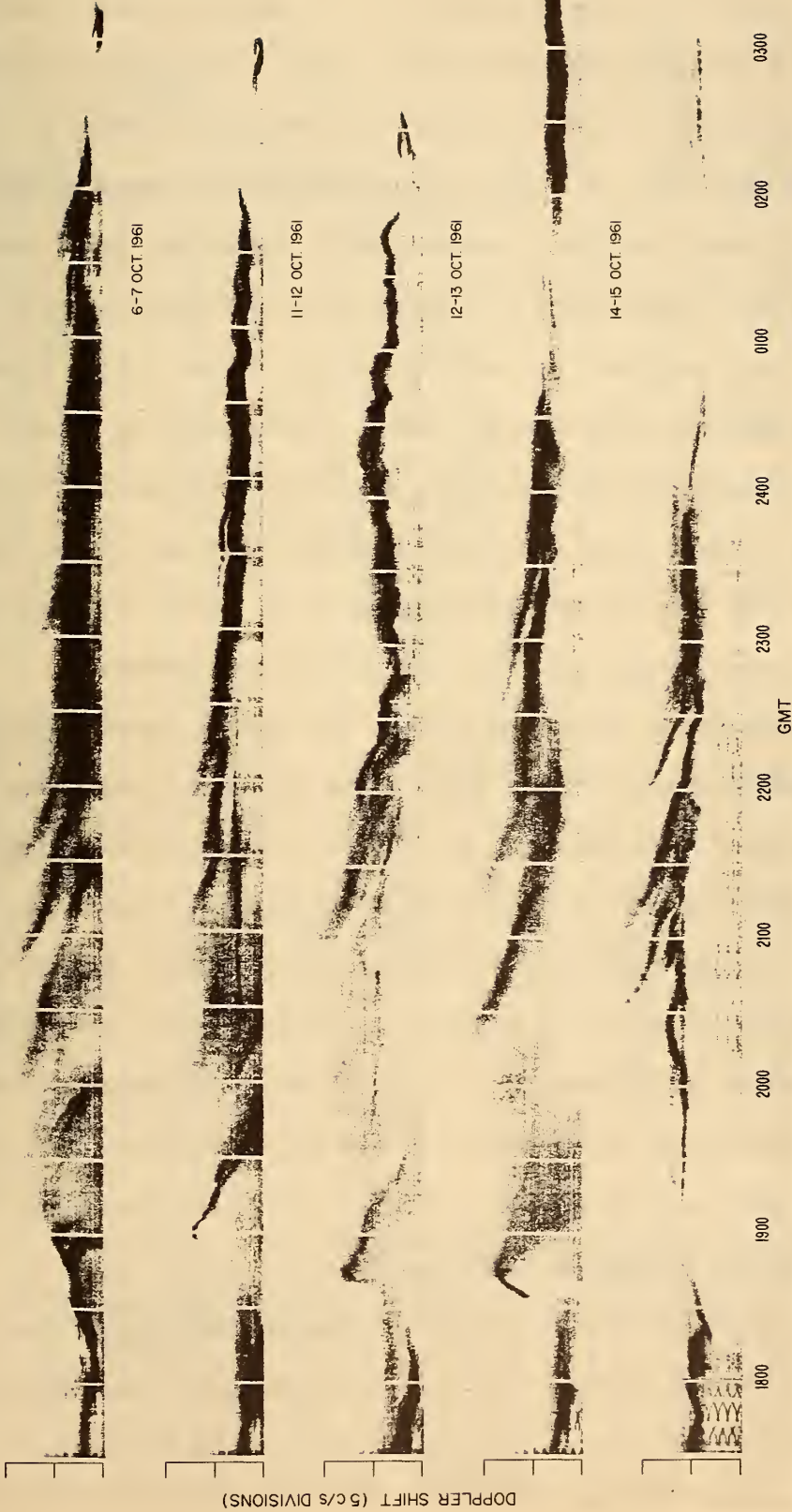


Figure 30b. Nighttime doppler shifts attributed to equatorial spread F.

be attributed to the aspect-sensitivity of the spread-F scattering.

Since spread-F irregularities are thin and long, radio waves will be scattered strongest when they add in phase from the whole length of the irregularity. In other words, the irregularity must be oriented so that there is phase coherence along its length. For the simple case where ionospheric refraction is neglected, phase coherence occurs when the irregularity is tangent to an ellipsoid of revolution having the path terminals as foci (since this is the figure on which the path length has a stationary value). Since spread-F irregularities are magnetic-field aligned, and their orientation is thus fixed, they produce phase coherence only when they are in the proper places. In the case of the Tripoli-Accra path, which crosses the magnetic equator, phase coherence is possible for spread-F irregularities above the ground only in two sectors--those roughly northwest and southeast of the point where the path crosses the magnetic equator. Furthermore, the latter sector is also excluded because F-layer heights there are below the horizon from Tripoli.

Figure 31 shows the positions where phase-coherent scattering should be detected with this experiment and the simple model above. The solid curves correspond to irregularities at the heights indicated, and the dotted curve is the limit imposed by the horizons from the two terminals. The approximations involved in this calculation are indicated in the derivation, Appendix C.

Figure 31 does not appear to be consistent with the sloping striations apparent in figure 30. It would predict, from the fact that its constant-height contours are nearly parallel to the path,

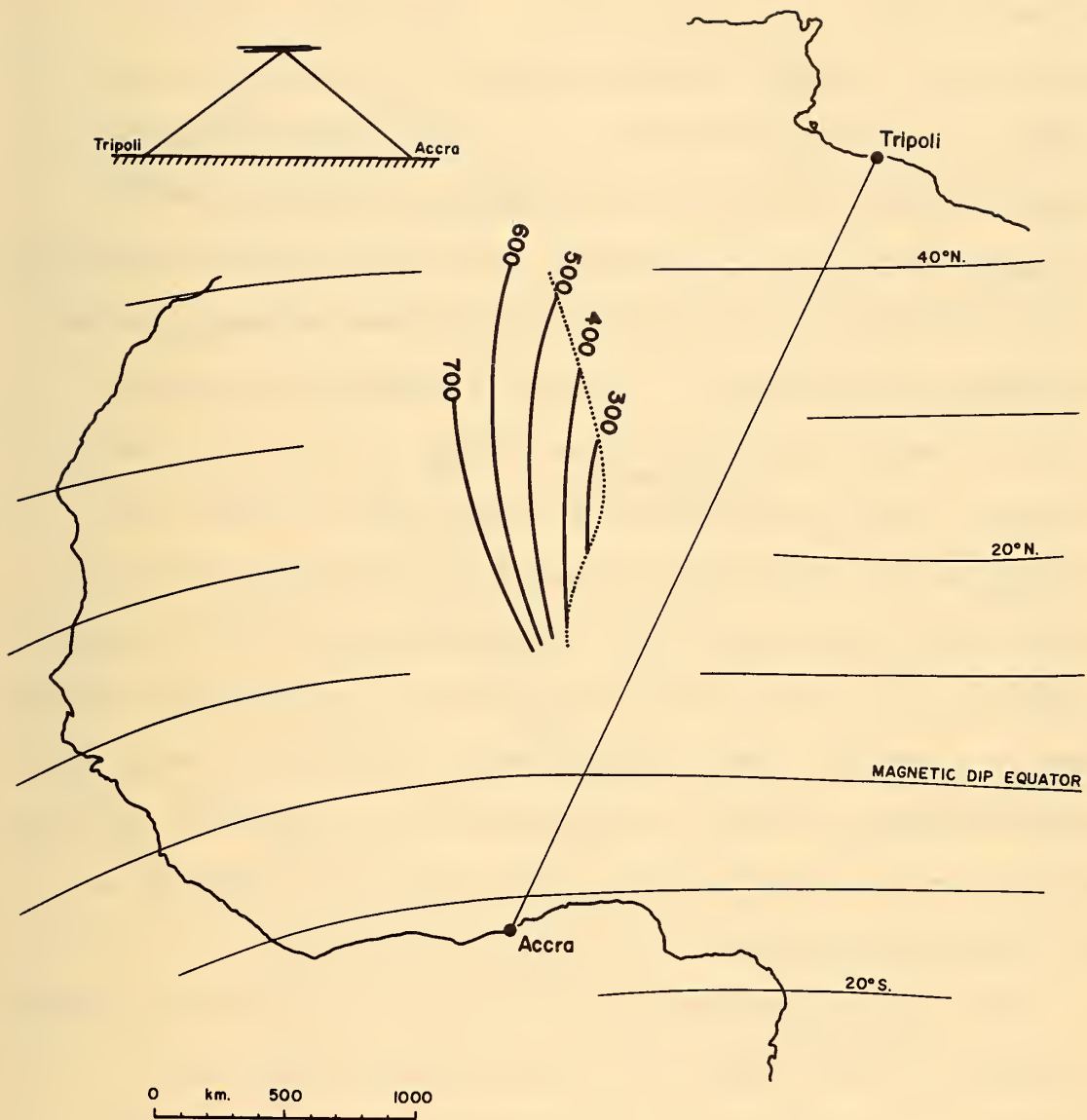


Figure 31. The height at which spread-F irregularities would produce phase-coherent echoes on a one-hop model. This figure and figure 32 are based on magnetic charts of the U. S. Hydrographic Office.

that thin patches of spread-F irregularities should give rise to a relatively constant doppler shift corresponding to the off-path distance and the velocity of the irregularities. Furthermore, concurrent results from an oblique ionosonde experiment (similar to vertical sounding, but with the transmitter and receiver separated) between Tripoli and Accra indicated that the doppler shifts should be associated with two-hop transmission, rather than one-hop transmission. It appears from this, and from vertical-incidence ionograms recorded at Tamanrasset (See figure 32.), that the ionosphere just south of Tripoli is dense enough during these times to reflect 20 Mc/s radio waves back toward the ground near the midpoint of the path. For radio waves thus reflected at the ground and subsequently scattered by spread-F irregularities at the same height as the initial ionospheric reflection, the positions where phase coherence may be attained become those of figure 32. These contours, being inclined to the path, allow the observation of a patch of irregularities as it approaches the path, and thus are consistent with the presence of sloping striations in the doppler-shift records.

Since this second interpretation requires an exceptionally strong ionosphere at $30-40^{\circ}$ magnetic dip (the observed "subequatorial anomaly"), it accounts for the disappearance of the doppler-shift signals at 0200-0300 LT, just when the concentration of ionization there is observed to dissipate suddenly.

The interpretation that the doppler-shift signals arrive by two-hop transmission, and thus that the scattering occurs at roughly one-quarter the total path length from the Accra terminal, leads to an

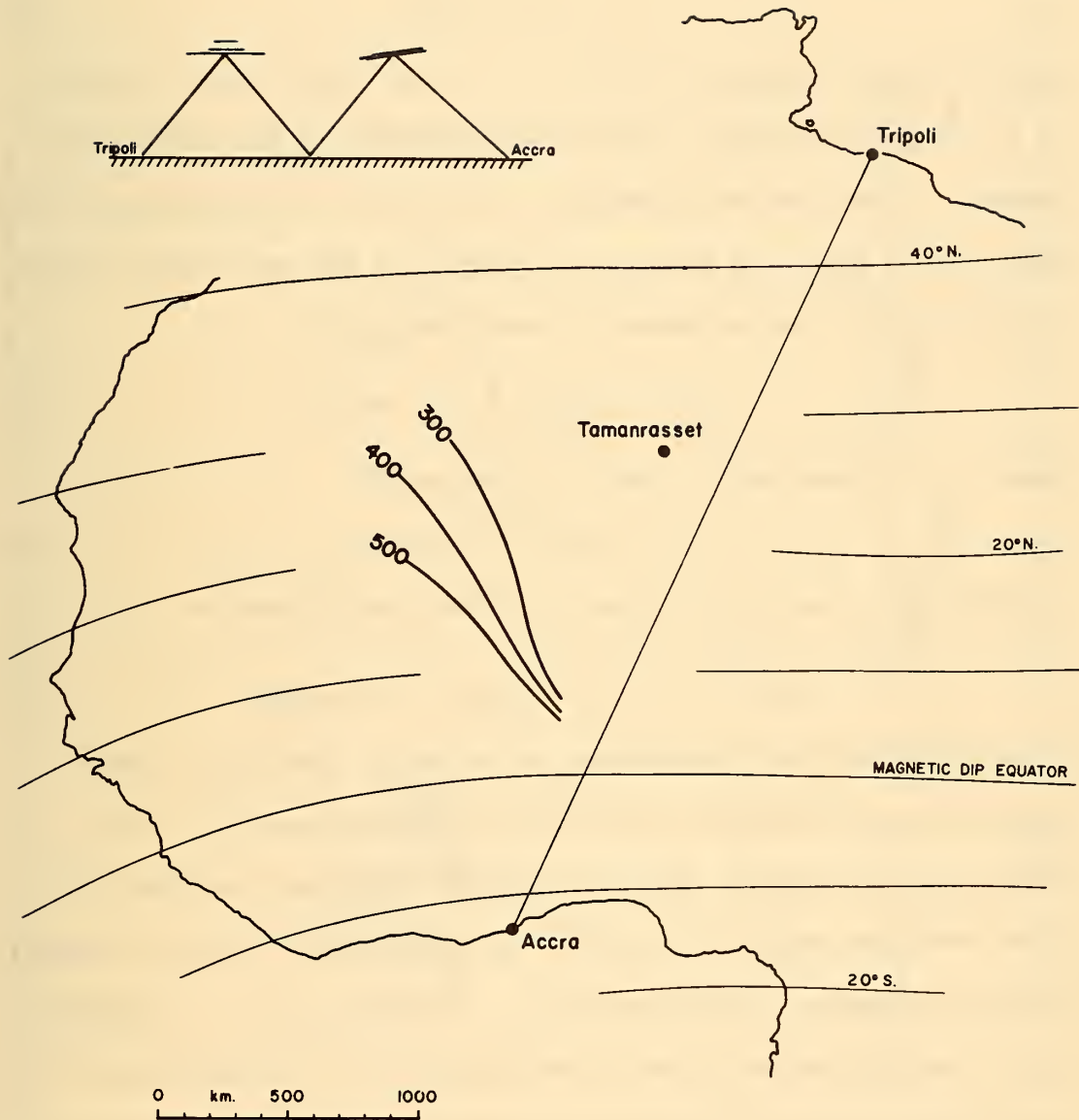


Figure 32. The height at which spread F irregularities would produce phase-coherent echoes on a two-hop model. The ionospheric reflection is assumed to occur at the same height as the scattering.

estimate of the spread-F velocities from the sloping striations. The doppler shift is

$$D = (f/c) \, dP/dt, \quad (6)$$

where f is the frequency (20 Mc/s), c is the speed of radio waves (3×10^8 m/s), and dP/dt is the time derivative of the total path length. If the scattering region is a distance x perpendicular to the great-circle path from a point one-quarter of the way between the two terminals (which are separated by the distance P_0),

$$dP/dt = (32/3) (x/P_0) \, dx/dt, \quad (7)$$

where x is assumed small. Hence, approximately,

$$D = 2 \times 10^{-7} (x \, dx/dt), \quad (8)$$

in MKS units. The slope of the striations should then be

$$dD/dt = 2 \times 10^{-7} (dx/dt)^2 \text{ cycles/sec}^2. \quad (9)$$

A number of velocities determined according to equation (9) were extracted from the month's data and plotted in figure 33. For comparison, the results from the spread-F simulation described above have been added to the figure as open circles (sunspot minimum) and open triangles (sunspot maximum). Considering that the doppler-shift observations were made as the sunspot cycle is approaching its next minimum, there is reasonable agreement between the two sets of results.

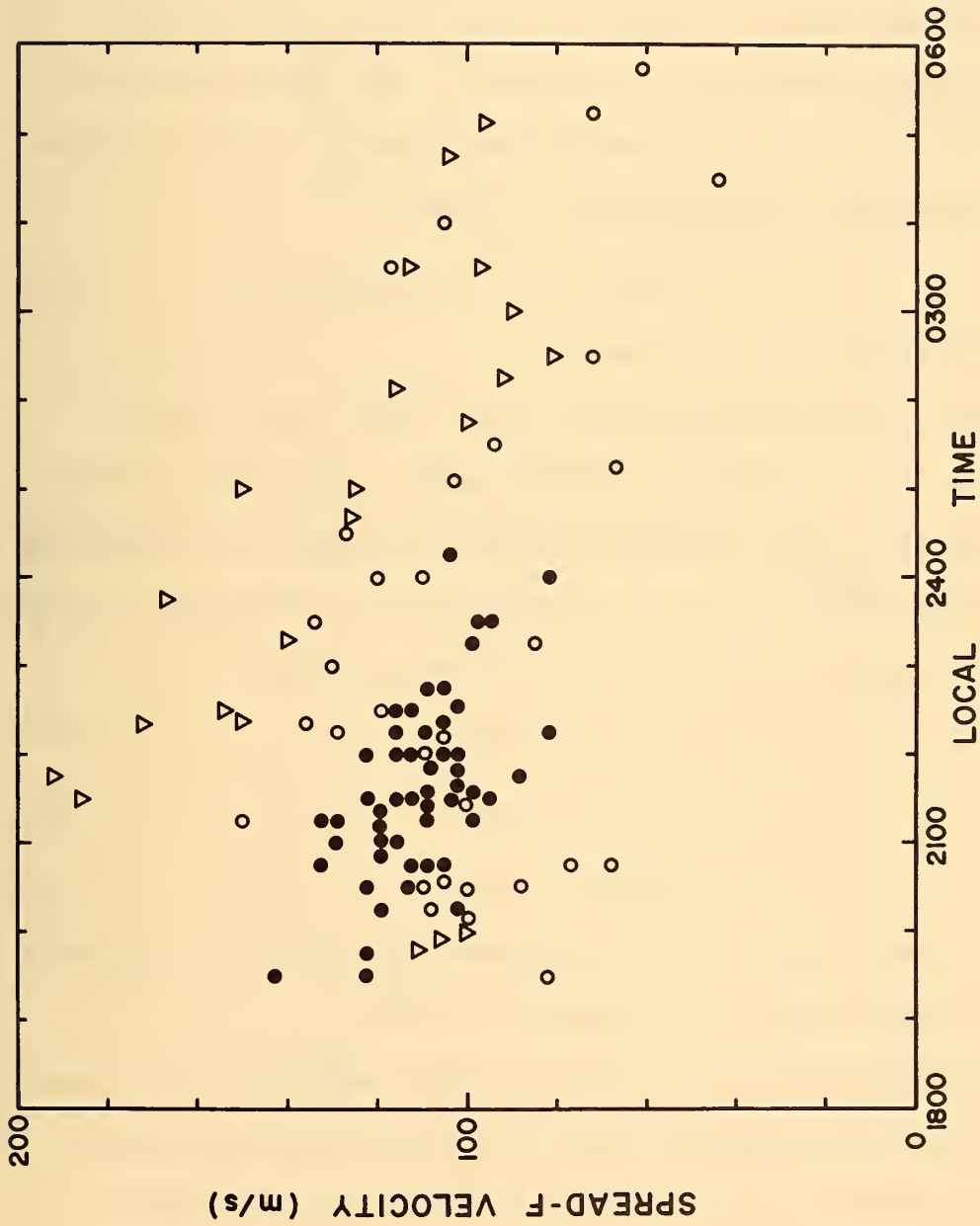


Figure 33. Spread-F velocities determined from the Tripoli-Accra doppler shifts (solid circles) compared with those determined by spread-F simulation during sunspot minimum (open circles) and sunspot maximum (open triangles).

Appendix C

CONDITIONS FOR PHASE COHERENCE ALONG THIN, MAGNETIC-
FIELD-ALIGNED IRREGULARITIES NEAR THE MAGNETIC EQUATOR

Figure 34 shows the cross-section of the earth (with radius a) and straight ray paths (of lengths r_1, r_2) between the terminals and a scattering irregularity (at height h). The great-circle arcs indicated (of lengths s_1, s_2) subtend the angles s_1/a and s_2/a at the center of the earth. From the law of cosines,

$$r^2 = h^2 + 2a(a + h)(1 - \cos s/a), \quad (10)$$

with the subscripts 1, 2 on r and s .

Figure 35 shows both ray paths in plan view. The two great-circle arcs from the terminals make the angles p and q with the horizontal component of the geomagnetic field (the vector B). Considering the variations of s_1, s_2 , and h as the position of scattering is varied along the geomagnetic field leads to the identifications

$$ds_1/dl = \cos p, \quad (11)$$

$$ds_2/dl = \cos q, \quad (12)$$

$$dh/dl = -\tan I; \quad (13)$$

where dl is the increment of the horizontal position of the scattering and I is the dip angle of the geomagnetic field.

The condition for phase coherence along a magnetic-field-aligned irregularity is that the variation of the total phase-path length is zero for variations of the scattering position along the magnetic field. With the assumption that the ionosphere has little effect, the phase path is approximately the geometric path of figures 34 and 35, and its length is approximately $(r_1 + r_2)$.

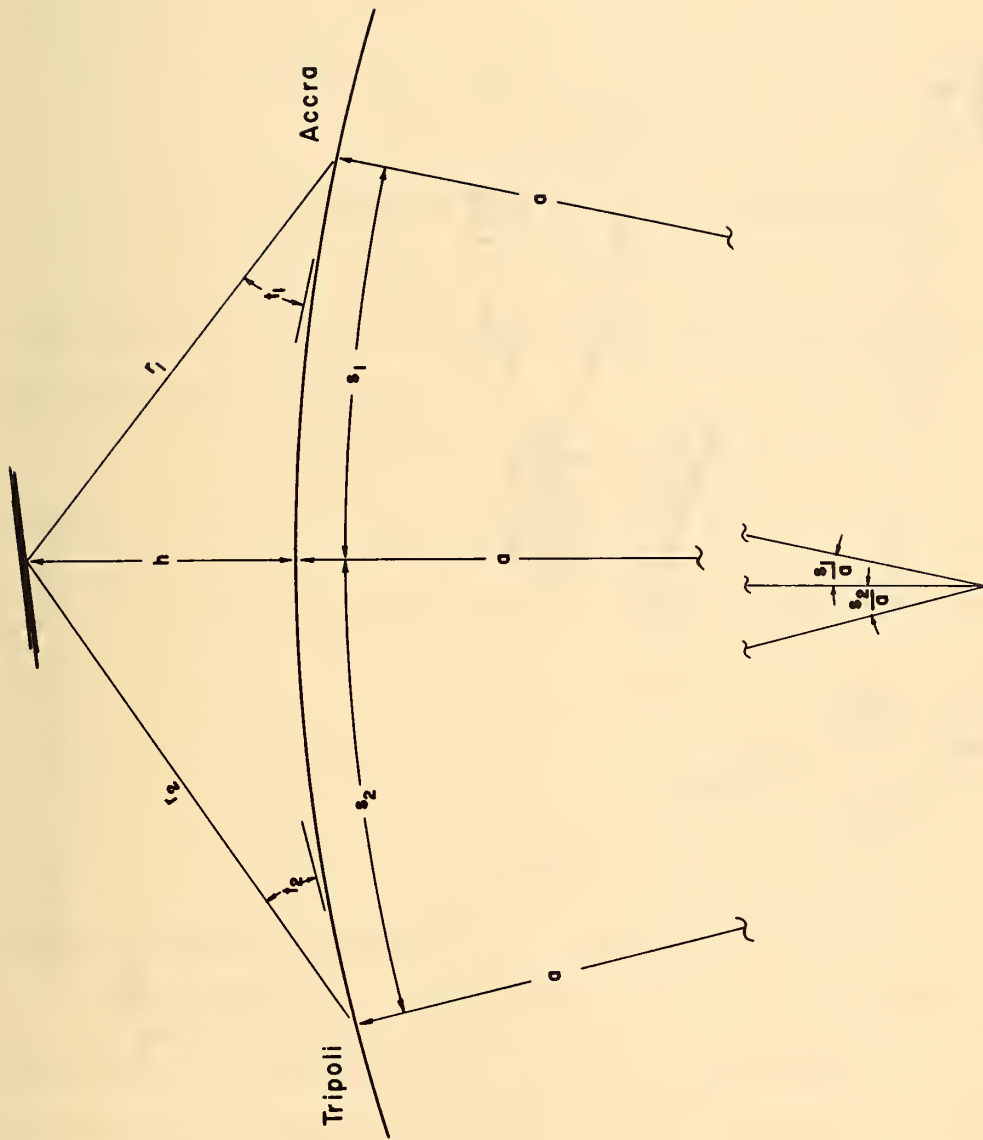


Figure 34. Ray-path geometry in the vertical plane.

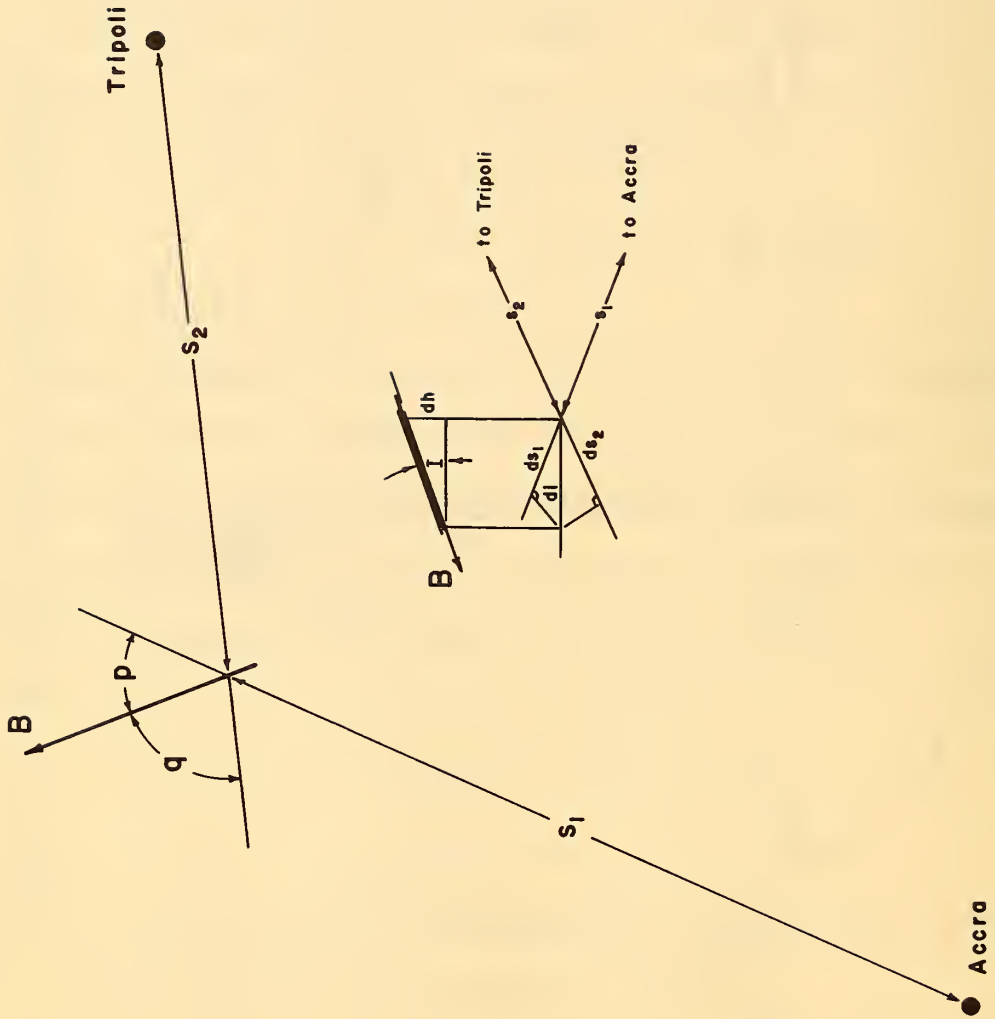


Figure 35. Ray-path geometry in plan view.

Thus for phase coherence:

$$dr_1/dl + dr_2/dl = 0. \quad (14)$$

Differentiating equation (10) and substituting from equations (11), (12), and (13) gives

$$\begin{aligned} r_1(dr_1/dl) &= -\tan I (h + a(1 - \cos s_1/a)) \\ &+ (a + h) \sin s_1/a \cos p, \end{aligned} \quad (15)$$

$$\begin{aligned} r_2(dr_2/dl) &= -\tan I (h + a(1 - \cos s_2/a)) \\ &+ (a + h) \sin s_2/a \cos q. \end{aligned} \quad (16)$$

Substituting for the $(1 - \cos s/a)$ factors from equation (10) and applying the law of sines,

$$(a + h) \sin s/a = r \cos t, \quad (17)$$

gives

$$\begin{aligned} dr_1/dl &= -\tan I (h/r_1 - (h^2 - r_1^2)/2r_1(a + h)) \\ &+ \cos t_1 \cos p, \end{aligned} \quad (18)$$

$$\begin{aligned} dr_2/dl &= -\tan I (h/r_2 - (h^2 - r_2^2)/2r_2(a + h)) \\ &+ \cos t_2 \cos q; \end{aligned} \quad (19)$$

where the ray take-off angle (t) is measured to the horizon.

If the height is a small fraction of the earth's radius, h may be neglected in comparison with a . With this approximation, the substitution of equations (18) and (19) into equation (14) gives the condition for phase coherence:

$$\begin{aligned} &(\cos t_1 \cos p + \cos t_2 \cos q) \cot I \\ &= h \left(\frac{1}{r_1} + \frac{1}{r_2} \right) + \frac{r_1 + r_2}{2a} \end{aligned} \quad (20)$$

The further approximations that the take-off angles are small and that the path lengths (r_1, r_2) are approximately equal to their great-circle arc lengths (s_1, s_2) simplifies the calculation of figures 31 and 32 by providing the formula

$$h = \left(\frac{s_1 s_2}{s_1 + s_2} \right) (\cos p + \cos q) \cot I - \frac{s_1 s_2}{2a}. \quad (21)$$

Figure 31 is obtained by using the distances to the terminals for s_1 and s_2 ; figure 32 by using the distance to Accra for s_1 and one-third the distance to Tripoli for s_2 .

Part IV

THEORIES OF SPREAD-F IRREGULARITIES

Current theories. A number of theories have been proposed to account for the irregularities causing equatorial spread F, although only two have had any measure of acceptance. These two, Martyn's (1959) electrostatic instability and Dagg's (1957d) coupling to turbulent E-region structure, will be treated later. The others will be briefly mentioned now.

Dessler (1958) suggested that hydromagnetic waves excited by the solar "wind" of particles would concentrate at the level where their velocity is greatest and produce a stratum of irregularities. Later calculations (Francis, Green, and Dessler, 1959) indicated that this height was 2000 to 4000 km, much too high for agreement with observed spread F.

Dagg (1957c) and Glover (1960) have surveyed the remaining theories: Irregular accretion of interstellar matter (Ryle and Hewish, 1950) would be inconsistent with the observed sunspot-cycle effects and with the occurrence of spread F in rather well-defined patches. An influx of charged solar particles (Shimazaki, 1959a, 1960a) would be deflected away from the equator to cause spread F only at high latitudes. Ryle's suggestion of charged-particle streaming forced by solar radiation pressure (Ratcliffe, 1956) predicts spread F just in the sunrise and sunset regions and contradicts the observation that the onset of spread F is delayed an hour or so after sunset.

Turbulence in the F region has not been considered among the theories, since it is thought to be quite weak at these heights. There is considerable evidence that the atmosphere above 120 km is not mixed by turbulence, but rests in diffusive equilibrium with each constituent distributed according to its own mass (Nicolet, 1960).

Electrostatic coupling to the E region. Dagg (1957d) suggested that irregular structure would be coupled strongly along the earth's magnetic field by the great anisotropy of the conductivity in the ionosphere. The high conductivity along the magnetic field lines (compared to that across) tends to make them equipotential lines so that they can transmit transverse electrostatic fields. Presumably such electrostatic fields can control the distribution of ionization.

An estimate of the strength of the coupling to be expected results from the following simple analogy: Two adjacent field lines play the role of a lossy transmission line on which the attenuation follows the law

$$d(\ln E)/ds = (R G)^{\frac{1}{2}} \quad (22)$$

where E is the electric field between the lines, R and G are the line resistance and the shunt conductance per unit length along the transmission line, and s is the distance along the lines (from transmission-line theory of electrical engineering). With the analogy, G corresponds to the transverse conductivity σ_t , and R corresponds to the 'wire area' L^2 divided by the longitudinal conductivity σ_o . Here L represents the transverse scale size to be transmitted. The expected attenuation is then

$$d(\ln E)/ds = (\sigma_t/\sigma_o)^{\frac{1}{2}} (1/L). \quad (23)$$

Finally, considering the electrostatic coupling to an e-fold drop in E , the minimum scale size which can be transmitted over the distance s is

$$L_{\min} = (\sigma_t/\sigma_o)^{\frac{1}{2}} s. \quad (24)$$

Figure 36 shows the height variation of L_{\min}/s for two choices of the transverse conductivity (Chapman, 1956): Curve A for the Pederson conductivity (Hall currents allowed) and Curve B for the Cowling conductivity (Hall currents prohibited). The former applies at high latitudes and to vertical electric fields at the equator. The latter applies to horizontal electric fields at the equator, since the horizontal stratification of the ionosphere prohibits Hall currents in this case. The figure indicates that the coupling from 100 km (the height of the \underline{E} region) should be some hundred-times stronger for vertical equatorial structure than for horizontal equatorial structure. Furthermore, since the \underline{E} region is some 1000 km distant along the earth's magnetic field, structure no smaller than 100 m in cross section should be expected in the equatorial \underline{F} layer.

The calculations of Spreiter and Briggs (1961), involving detailed solutions for the potential distribution having Fourier wavelength L , agree in substance with these results. Their limiting scale size in the transverse direction is somewhat larger, the order of 5 km.

The mechanism proposed by Dagg must be discarded as the mechanism creating equatorial spread- \underline{F} irregularities. On the basis of the above estimates, it is inconsistent with the observation of spread- \underline{F}

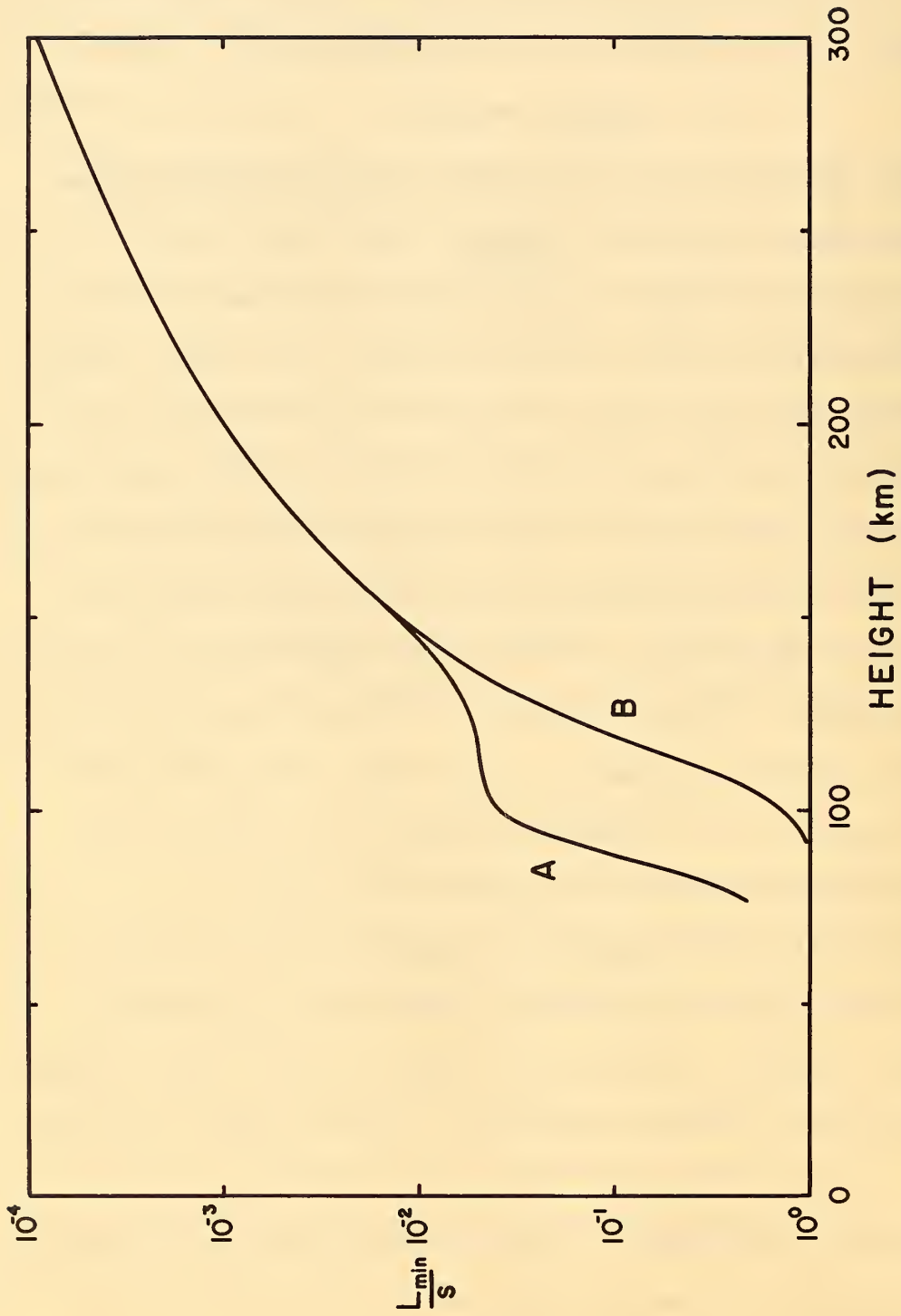


Figure 36. The minimum scale size (L_{\min}) which can be electrostatically coupled a given distance (s) along the geomagnetic field. Curves A and B correspond to coupling with and without the flow of Hall currents.

irregularities as thin as 6 m in cross-section (Cohen and Bowles, 1961)

Amplification of drifting irregularities. This section provides a basis for the discussions below which treat the instability of the ionosphere resulting from (1) electrostatic fields, (2) thermal contraction of the neutral atmosphere, (3) gravity waves, and (4) geomagnetic support of the ionosphere against gravity.

An irregularity in the ionization of the ionosphere may drift relative to the ambient ionization as a result of the above causes. If such a drift carries the irregularity to a region where its contrast with the ambient density is increased, it is, in effect, amplified. In other words, the relative strength of the irregularity

$$\epsilon = \Delta N/N \quad (25)$$

is increased in magnitude (N and $N + \Delta N$ are the ionization densities outside and inside the irregularity.) Where irregularities are amplified the ionosphere is unstable; where attenuated, stable.

An overdense irregularity is illustrated in figure 37 drifting through the distance dz and, as a result, increasing its strength from $\Delta N_1/N_1$ to $\Delta N_2/N_2$. It is thus amplified by the factor

$$\mu = (\Delta N_2/N_2) / (\Delta N_1/N_1). \quad (26)$$

With the assumption that dz is small, this may be written

$$\mu = (1 - A dz/\epsilon) / (1 + A dz), \quad (27)$$

where A is the logarithmic gradient of the ionization density in the direction of the drift:

$$A = (1/N) dN/dz. \quad (28)$$

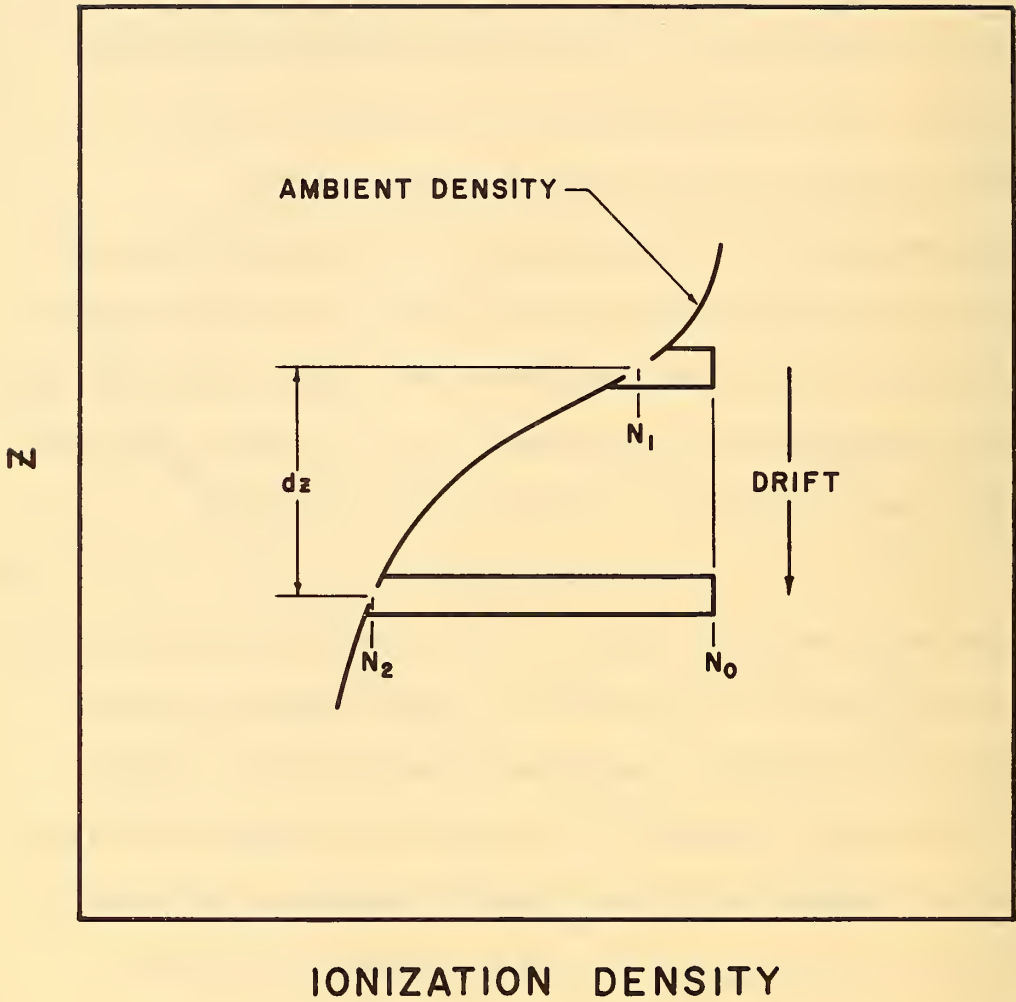


Figure 37. Amplification of an irregularity in ionization density as it drifts vertically.

Further, with $(A dz)$ much less than unity, the amplification is

$$\mu = 1 - A dz/\epsilon. \quad (29)$$

In the cases considered below, where $|\epsilon|$ is small, the drift velocity of the irregularity relative to the surrounding medium will be shown to be proportional to ϵ .

$$\mu = -\frac{1}{2} \epsilon U, \quad (30)$$

where U is a velocity related to the mechanism involved.

The irregularity covers the distance dz in the time $dt = dz/u$, during which it increases its strength by $d\epsilon$:

$$d\epsilon = (\mu - 1)\epsilon = -A u dt. \quad (31)$$

Substituting from equation (30) and integrating yields the overall amplification of the irregularity:

$$\epsilon/\epsilon_0 = \exp \left(\int_{t_1}^{t_2} \frac{1}{2} A U dt \right). \quad (32)$$

Hence the ionization profile is stable where $(A U)$ is negative and unstable where it is positive. Furthermore, the time constant of the instability growth or decay is

$$T = 1/\left(\frac{1}{2} A U\right).$$

Electrostatic drift. Martyn (1959) has proposed that the source of equatorial spread-F irregularities is an amplifying drift arising from an east-west electrostatic field in the F layer. This electric field causes both the ionosphere and its irregularities to drift vertically, but with slightly different speeds. The differential velocity between the two derived by Martyn is also derived in appendix D (equation (85)). For weak irregularities ($\epsilon \ll 2$) its vertical

component is

$$u_y = -\frac{1}{2}\epsilon U_0, \quad (33)$$

where U_0 is the upward electrostatic drift velocity of the F layer (equation (83)). From equation (32), the overall amplification of irregularities is thus

$$\epsilon/\epsilon_0 = \exp\left(\frac{1}{2} A U_0 t\right). \quad (34)$$

Under this mechanism, the F layer should be unstable below its peak when drifting upward and above its peak when drifting downward. Furthermore, irregularities should be formed more readily near the base of an F layer drifting upward, since the logarithmic gradient of ionization density (A) is greatest there. These predictions agree with the morphology of the spread F that forms just after sunset: The onset of spread F corresponding to irregularities near the base of the layer is immediately preceded by a rise of the F layer.

If the sudden rise in the F layer after sunset is entirely due to an electrostatic field, ($U t$) may be as large as 200 km. With an observed value of 0.1 km^{-1} for the logarithmic gradient (A) near the base of the nighttime F layer, the corresponding overall amplification may exceed 10^4 .

Unfortunately, this theory does not present an adequate source of the electrostatic field. To produce the desired effects, a field of $500 \mu\text{V/m}$ must exist shortly after sunset, abruptly reversing in sense when the F layer reaches its greatest height (at 2100-2200 LT). Martyn originally suggested that the electric field driving the daily Sq current system of the E region might be adequate. The

diurnal range in the strength of this electric field (determined from the strength of the Sq currents) is the order of $800 \mu\text{V}/\text{m}$ near the equator. However, the electric field attains its greatest magnitude near noon, and apparently dwindles to a weak field by sunset (Hirano and Maeda, 1955). In short: The diurnal variations of this Sq electric field are of the wrong phase. Two alternate sources for the required electrostatic field--a charge concentration at sunset and induction by the changing equatorial electrojet current--are of the wrong sense and of insufficient magnitude, respectively.

Thermal contraction of the neutral atmosphere. An alternative to Martyn's theory is proposed in this section. It is based on the cooling of the atmosphere after sunset.

Lowan (1955) assumed that the upper atmosphere cools after sunset principally by downward thermal conduction. His calculations indicate that the atmosphere above 200 km should remain nearly isothermal as it cools from 1250°K to 850°K during the two hours following sunset. Recent satellite measurements of the electron temperature (Serbu, Bourdeau, and Donley, 1961) bear out Lowan's predictions remarkably well. The nocturnal temperatures at F-region heights range from 1800°K at dusk to 1000°K at dawn, with most of the decrease occurring abruptly after sunset.

The neutral atmosphere should contract as it cools. Its downward motion gives rise to an instability in the ionosphere quite similar to that of electrostatic fields.

The analysis of the motion of ionization irregularities in appendix D tacitly assumes (through the simple definition of particle

mobilities) that the frame-of-reference is fixed to the neutral atmosphere. Hence, with this analysis, effects of the moving neutral atmosphere enter the picture as effects caused by the use of a moving frame-of-reference.

The motion of the frame-of-reference across the geomagnetic field produces, in that frame, an induced electric field given by

$$E = V \times B, \quad (35)$$

where V is the velocity of the frame-of-reference and B is the magnetic field. Exactly as indicated in the previous section, this electric field causes a differential drift and thus an instability in the ionization profile. In this case the proper value of U for equation (30) is approximately V , the velocity of the frame-of-reference, and the overall amplification of irregularities is

$$\epsilon/\epsilon_0 = \exp \left(\int \frac{1}{2} A V dt \right). \quad (36)$$

The vertical drift of the ionosphere as a whole is also approximately V (from equation (83) and the assumption of small collision frequencies) relative to the moving frame-of-reference. Upon transformation back to fixed coordinates, this drift overcomes the motion of the frame and the ionosphere is practically stationary (its motion being roughly $(x \times V)$, where x and X are the order of 10^{-2} - 10^4).

If the neutral atmosphere is in hydrostatic equilibrium throughout its contraction, its vertical velocity can be shown to be

$$V = (H + h)(1/T)dT/dt, \quad (37)$$

where H is the scale height of the neutral atmosphere (assumed constant

with height), h is the height above the level where the density is not changing (near 200 km in this case), T is the temperature, and t is the time. Its integral in time (for substitution in equation (36)) as the scale-height changes from H_1 to H_2 is

$$-\int_1^2 v dt = H_1 - H_2 + h \ln (H_1/H_2). \quad (38)$$

The amplification of irregularities thus increases exponentially with height. If $H_1 = 50$ km, $A = 0.1 \text{ km}^{-1}$ (appropriate for the base of the nighttime F layer), and the reference level for h is at 200 km, the results obtained by Serbu, et. al. (1961) give the following overall amplifications (from equations (36) and (38)):

Height:	300 km	400 km	500 km
ϵ/ϵ_0 :	58	10^3	2×10^4

The post-sunset rise of the F layer--now attributed mostly to recombination and lateral diffusion away from the equator (Norton and VanZandt, 1962)--contributes to the formation of equatorial spread F simply by bringing the F layer to greater heights where the irregularity amplification is greater.

Gravity waves. The instability mechanism described above is not limited to thermal contraction. It would arise with any appreciable motion of the neutral atmosphere across the contours of equal ionization density.

For instance, such an instability could arise with gravity waves possessing vertical motions of sufficient amplitude. Such gravity waves, excited in the F region by the relatively sudden adjustment

of the neutral atmosphere after sunset, might well explain the spread-F motions described in part III. The calculations on internal gravity waves in the ionosphere by Hines (1953, 1959, 1960) indicate that the observed spread-F velocities should correspond to 100 km wavelengths in the east-west direction. It is curious that striations of nearly this spacing often occur in configurations of equatorial 'scatter' spread F (e.g. figures 7a, 8a, and 24c).

Gravitational instability. A final source of instability arises from geomagnetic support of the F layer. A plasma supported against gravity by a horizontal magnetic field is analogous to a dense fluid supported by a weightless fluid--it is unstable (Chandrasekhar, 1960).

The downward velocity of ionization irregularities under gravity is calculated in appendix D (equation (91)), and is approximately

$$u = -\frac{1}{2} \epsilon g/v_i, \quad (39)$$

where g is the acceleration of gravity and v_i is the ionic collision frequency. Thus, in equation (30),

$$U = g/v_i. \quad (40)$$

With the logarithmic gradient used earlier, $A = 0.1 \text{ km}^{-1}$, the time constant of this instability at 300 km is the order of 1/2 hour by day and 2 minutes by night (using Chapman's (1956) collision frequencies for hot (1500°K) and cold 850°K) models of the thermosphere). These time constants should decrease with height along with the density of the neutral atmosphere--exponentially with a scale height the order of 50 km.

This instability gives rise to the "convective diffusion" described by Johnson and Hulburt (1950) and Dungey (1956). This

hypothesis allows the downward transport of ionization in the equatorial ionosphere to be carried by these gravitational irregularities. Presumably the irregularities would coalesce at a lower height where the time constant of the instability is greater. This mechanism is consistent with the observation that the equatorial F layer often starts to fall when spread F first forms (figure 5). Observations where the F layer falls without the occurrence of spread F might be disclaimed with the apology that the observing equipment was insensitive to either the scale size or the strength of the irregularities present. (Improved ionosondes have done much toward increasing the occurrence of spread F.)

Conclusions. The minimum scale size which could be electrostatically transmitted from the E region is too large to account for observed equatorial spread-F irregularities.

Martyn's drift theory would account for the equatorial spread F observed shortly after sunset if the existence of the required electrostatic field could be justified.

Thermal contraction of the neutral atmosphere, based on the observed atmospheric cooling after sunset, provides an adequate degree of instability.

Additional sources of instability are possible, resulting from (1) geomagnetic support of the F layer or from (2) vertical motions of atmospheric gravity waves excited by the thermal adjustment after sunset.

More than one type of instability may combine to provide the nocturnal display of equatorial spread F. The sudden onset of

spread F might be attributed to thermal contraction; its maintenance as the F layer falls to gravitational instability; and its occurrence late in the night to wave motion.

Appendix D

THE MOTION OF A CYLINDRICAL IRREGULARITY IN IONIZATION

Introduction. The mobility of a particle is defined as the ratio of its velocity to the force causing the motion. In the presence of a magnetic field, the mobility of a charged particle may depend strongly upon direction. This being the case, the mobility is treated as a tensor with three independent components. In the geometry of figure 38, the magnetic field is parallel to the z-axis and the assumed force lies in the xz-plane. Then the longitudinal mobility is

$$L' = \bar{v}_z / F_z, \quad (41)$$

the transverse mobility is

$$T' = \bar{v}_x / F_x, \quad (42)$$

and the Hall mobility is

$$H' = \bar{v}_y / F_x; \quad (43)$$

where F is the force and \bar{v} is an average of the particle velocity.

A simple calculation of these mobilities (after Ratcliffe, 1959) is presented below.

Between collisions with other particles, the charged particle is assumed to follow the well-known cycloidal path (superimposed on its random thermal motion):

$$v_x = (F_x / eB) \sin wt, \quad (44)$$

$$v_y = -(F_x / eB)(1 - \cos wt), \quad (45)$$

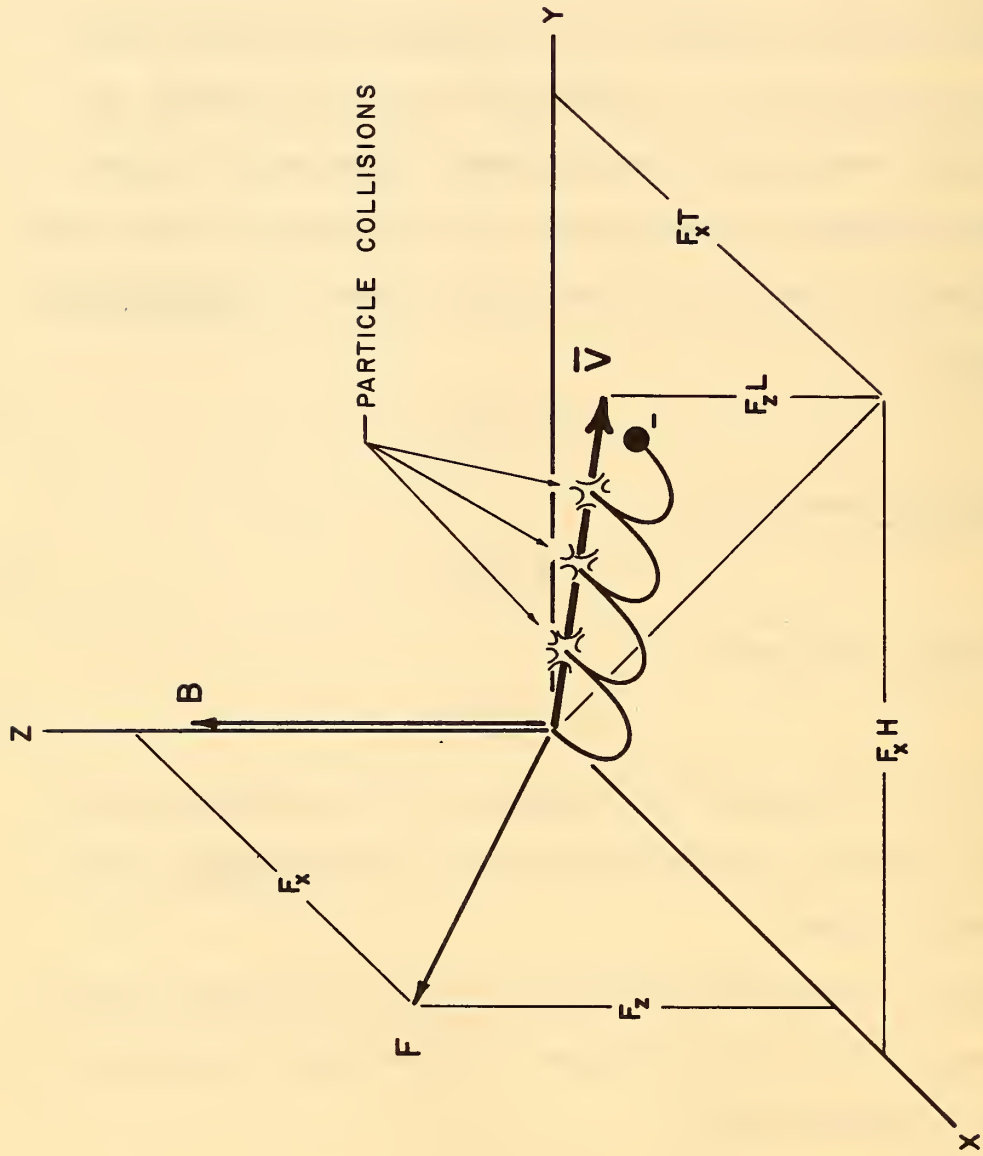


Figure 38. The motion of a (negatively) charged particle in a magnetic field.

$$V_z = (F_z/m) t; \quad (46)$$

where e is the charge of the particle (sign included), B is the magnetic field strength, m is the particle mass, w is the angular gyrofrequency ($= eB/m$), and t is the time. Since a collision will randomize this orderly motion, the particle is, in effect, stopped by each collision; whereupon it restarts the cycloidal motion again. The net motion of the particle due to the applied force is thus the average of its instantaneous motion, weighted by the time between collisions. The probability of collision is taken to be

$$\exp(-vt),$$

where v is the collision frequency of the particle. With this, equations (44), (45), and (46) yield the following average velocity:

$$\bar{V}_x = (v/m(v^2 + w^2))F_x, \quad (47)$$

$$\bar{V}_y = - (w/m(v^2 + w^2))F_x, \quad (48)$$

$$\bar{V}_z = (1/mv) F_z. \quad (49)$$

From this, the mobilities are

$$L' = 1/mv, \quad (50)$$

$$T' = v/m(v^2 + w^2), \quad (51)$$

$$H' = -w/m(v^2 + w^2). \quad (52)$$

Where the force may not lie in the xz -plane, the average particle motion is

$$\bar{V}_x = T'F_x - H'F_y, \quad (53)$$

$$\bar{V}_y = H'F_x + T'F_y, \quad (54)$$

$$\bar{V}_z = L'F_z. \quad (55)$$

In the equations which follow, it will be convenient to use the symbols h and t for the Hall and transverse mobilities of the electrons, and H and T for those of the ions. Further, with

$$x = |v_e/w_e|, \quad X = v_i/w_i, \quad H_0 = 1/eB;$$

these mobilities are

$$\begin{aligned} h &= H_0/(1 + x^2), & t &= x H_0/(1 + x^2), \\ H &= -H_0/(1 + X^2), & T &= X H_0/(1 + X^2). \end{aligned} \tag{56}$$

Derivation. The method employed below to arrive at the drift of an irregularity in ionization is that started by Martyn (1953) and finished by Clemmow, Johnson, and Weekes (1955). In addition to the electrostatic drift treated by them, gravitational drift will be considered.

The motions of ions and electrons are examined relative to an irregularity in the form of an infinitely-long circular cylinder with its axis parallel to the earth's magnetic field. The motions arise from (1) an applied force field, and from (2) an electrostatic field of induced charges residing on the surface of the cylinder. In applying the condition that the irregularity should be stable, it is found to drift through the surrounding medium.

The applied force, assumed to be perpendicular to the irregularity, defines a reference direction for the cylindrical coordinate system employed, the $r\theta$ -plane of which is shown in figure 39. Its components are thus

$$F_r = F \cos \theta, \tag{57}$$

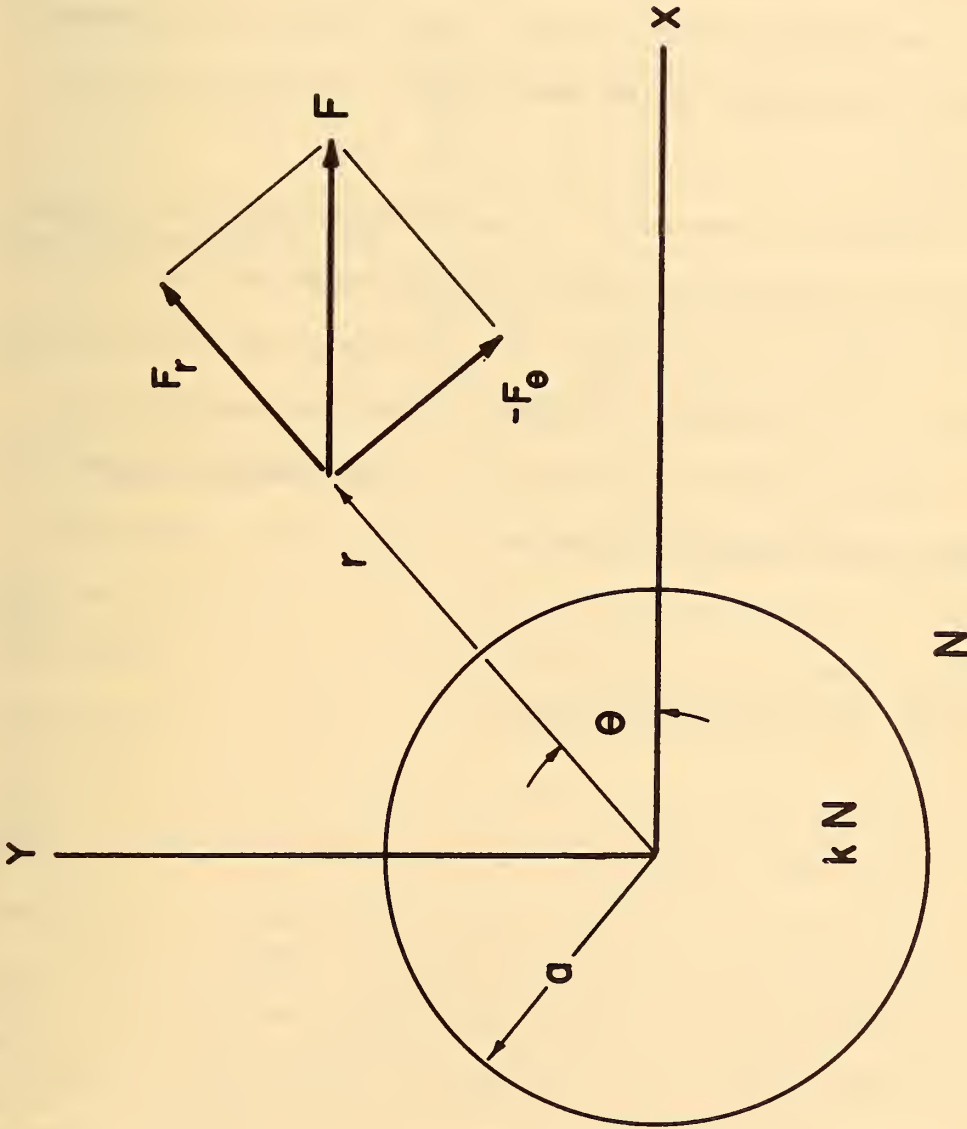


Figure 39. The cross-section of an ionization-density irregularity and the polar coordinate system employed in the text. (The magnetic field is directed out of the page.)

$$F_{\theta} = - F \sin \theta. \quad (58)$$

Under applied forces, the ions and electrons in the ionized medium will tend to move differently, according to their individual mobilities. In a non-uniform medium, this leads to charge separation, and thus to an induced electric field. Hence particle motions are dictated by a combination of two force fields; one applied and the other induced.

The ionization is assumed to be uniform both inside and outside the cylindrical irregularity. Hence induced charges should develop only on the surface of the cylinder, as a result of the discontinuity in the density of ionization. Elsewhere, electrical neutrality is assumed. The electrostatic potential (P) of the induced charges should thus satisfy Laplace's equation

$$\nabla^2 P = 0. \quad (59)$$

This equation is easily solved, giving

$$P = \sum_n (C_n r^n + D_n r^{-n}) \cos (n \theta + p_n) + C_0 \ln r + D_0, \quad (60)$$

where C_n , D_n , and p_n are integration constants. The part of this solution corresponding to a uniform field within the cylinder ($n = 1$) seems to be appropriate, and the remainder is arbitrarily discarded. Further requiring that the potential be finite and continuous leads to the following solutions inside (P) and outside (P') the cylinder:

$$P = Q r \cos (\theta + p), \quad (61)$$

$$P' = Q (a^2/r) \cos (\theta + p); \quad (62)$$

where a is the radius of the cylinder and Q, p are the two remaining integration constants. The forces on a particle with the charge e , given by

$$- e \nabla P \text{ or } - e \nabla P',$$

are thus

$$F_r^S = - Q e \cos (\theta + p), \quad (63)$$

$$F_\theta^S = Q e \sin (\theta + p) \quad (64)$$

inside the cylinder, and

$$F_r^{S'} = Q e (a/r)^2 \cos (\theta + p), \quad (65)$$

$$F_\theta^{S'} = Q e (a/r)^2 \sin (\theta + p) \quad (66)$$

outside the cylinder.

The total force acting on a charged particle (either ion or electron) is thus $(F + F^S)$ inside the cylinder and $(F + F^{S'})$ outside the cylinder. The two unknown constants (Q and p) remaining in these expressions are determined from the conditions that the particle fluxes must each be continuous across the boundary of the cylinder.

In this process it is necessary to superimpose a velocity U , representing the drift of the irregularity, upon the particle velocities. Where V and V' are the particle velocities on the two sides of the boundary and k is the ratio of ionization densities across the boundary, this continuity condition is

$$k (V_r + U_r) = (V'_r + U_r). \quad (67)$$

Calculating the particle velocities according to equation (53) and substituting them into equation (67) gives

$$\begin{aligned}
 & (FT' + (QeT'/d) \cos p - QeH' \sin p + U_x) \cos \theta \\
 & + (FH' - (QeT'/d) \sin p - QeH' \cos p + U_y) \sin \theta = 0 \quad (68)
 \end{aligned}$$

where U_x and U_y are the cartesian components of U , and

$$d = (1 - k)/(1 + k), \quad (69)$$

In order to satisfy equation (69) all around the boundary of the cylinder, the coefficients of $(\cos \theta)$ and $(\sin \theta)$ must separately vanish. Thus there are two equations for electrons and two for ions; a total of four equations to be solved for Q , p , U_x , and U_y . Using the abbreviations

$$C = Q |e| \cos p, \quad S = Q |e| \sin p, \quad (70)$$

and the notation that F and f are the applied forces on the ions and electrons, respectively; these four equations are

$$FT = -T/d C + H S - U_x, \quad (71)$$

$$ft = t/d C - h S - U_x, \quad (72)$$

$$FH = H C + T/d S - U_y, \quad (73)$$

$$fh = -h C - t/d S - U_y. \quad (74)$$

The components of the drift velocity may then be found in terms of ratios of determinants:

$$U_x = [x]/[D], \quad U_y = [y]/[D], \quad (75)$$

$$\text{where} \quad [D] = (T + t)^2 + d^2 (H + h) \quad (76)$$

$$\begin{aligned}
 [x] = & -T t (T + t) (F + f) \\
 & - d (Th - tH) (FH - fh) \\
 & - d^2 (H + h) (FTh + ftH) \quad (77)
 \end{aligned}$$

$$\begin{aligned}
 [y] = & - (T + t) (FhT + fhT) \\
 & + d (Th - tH) (FT - ft) \\
 & + d^2 H h (H + h) (F + f)
 \end{aligned} \tag{78}$$

Electrostatic drift. If the applied forces are those of an electrostatic field E,

$$F = |e| E, \quad f = - |e| E. \tag{79}$$

This gives the result previously arrived at by Clemmow, Johnson, and Weekes (1955):

$$U_x = - \frac{(d + d^2)(Th - tH)(H + h)}{(T + t)^2 + d^2(H + h)^2} |e| E, \tag{80}$$

$$U_y = \frac{(1 + d)(Th - tH)(T + t)}{(T + t)^2 + d^2(H + h)^2} |e| E. \tag{81}$$

When d is zero, equations (80) and (81) give the electrostatic drift of the ambient medium:

$$U_{ox} = 0, \tag{82}$$

$$U_{oy} = (Th - tH) |e| E / (T + t) = (E/B) / (1 + xX). \tag{83}$$

If the irregularity is relatively weak (i.e. if d is small), the velocity of the cylindrical irregularity relative to the ambient medium is

$$u_x = - (d + d^2) \frac{H + h}{T + t} U_{oy} = \frac{2\epsilon}{(2 + \epsilon)^2} \frac{x - X}{1 + xX} U_{oy}. \tag{84}$$

$$u_y = d U_{oy} = - \frac{\epsilon}{2 + \epsilon} U_{oy}, \tag{85}$$

where ϵ is the fractional deviation of the ionization density ($\epsilon = k - 1$).

Gravitational drift. If the applied forces are those of a gravitational field g :

$$F = M g, \quad f = m g, \quad (86)$$

where M, m are the ionic, electronic masses, respectively.

Neglecting m compared to M gives the result:

$$U_x = - \frac{Tt(T+t) + dH(Th - tH) + d^2Th(H+h)}{(T+t)^2 + d^2(H+h)^2} M g, \quad (87)$$

$$U_y = - \frac{Ht(T+t) - dT(Th - tH) + d^2Hh(H+h)}{(T+t)^2 + d^2(H+h)^2} M g. \quad (88)$$

When d is zero, equations (87) and (88) give the gravitational drift of the ambient medium:

$$U_{ox} = - \frac{T t M g}{T+t} = - \frac{xX}{1+xX} \frac{g}{v_i + (m/M)v_e} \quad (89)$$

$$U_{oy} = - \frac{H t M g}{T+t} = - \frac{X}{1+xX} \frac{g}{v_i + (m/M)v_e} \quad (90)$$

If the irregularity is relatively weak (i.e. if d is small), the velocity of the cylindrical irregularity relative to the ambient medium is approximately

$$\begin{aligned} u_x &= - H (Th - tH) d M g / (T+t)^2 \\ &= d (1+x^2) (U_{ox}/xX) \\ &= - (\epsilon/(2+\epsilon)) (g/v_i), \end{aligned} \quad (91)$$

$$\begin{aligned} u_y &= T (Th - tH) d M g / (T+t)^2 \\ &= d (1+x^2) U_{oy} \\ &= - (\epsilon/(2+\epsilon)) (g/w_i), \end{aligned} \quad (92)$$

where ϵ is the fractional deviation of the ionization density ($\epsilon = k - 1$).

Appendix E.

GEOGRAPHIC LOCATIONS MENTIONED IN THE TEXT

Name	geog. coord.	mag. dip	Remarks
Accra, Ghana	5°45'N, 0° 8'W	13°S	D
Antofagasta, Chile	23°44'S, 70°15'W	17°S	T
Chiclayo, Peru	6°47'S, 79°47'W	9°N	I
Chimbote, Peru	9° 4'S, 78°34'W	5°N	I
Dakar, Dr. W. Africa	14°36'N, 17°24'W	17°N	I
Guayaquil, Ecuador	2°36'S, 80°24'W	17°N	T
Huancayo, Peru	12° 3'S, 75°20'W	2°N	I
Ibadan, Nigeria	7°26'N, 3°53'E	8°S	I
La Paz, Bolivia	16°30'S, 68°10'W	5°S	I
Maui, Hawaii, USA	20°50'N, 156°30'W	39°N	I
Natal, Brazil	5°18'S, 35° 6'W	2°N	I
Rarotonga Island	21°15'S, 159°45'W	39°S	I
Talara, Peru	4°34'S, 81°15'W	13°N	I
Tamanrasset, Algeria	22°50'N, 5°31'E	28°N	I
Tripoli, Libya	32°55'N, 13°25'E	46°N	D
Washington, D. C., USA	38°55'N, 77° 0'W	71°N	I

D: Doppler Shift Station

I: Ionosonde

T: Transequatorial Scatter Station

REFERENCES

- Booker, H. G., Turbulence in the ionosphere with applications to meteor-trails, radio-star scintillation, auroral radio echoes, and other phenomena, J. Geophys. Research, 61, 673-705, 1956.
- Booker, H. G., and H. W. Wells, Scattering of radio waves by the F region of the ionosphere, Terr. Mag., 43, 249-256, 1938.
- Bowles, K. L., and R. Cohen, NBS equatorial region VHF scatter research program for the IGY, QST, 41, 11-15, 1957.
- Bowles, K. L., and R. Cohen, Studies of scattering phenomena in the equatorial ionosphere based upon VHF transmissions across the magnetic equator, Some Ionospheric Results Obtained during the International Geophysical Year, W. J. G. Beynon, ed., 192-193, 1960.
- Bowles, K. L., and R. Cohen, A study of radio wave scattering from sporadic E near the magnetic equator, Ionospheric Sporadic E, Pergamon Press, 1962a.
- Bowles, K. L., and R. Cohen, On the nature of 'equatorial sporadic E' (in preparation, 1962b).
- Bowles, K. L., R. Cohen, G. R. Ochs, and B. B. Balsley, Radio echoes from field-aligned ionization above the magnetic equator and their resemblance to auroral echoes, J. Geophys. Research, 65, 1853-1855, 1960.
- Breit, G., and M. A. Tuve, A test of the existence of the conducting layer, Phys. Rev., 28, 554-575, 1926.
- Brenan, P. M., The correlation of radio source scintillation in the southern and northern hemispheres, J. Atmospheric and Terrest. Phys., 19, 287-289, 1960.
- Briggs, B. H., The diurnal and seasonal variations of spread F ionospheric echoes and the scintillations of a radio star, J. Atmospheric and Terrest. Phys., 12, 89-99, 1958.
- Calvert, W., and R. Cohen, The interpretation and synthesis of certain spread F configurations appearing on equatorial ionograms, J. Geophys. Research, 66, 3125-3140, 1961.
- Chandrasekhar, S., Plasma Physics, 1960.

- Chapman, S., The electrical conductivity of the ionosphere; A Review, Nuovo Cimento Supplements, 4, 1385-1412, 1956.
- Clemmow, P. C., M. A. Johnson, and K. Weeks, A note on the motion of a cylindrical irregularity in an ionized medium, The Physics of the Ionosphere, The Physical Society, 136-139, 1955.
- Cohen, R., and K. L. Bowles, On the nature of equatorial spread F, J. Geophys. Research, 66, 1081-1106, 1961.
- Cohen, R., K. L. Bowles, and W. Calvert, On the nature of 'equatorial slant sporadic E', J. Geophys. Research, 67, 965-972, 1962.
- Dagg, M., The correlation of radio-star-scintillation phenomena with geomagnetic disturbances and the mechanism of motion of ionospheric irregularities in the F region, J. Atmospheric and Terrest. Phys., 10, 194-203, 1957a.
- Dagg, M., Diurnal variations of radio-star scintillations, spread F, and geomagnetic activity, J. Atmospheric and Terrest. Phys., 10, 204-214, 1957b.
- Dagg, M., The origin of the ionospheric irregularities responsible for radio-star scintillations and spread F--I. Review of existing theories, J. Atmospheric and Terrest. Phys., 11, 133-138, 1957c.
- Dagg, M., The origin of the ionospheric irregularities responsible for radio-star scintillations and spread F--II. Turbulent motion in the dynamo region, J. Atmospheric and Terrest. Phys., 11, 139-150, 1957d.
- Davies, K., J. M. Watts, and D. H. Zacharisen, A study of F_2 -layer effects as observed with a doppler technique, J. Geophys. Research, 67, 601-610, 1962.
- Dessler, A. J., Large-amplitude hydromagnetic waves above the ionosphere, J. Geophys. Research, 63, 507-511, 1958.
- Dieminger, W., The scattering of radio waves, Proc. Phys. Soc., 64B, 142-158, 1951.
- Dungey, J. W., Convective diffusion in the equatorial F region, J. Atmospheric and Terrest. Phys., 9, 304-310, 1956.
- Eckersley, T. L., Irregular ionic clouds in the E layer of the ionosphere, Nature, 140, 846-847, 1937.
- Eckersley, T. L., Analysis of the effect of scattering in radio transmission, J. Inst. E. E., 86, 548-563, 1940.

- Egan, R. D., Anisotropic field-aligned ionization irregularities in the ionosphere near the magnetic equator, J. Geophys. Research, 65, 2343-2358, 1960.
- Francis, W. E., M. I. Green, and A. J. Dessler, Hydromagnetic propagation of sudden commencements of magnetic storms, J. Geophys. Research, 64, 1643-1645, 1959.
- Glover, F. N., A survey of spread F, National Bureau of Standards Tech. No. 82, 67 pp., 1960.
- Hines, C. O., Wave hypothesis of moving irregularities in the ionosphere, Nature, 171, 980, 1953.
- Hines, C. O., An interpretation of certain ionospheric motions in terms of atmospheric waves, J. Geophys. Research, 64, 2210-2211, 1959.
- Hines, C. O., Internal atmospheric gravity waves at ionospheric heights, Can. J. Phys., 38, 1441-1481, 1960.
- Hirono, M., and H. Maeda, Geomagnetic distortion of the F_2 region on the magnetic equator, J. Geophys. Research, 60, 241-255, 1955.
- Johnson, M. H., and E. O. Hulburt, Diffusion in the ionosphere, Phys. Review, 79, 802-807, 1950.
- Kent, G. S., High frequency fading of the 108 Mc/s wave radiated from an artificial earth satellite, J. Atmospheric and Terrest. Phys., 22, 255-269, 1961.
- Knecht, R. W., Possibility of detecting ionospheric drifts from the occurrence of spread F echoes at low latitudes, Nature, 187, 927, 1960.
- Knecht, R. W., Temporal and spatial variations in low latitude spread F occurrence (in preparation, 1962).
- Koster, J. R., and R. W. Wright, Scintillation, spread F, and trans-equatorial scatter, J. Geophys. Research, 65, 2303-2306, 1960.
- Lowan, A. N., On the cooling of the upper atmosphere after sunset, J. Geophys. Research, 60, 421-429, 1955.
- Lyon, A. J., N. J. Skinner, and R. W. Wright, Equatorial spread F and magnetic activity, Nature, 181, 1724-1725, 1958.
- Lyon, A. J., N. J. Skinner, and R. W. Wright, The geomorphology of equatorial spread F, Some Ionospheric Results Obtained during the International Geophysical Year, W. J. G. Beynon, ed., 153-157, 1960a.

- Lyon, A. J., N. J. Skinner, and R. W. Wright, The belt of equatorial spread F, J. Atmospheric and Terrest. Phys., 19, 145-159, 1960b.
- Lyon, A. J., N. J. Skinner, and R. W. Wright, Equatorial spread F at Ibadan, Nigeria, J. Atmospheric and Terrest. Phys., 21, 100-119, 1961.
- Martyn, D. F., The propagation of medium radio waves in the ionosphere, Proc. Phys. Soc., 47, 323-339, 1935.
- Martyn, D. F., Electric currents in the ionosphere. III. Ionization drift due to winds and electric fields, Phil. Trans. Roy. Soc., 246A, 306-320, 1953.
- Martyn, D. F., Large-scale movements of ionization in the ionosphere, J. Geophys. Research, 64, 2178-2179, 1959.
- Mitra, S. K., Geomagnetic control of the F₂ region of the ionosphere, Nature, 158, 668-669, 1946.
- Nicolet, M., The properties and constitution of the upper atmosphere, Physics of the Upper Atmosphere, J. A. Ratcliffe, ed., 17-71, 1960.
- Norton, R. B., and T. E. VanZandt, The daytime equatorial F region (in preparation, 1962).
- Pitteway, M. L. V.; and R. Cohen, A waveguide interpretation of 'temperate-latitude' spread F on equatorial ionograms, J. Geophys. Research, 66, 3141-3156, 1961.
- Rao, C. V. S., and S. N. Mitra, Spread F and geomagnetic activity, J. Geophys. Research, 67, 127-134, 1962.
- Rao, M. S. V. G., and B. R. Rao, Nocturnal and seasonal variations of equatorial spread F, J. Atmospheric and Terrest. Phys., 22, 12-22, 1961a.
- Rao, M. S. V. G., and B. R. Rao, Equatorial spread F in relation to post-sunset height changes and magnetic activity, J. Geophys. Research, 66, 2113-2120, 1961b.
- Rao, M. S. V. G., B. R. Rao, and P. R. Pant, Correlation of spread F activity with F-region height changes, J. Atmospheric and Terrest. Phys., 17, 345-347, 1960.
- Ratcliffe, J. A., Movements in the ionosphere, Nature, 177, 307-308, 1956.
- Ratcliffe, J. A., Ionization and drifts in the ionosphere, J. Geophys. Research, 64, 2102-2111, 1959.

- Ratcliffe, J. A., The Magneto-Ionic Theory and Its Applications to the Ionosphere, Cambridge University Press, 206 pp., 1959.
- Ratcliffe, J. A., and K. Weekes, The ionosphere, Physics of the Upper Atmosphere, J. A. Ratcliffe, ed., 377-470, 1960.
- Reber, G., Spread F over Hawaii, J. Geophys. Research, 59, 257-265, 1954a.
- Reber, G., Spread F over Washington, J. Geophys. Research, 59, 445-448, 1954b.
- Reber, G., World-wide spread F, J. Geophys. Research, 61, 157-164, 1956.
- Renau, J., A study of ionospheric spread echoes, Cornell University Research Report No. EE-442, 1959a.
- Renau, J., A theory of spread F based on a scattering-screen model, J. Geophys. Research, 64, 971-977, 1959b.
- Renau, J., Theory of spread F based on aspect-sensitive backscatter echoes, J. Geophys. Research, 65, 2269-2277, 1960.
- Ryle, M., and A. Hewish, The effects of the terrestrial ionosphere on the radio waves from discrete sources in the galaxy, Mon. Not. Roy. Astron. Soc., 110, 381-394, 1950.
- Serbu, G. P., R. E. Bourdeau, and J. L. Donley, Electron temperature measurements on the explorer VIII satellite, J. Geophys. Research, 66, 4313-4315, 1961.
- Shimazaki, T., A statistical study of world-wide occurrence probability of spread F, Part I, Average State, J. Radio Res. Labs. (Japan), 6, 669-687, 1959a.
- Shimazaki, T., A statistical study of world-wide occurrence probability of spread F, Part II, Abnormal state in severe magnetic storms, J. Radio Res. Labs. (Japan), 6, 688-704, 1959b.
- Shimazaki, T., The diurnal and seasonal variations of the occurrence probability of spread F, Some Ionospheric Results Obtained during the International Geophysical Year, W. J. G. Beynon, ed., 158-164, 1960a.
- Shimazaki, T., The world-wide occurrence probability of spread F in severe magnetic storms, Some Ionospheric Results Obtained during the International Geophysical Year, W. J. G. Beynon, ed., 165-171, 1960b.
- Singleton, D. G., The geomorphology of spread F, J. Geophys. Research, 65, 3615-3624, 1960.

- Skinner, N. J., J. Hope, and R. W. Wright, Horizontal drift measurements in the ionosphere near the equator, Nature, 182, 1363-1365, 1958.
- Smith, E. K., and R. W. Knecht, Some implications of slant-Es, J. Atmospheric and Terrest. Phys., Special Supplement, Part II, 195-204, 1957.
- Spreiter, J. R., and B. R. Briggs, Theory of electrostatic fields in the ionosphere at equatorial latitudes, J. Geophys. Research, 66, 2345-2354, 1961.
- Whale, H. A., Fine structure of the ionospheric region E, J. Atmospheric and Terrest. Phys., 1, 233-243, 1951.
- Wild, J. P., and J. A. Roberts, Regions of the ionosphere responsible for radio-star scintillations, Nature, 178, 377-378, 1956.
- Wright, R. W., Geomorphology of spread F and characteristics of equatorial spread F, J. Geophys. Research, 64, 2203, 2207, 1959.
- Wright, R. W., J. R. Koster, and N. J. Skinner, Spread F echoes and radio-star scintillation, J. Atmospheric and Terrest. Phys., 8, 240-246, 1956.
- Wright, R. W., and N. J. Skinner, Equatorial spread F, J. Atmospheric and Terrest. Phys., 15, 121-125, 1959.

U. S. DEPARTMENT OF COMMERCE

Luther H. Hodges, *Secretary*

NATIONAL BUREAU OF STANDARDS

A. V. Astin, *Director*



THE NATIONAL BUREAU OF STANDARDS

The scope of activities of the National Bureau of Standards at its major laboratories in Washington, D.C., and Boulder, Colorado, is suggested in the following listing of the divisions and sections engaged in technical work. In general, each section carries out specialized research, development, and engineering in the field indicated by its title. A brief description of the activities, and of the resultant publications, appears on the inside of the front cover.

WASHINGTON, D. C.

Electricity. Resistance and Reactance. Electrochemistry. Electrical Instruments. Magnetic Measurements. Dielectrics. High Voltage.

Metrology. Photometry and Colorimetry. Refractometry. Photographic Research. Length. Engineering Metrology. Mass and Scale. Volumetry and Densimetry.

Heat. Temperature Physics. Heat Measurements. Cryogenic Physics. Equation of State. Statistical Physics.

Radiation Physics. X-ray. Radioactivity. Radiation Theory. High Energy Radiation. Radiological Equipment. Nucleonic Instrumentation. Neutron Physics.

Analytical and Inorganic Chemistry. Pure Substances. Spectrochemistry. Solution Chemistry. Standard Reference Materials. Applied Analytical Research. Crystal Chemistry.

Mechanics. Sound. Pressure and Vacuum. Fluid Mechanics. Engineering Mechanics. Rheology. Combustion Controls.

Polymers. Macromolecules: Synthesis and Structure. Polymer Chemistry. Polymer Physics. Polymer Characterization. Polymer Evaluation and Testing. Applied Polymer Standards and Research. Dental Research.

Metallurgy. Engineering Metallurgy. Microscopy and Diffraction. Metal Reactions. Metal Physics. Electrolysis and Metal Deposition.

Inorganic Solids. Engineering Ceramics. Glass. Solid State Chemistry. Crystal Growth. Physical Properties. Crystallography.

Building Research. Structural Engineering. Fire Research. Mechanical Systems. Organic Building Materials. Codes and Safety Standards. Heat Transfer. Inorganic Building Materials. Metallic Building Materials.

Applied Mathematics. Numerical Analysis. Computation. Statistical Engineering. Mathematical Physics. Operations Research.

Data Processing Systems. Components and Techniques. Computer Technology. Measurements Automation. Engineering Applications. Systems Analysis.

Atomic Physics. Spectroscopy. Infrared Spectroscopy. Far Ultraviolet Physics. Solid State Physics. Electron Physics. Atomic Physics. Plasma Spectroscopy.

Instrumentation. Engineering Electronics. Electron Devices. Electronic Instrumentation. Mechanical Instruments. Basic Instrumentation.

Physical Chemistry. Thermochemistry. Surface Chemistry. Organic Chemistry. Molecular Spectroscopy. Elementary Processes. Mass Spectrometry. Photochemistry and Radiation Chemistry.

Office of Weights and Measures.

BOULDER, COLO.

Cryogenic Engineering Laboratory. Cryogenic Equipment. Cryogenic Processes. Properties of Materials. Cryogenic Technical Services.

CENTRAL RADIO PROPAGATION LABORATORY

Ionosphere Research and Propagation. Low Frequency and Very Low Frequency Research. Ionosphere Research. Prediction Services. Sun-Earth Relationships. Field Engineering. Radio Warning Services. Vertical Soundings Research.

Radio Propagation Engineering. Data Reduction Instrumentation. Radio Noise. Tropospheric Measurements. Tropospheric Analysis. Propagation-Terrain Effects. Radio-Meteorology. Lower Atmosphere Physics.

Radio Systems. Applied Electromagnetic Theory. High Frequency and Very High Frequency Research. Frequency Utilization. Modulation Research. Antenna Research. Radiodetermination.

Upper Atmosphere and Space Physics. Upper Atmosphere and Plasma Physics. High Latitude Ionosphere Physics. Ionosphere and Exosphere Scatter. Airglow and Aurora. Ionospheric Radio Astronomy.

RADIO STANDARDS LABORATORY

Radio Physics. Radio Broadcast Service. Radio and Microwave Materials. Atomic Frequency and Time-Interval Standards. Radio Plasma. Millimeter-Wave Research.

Circuit Standards. High Frequency Electrical Standards. High Frequency Calibration Services. High Frequency Impedance Standards. Microwave Calibration Services. Microwave Circuit Standards. Low Frequency Calibration Services.

